

# **Wet Classification in the Centrifugal Fluidized Bed**

Vom Promotionsausschuss der  
Technischen Universität Hamburg-Harburg  
zur Erlangung des akademischen Grades

**Doktor-Ingenieur (Dr.-Ing.)**

genehmigte Dissertation

von

**Jan Margraf**

aus

**Hamburg**

2010

**Gutachter**

1. Prof. Dr.-Ing. Joachim Werther
2. Prof. Dr.-Ing. Gerd Brunner

**Tag der mündlichen Prüfung**

15. Juni 2010

## **VERLAGSTITELSEITE**

**CIP-Eintrag**  
**Copyright**

# **Vorwort**

Diese Arbeit ist während meiner Zeit als wissenschaftlicher Mitarbeiter am Institut für Feststoffverfahrenstechnik und Partikeltechnologie an der Technischen Universität Hamburg-Harburg entstanden.

Die Erstellung dieser Arbeit wurde mir durch kompetente Unterstützung meiner ehemaligen Kollegen am Institut ermöglicht. Mein besonderer Dank gilt dabei meinem Doktorvater Herrn Prof. Dr.- Ing. Joachim Werther, sowie Herrn Dr. Hartge für das Vertrauen und die Unterstützung in meine Arbeit.

Weiterhin möchte ich mich für die technische Unterstützung der Institutsangestellten Frank Rimoschat, Heiko Rohde und Bernhard Schult bedanken, die mir bei technischen Fragestellungen eine große Hilfe gewesen sind.

Auch möchte ich mich bei allen meinen ehemaligen Kollegen für die schöne und interessante Zeit am Institut bedanken, auf die ich immer gerne zurückblicken werde.

Die Fertigstellung dieser Arbeit erfolgte nach meinem Ausscheiden aus dem Institut neben meiner Tätigkeit als Entwicklungsingenieur bei der HJS Fahrzeugtechnik GmbH. Ich möchte mich an dieser Stelle ganz besonders bei meiner Familie und meiner Partnerin Meenu für die Unterstützung und den Beistand in dieser Zeit bedanken.

Dortmund, 20. Juni 2010

Jan Margraf



# Contents

<b>1. Introduction.....</b>	<b>1</b>
<b>2. State of the art.....</b>	<b>5</b>
2.1 Applications of rotating gas fluidized beds.....	6
2.2 Wet classification in stationary classifiers.....	8
2.2.1 The principle of gravity elutriation.....	8
2.2.2 Classification with hydrocyclones.....	10
2.3 Wet centrifugal classification in rotating classifiers.....	11
2.4 Classification from centrifugal fluidized beds.....	14
2.4.1 The principle of centrifugal elutriation.....	14
2.4.2 Centrifugal upstream classifiers.....	16
<b>3. Setup and design of the centrifugal fluidized bed classifier .....</b>	<b>27</b>
3.1 Experimental setup.....	28
3.2 The geometry of the classification chamber .....	31
<b>4. Theory.....</b>	<b>34</b>
4.1 A simplified hydrodynamic model of the liquid flow in the solids-free chamber (model I).....	35
4.2 CFD simulation of the pure liquid flow (model II) .....	38
4.2.1 Geometry and computational grid.....	39
4.2.2 The CFD model.....	43
<b>5. Experimental.....</b>	<b>45</b>
5.1 Experimental materials.....	45
5.2 Flow measurement techniques in the rotating classification chamber	48

5.2.1	Pure liquid flow in the rotating classification chamber.....	48
5.2.2	Flow of the fluidized bed in the rotating classification chamber.....	52
5.3	Optimization of the coarse discharge .....	54
5.4	The usage of the Richardson Zaki correlation for the prediction of the expansion behavior.....	56
5.5	Measurement of the bed pressure drop.....	61
5.6	A concept of the control of the operation of the classifier.....	64
5.6.1	Calculation of the fluidized bed pressure drop from the liquid column gauge.....	65
5.6.2	Bed pressure drop model.....	67
5.6.3	Pressure drop model for rotating fixed beds.....	69
5.6.4	Determination of the operational parameters.....	70
5.7	Evaluation of the classification experiments.....	75
<b>6.</b>	<b>Results and discussion.....</b>	<b>82</b>
6.1	Fluid mechanics of the flow in the classification chamber.....	82
6.1.1	Results of the simplified model.....	82
6.1.2	Results of the CFD simulation.....	86
6.1.3	Comparison of the results of the simplified model with CFD calculations and experiments conducted with a tracer sphere.....	89
6.1.4	The tangential velocity in the freeboard above the fluidized bed.....	91
6.1.5	Motion of the fluidized bed in the centrifugal field.....	93
6.2	Pressure drop.....	96
6.2.1	Pressure drop of the distributor.....	96
6.2.2	The fluidized bed pressure drop.....	98
6.3	The expansion behavior of the fluidized bed .....	103



---

6.4	Analysis of the particle size distributions .....	106
6.5	Classification experiments with the original configuration of solids discharge.....	111
6.6	Estimation of the outgoing mass flows for classification with the optimized coarse discharge nozzles.....	114
6.7	Classification experiments with the optimized coarse discharge.....	118
6.8	Classification with the coarse discharge nozzle type III.....	122
6.9	Classification with the coarse discharge nozzle type IV.....	124
6.9.1	Influence of the bed height.....	126
6.9.2	Effect of the number of feed ports on the classification with nozzle IV.....	129
6.9.3	Classification of limestone.....	133
6.9.4	Classification of quartz for cut sizes between 1 and 10 $\mu\text{m}$ .....	134
6.9.5	Classification of glass beads.....	136
6.10	Practical example of the control strategies for quartz powder classification.....	138
<b>7.</b>	<b>Summary and conclusions.....</b>	<b>143</b>
	<b>Nomenclature.....</b>	<b>145</b>
	<b>References.....</b>	<b>148</b>
	<b>Curriculum vitae.....</b>	<b>152</b>



# 1 Introduction

For many industrial applications particle sizes in the micron range and below are demanded, like in the minerals industry, in powder metallurgy, in ceramics industry or for toners or pigments.

Powder metallurgy products are used today in a wide range of industries, from automotive and aerospace applications to power tools and household appliances. Powder metallic and ceramic products are mainly manufactured by sintering. Sintering is a method for making objects from powder, by heating the material (below its melting point - solid state sintering) until its particles adhere to each other. Sintering is traditionally used for manufacturing ceramic objects, but has also found uses in such fields as powder metallurgy. For gaining high quality products by sintering it is necessary to process very fine particles.

Other fields where fine particles are demanded are pigments and toners. Pigments are used for coloring paint, ink, plastic, fabric, cosmetics, food and other materials. Most pigments used in manufacturing and the visual arts are dry colorants, usually ground into a fine powder.

Originally, the particle size of toner averaged between 14–16 micrometers (Nakamura and Kutsuwada, 1989). To improve image resolution, particle size was reduced, eventually reaching about 8–10  $\mu\text{m}$  for 600 dots per inch resolution. Further reductions in particle size producing further improvements in resolution are being developed recently (Mahabadi and Stocum, 2006). Toner manufacturers maintain a quality control standard for particle size distribution in order to produce a powder suitable for use in their printers.

For the production of fine powders the classification, i.e. the separation of polydisperse particle collectives into a coarse and a fines fraction, plays an important role. Classification processes are applied, when specific particle sizes are required and particles, which do not fulfill the demands, have to be removed from the product. During the production of fine particles, e.g. by grinding, spray drying or crystallization, particles with sizes outside the desired range are generated as unwanted byproducts, so that classification processes have to be applied.

Sieves and air classifiers are mainly used for dry classification tasks, for wet classification tasks standard apparatus like the hydrocyclone, the worm screen, the decanting centrifuge and the elutriator are available. However, they all show significant drawbacks when it comes to classification in the range of a few microns.

A major problem of standard centrifugal classifiers is the occurrence of a fishhook effect and an unsatisfactory classification performance with cut sizes in the micron range. The fishhook effect describes the increase of fines that have been misclassified to the coarse recovery with decreasing particle diameter (Majumder, et. al., 2003). Gravity classifiers or elutriators in general show a high separation performance and are therefore widely used in industry (Schmidt, 2004). The drawback of gravity classification is the too slow settling velocities of particles in the micron range. Smaller particles below 1  $\mu\text{m}$  can form a stable suspension in the gravity field, where no further sedimentation occurs. Industrial classification in the gravity field in the micron range is therefore nearly impossible. For the operation of an elutriator with cut sizes in the micron range an enhancement of the particles' settling velocities is necessary. This can in principle be achieved by a substitution of the gravity field by a centrifugal field.

In the past different lab scale centrifuges were designed to perform centrifugal elutriation. But all of the devices were found to be not directly applicable in industrial

application due to batch operation, low throughput and/or bypass of fines. This will be discussed in detail in chapter 2.

A continuously operating counter current classifier in the centrifugal field has been developed at the TU Hamburg-Harburg in the “Institute of Solids Process Engineering and Particle Technology”, which should be able to perform industrial separation tasks (Schmidt and Werther 2005). However, the separation performance in the latter classifier revealed a fishhook effect as it is often observed in hydrocyclone classification. The reason for that was not really clarified yet, as well as the properties of the fluidized bed and the fluid mechanics. Besides that the control of the bed height and the outgoing massflows were not satisfying.

The aim of the present work is therefore to study the fluid mechanics, the separation process and the fluidized bed behavior and to optimize the classifier and its separation performance to fulfill the demands of industrial classification in the micron range.

In the first part of this work the fluid mechanics of the classifier are presented. The investigation was performed by CFD simulations and experiments with tracers, which were introduced into the classifier and observed with a high speed camera and a stroboscope. Especially the influence of the Coriolis force on the flow pattern of the fluid and the fluidized bed was studied, which plays an important role in rotating systems at high angular velocities.

Based on a thorough analysis of the system behavior a novel coarse discharge mechanism was developed, which was capable to improve the classification.

In order to find suitable operating conditions the pressure drop profile was measured and modeled to determine the minimum fluidizing velocity, below which classification tasks are impossible. Classification experiments with the improved coarse discharge

were conducted and the results are presented in the following. The influence of the cut sizes, the bed height, the coarse discharge and the angular velocities are discussed.

## 2 State of the art

Fluidization technology, i.e. the induction of liquid like behavior of a particle collective by a flow opposite to the direction of gravity, is widely used in industry. In the fluidized state the weight of the particles is completely carried by the drag of the flow. All particles are then suspended by the upward-flowing gas or liquid and are able to move freely in the bed like the molecules in a fluid. The characteristics of a fluidized particle collective is depending on the properties like particle size distribution, density or shape and can be described by the approach of Geldart (Kuni and Levenspiel, 1991).

Geldart distinguished between four main categories of fluidizing behavior, taking the density difference between particles and fluid and the mean particle diameter into account, which are shown in the Geldart chart for beds fluidized with air at ambient conditions (figure 2.1). Geldart A and B beds are strongly bubbling and Geldart D beds can also spout when they are fluidized.

With decreasing diameter cohesion forces gain more and more influence on the behavior of the fluidized bed and interparticle forces are greater than those resulting from the action of the fluid. These beds are extremely difficult to fluidize and are classified as Geldart C beds. Geldart C beds usually exhibit channeling, plugging and the formation of “rat holes” (Watano et al., 2003).

With increasing interest in processing powders in the micron range (Geldart C) and below, the application of a fluidized bed with its benefits like enhanced heat, mass transfer or good handling due to fluid like behavior has a great potential in industrial applications. One possibility to fluidize these particles is the transfer into the centrifugal field. The replacement of the gravity by centrifugal acceleration allows the usage of such higher fluid velocities compared to the gravity field.

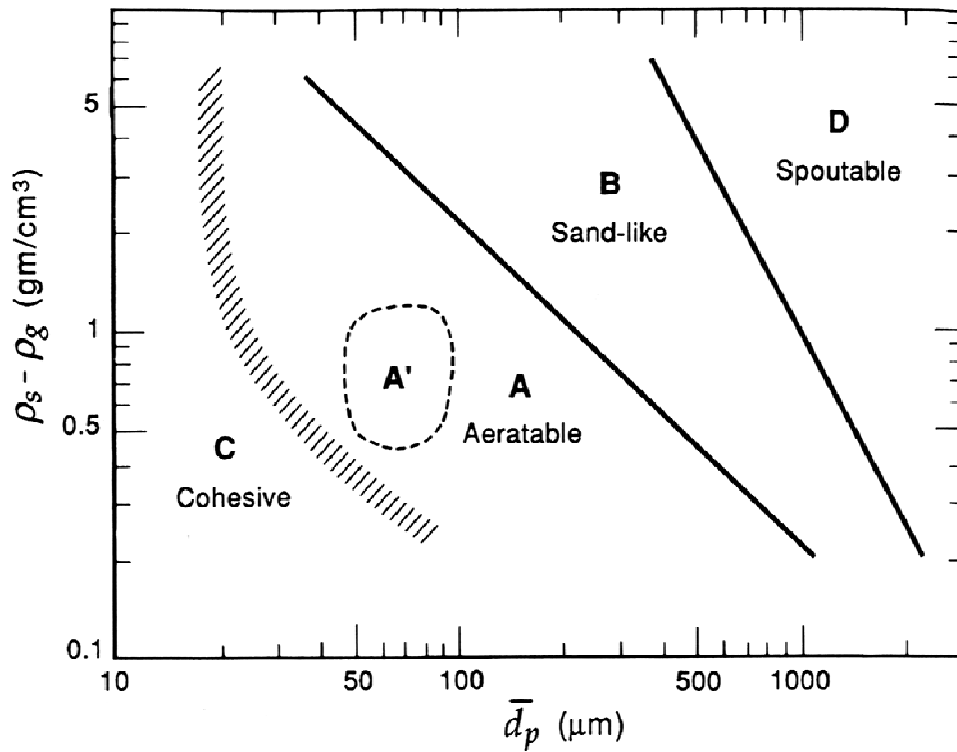


**Figure 2.1:** The Geldart classification of particles for air at ambient conditions (Kuni, Levenspiel, 1991)

Centrifugal fluidized beds are therefore gaining more and more interests in industry for processing particles in the micron range or below. The understanding of the fundamentals in these applications, either for liquid or gas fluidized beds, is therefore essential for the design of appropriate rotating fluidized beds, which is part of this work. In the present chapter different applications of rotating fluidized beds are presented with the focus on centrifugal counter current classification. Additionally other classifiers are discussed and their separation performances will be analyzed.

## 2.1 Applications of rotating gas fluidized beds

Different ways to induce a centrifugal field have been proposed in the literature. De Wilde and de Broqueville (2007) studied the concept of a centrifugal gas fluidized bed in a static geometry. In this case the centrifugal field was obtained by the tangential



injection of the fluidizing gas via multiple gas inlet slots in the outer wall of the fluidizing chamber.

A more common approach of centrifugal fluidization is the one in a rotating frame, i.e. the whole system including the distributor is rotating at the desired angular velocity. Qian et. al.,(2004) applied the fluidized bed in a horizontally rotating frame as a dust filter for diesel exhaust gas treatment, where the unwanted soot particles are captured in the fluidized bed. The advantage of the rotating fluidized bed for this application is the reduction of the pressure drop compared to other types of granular bed filters. The formation of bubbles and the bubble size development was studied and modeled by Nakamura et. al.(2007), who found a reduction of bubble size with increasing centrifugal acceleration in the rotating fluidized bed.

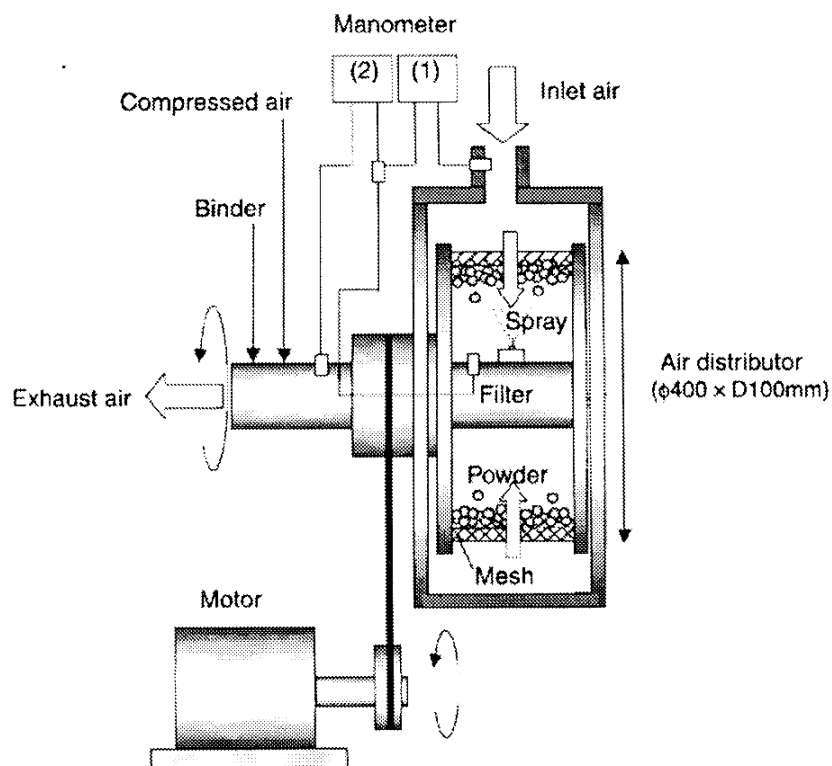


**Figure 2.2:** Rotating fluidized bed by Watano et. al. (2003)

Watano et. al. developed a rotating fluidized bed as shown in figure 2.2 for the purposes of granulation (2003) and coating (2004). They fluidized highly cohesive

cornstarch powder with a median diameter of 15  $\mu\text{m}$  and obtained uniform fluidization. The feasibilities of the granulation and the coating of micro particles due to the centrifugal acceleration were demonstrated.

## 2.2. Wet classification in stationary classifiers

For processing particles with a desired range in size or density the use of classification processes, i.e. the separation of a particle collective into a coarse and fines fraction, is unavoidable. Dry classification is normally performed by air classifiers or sieves, for the wet classification the most common classifier is the counter current classifier or elutriator.

### 2.2.1 The principle of gravity elutriation

The principle of a gravity elutriator is shown in figure 2.3. The suspension is introduced into the classifier from the top. While the particles are settling in the gravity environment, the fluid phase of the suspension and additional injected water through the distributor are forming an upstream, which is directed against the particles' settling velocities. As smaller particles are settling slower than larger particles, the presence of

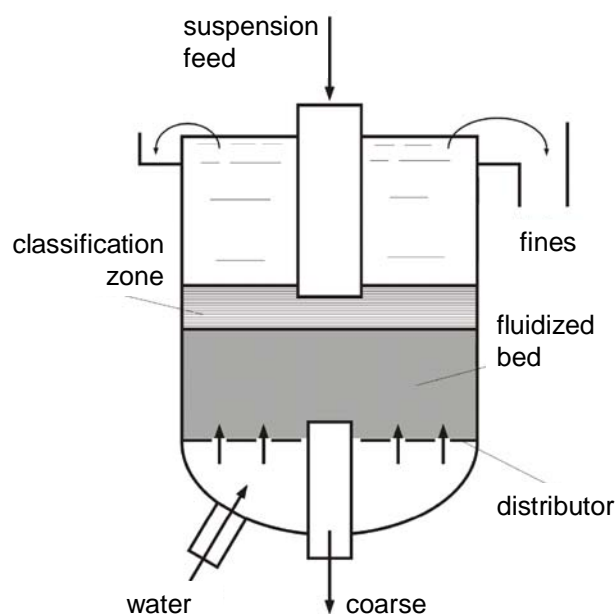


**Figure 2.3:** Gravity elutriator (Schmidt, 2004)

an upstream is causing classification by taking the fines to an overflow weir, while the coarse particles are settling in the direction of the distributor. The coarse particles are accumulating in a bed, which is fluidized by the water injected through the distributor. An intense movement of particles inside the fluidized bed is causing agglomerates to decompose (Kalck, 1990), the emerging fines are carried out of the bed with the upstream to the weir.

Elutriators can be operated continuously and high separation performances can be achieved. The performance of the classification can be characterized by the separation efficiency curve  $T(d_p)$ , which denotes the ratio of the coarse recovery to the feed mass flow for a particle diameter  $d_p$ . The characterization of the classification performance is discussed in detail in chapter 5.7.

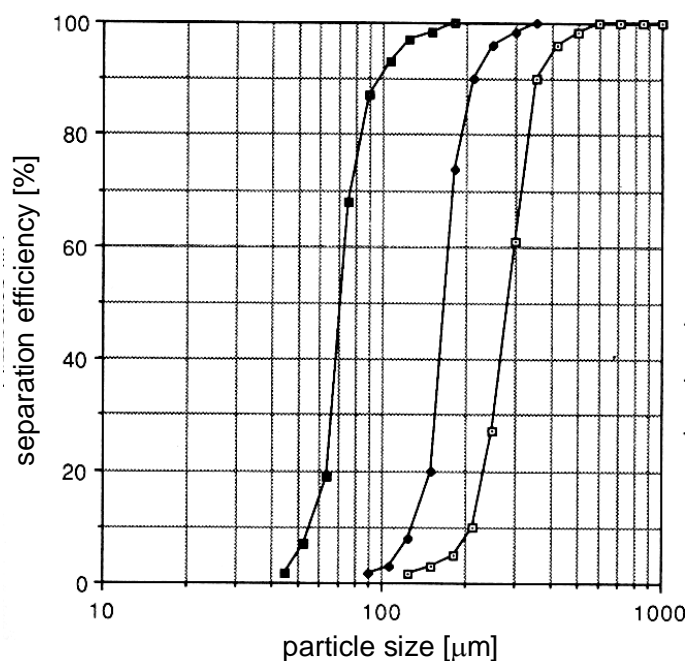


**Figure 2.4:** Typical separation efficiency curves of gravity elutriation for sand (Heiskanen, 1993)

Typical separation efficiency curves are presented by Heiskanen (1993) in figure 2.4 for sand with cut sizes above 70  $\mu\text{m}$ . The presented curves show a sharp classification, as it is desired for a classification process. Due to the reliability, the classification performance and the low costs, the elutriator is widely used in industry.

Unfortunately, with decreasing particle diameter, the throughput is reduced or alternatively, the elutriator's diameter is increased to unacceptable high values at small cut sizes, whereby the gravity elutriator is not applicable for classification tasks in the micron range.

### 2.2.2 Classification with hydrocyclones

Wet classification for cut sizes in the micron range can be enabled by the enhancement of the settling velocities by a centrifugal field. A very common apparatus for this purpose is the hydrocyclone, which is sketched in figure 2.5. The hydrocyclone consists of a cylindrical part with the feed injection and overflow at the top and a conical part with coarse discharge at the bottom. The feed is tangentially injected, which induces a

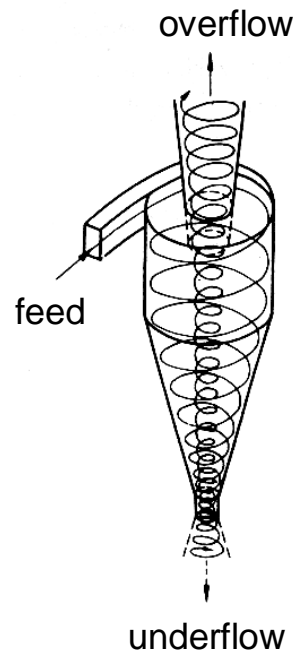


**Figure 2.5:** Principle of a hydrocyclone

downward oriented vortex in the wall region. In the conical part an upward oriented vortex at the center of the cyclone is achieved by the constriction of the cross sectional area. The flow is then leaving the cyclone at the overflow. Due to the centrifugal force the coarse particles are carried along the outer vortex at the wall and are then discharged at the underflow, while the fines are able to follow the flow to the overflow. Hydrocyclone classifications are normally applied for cut sizes between 5 and 250  $\mu\text{m}$  (Kerkhoff, 1996). The popularity of the hydrocyclone is based on its low costs and its high throughput at a low place requirement. The main disadvantages are the high energy requirement and the sensitivity to clogging and unsatisfactory separation performance (Kerkhoff, 1996). Especially the occurrence of the “fishhook effect” (Majumder et. al., 2003), i.e. the recovery of fine particles in the hydrocyclone

underflow increases with decrease in particle size, is a major problem for hydrocyclone classification tasks.

Figure 2.6 shows a typical separation efficiency curves of a hydrocyclone classification with quartz (Gerhart, 2001) in the fines region, where a distinct “fishhook effect” occurs. The reason for the “fishhook effect” is not really clarified yet, imprecise particle size analysis, different densities of aggregates in the feed, flocculation of fines and the dragging of fines to the underflow by coarse particles are discussed in the literature (Gerhart, 2001). The separation efficiency of hydrocyclones in the micron range is therefore not satisfying, so that other approaches have to be considered.

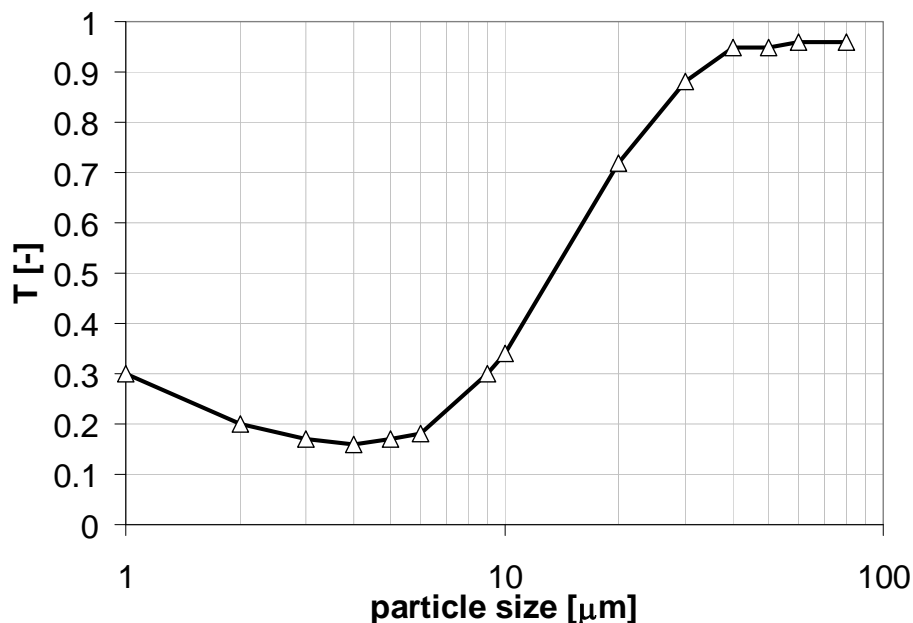


**Figure 2.6:** Typical separation efficiency curve of hydrocyclone classification (Gerhart, 2001) (hydrocyclone diameter: 39mm, pressure drop: 1.5 bar; material: quartz)

### 2.3 Wet centrifugal classification in rotating classifiers

Another possibility to create a centrifugal field is to rotate the whole apparatus. The most common application is the centrifuge, which is often employed for classification or dewatering tasks. For continuous operations decanter centrifuges are used (figure 2.7), in which the sediments are carried by a conveyor screw to the outlet (Stieß, 1993). In the literature classifications are reported with cut sizes down to 10  $\mu\text{m}$

(Kellerwessel, 1979). Unfortunately, these centrifuges cause a strong compaction of the sediment and fines are likely to be misclassified with the sediment to the coarse discharge, what is not appropriate for industrial applications (Schmidt, 2004). An apparatus, which is often used in industry for liquid-solid separation is the disc-stack centrifuge. The principle is illustrated in figure 2.8 (Wang et. al, 1997). A suspension is introduced at the center, from there the suspension is distributed to the rotating chamber, where the separation takes place.

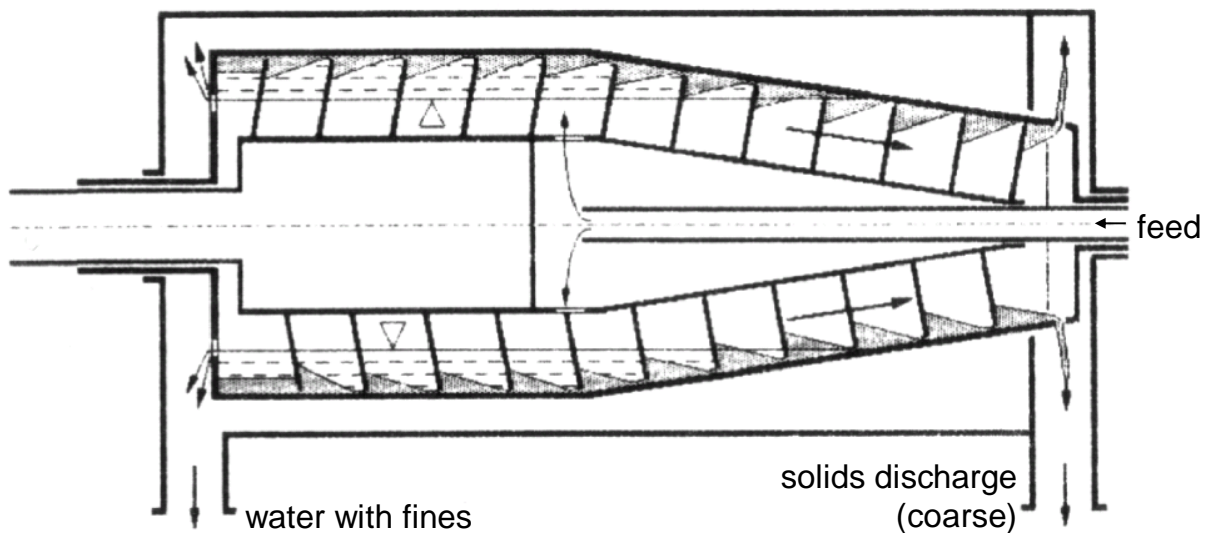


**Figure 2.7:** Principle of a decanter centrifuge (Stieß, 1993)

The coarse particles are settling to a coarse discharge nozzle, while the fluid is deflected and flowing versus the centrifugal force to the fluid outlet as pictured in figure 2.8. If disc-stack centrifuges are operated as classifiers it is unavoidable, that fines are following the coarse particles instead of the fluid at the turnaround point. This leads to a huge amount of misclassified fines (Schmidt, 2004).

For separation tasks for small cut sizes spinning wheel separators are often employed. The principle is pictured in figure 2.9. The suspension is introduced (1) into a non rotating chamber with a spinning wheel (4) inside. The fluid is passing through the wheel versus the centrifugal acceleration in direction to the center. The centrifugal

acceleration is forcing the coarse particles back to outer chamber (2) from which the coarse particles are discharged. The fines reaching the centre are then discharged with the fluid (3). A problem of this principle is that the shear forces at the transition from the non – rotating chamber to the wheel may cause breakage or attrition of the particles. Another disadvantage is an unavoidable bypass of fines to the coarse

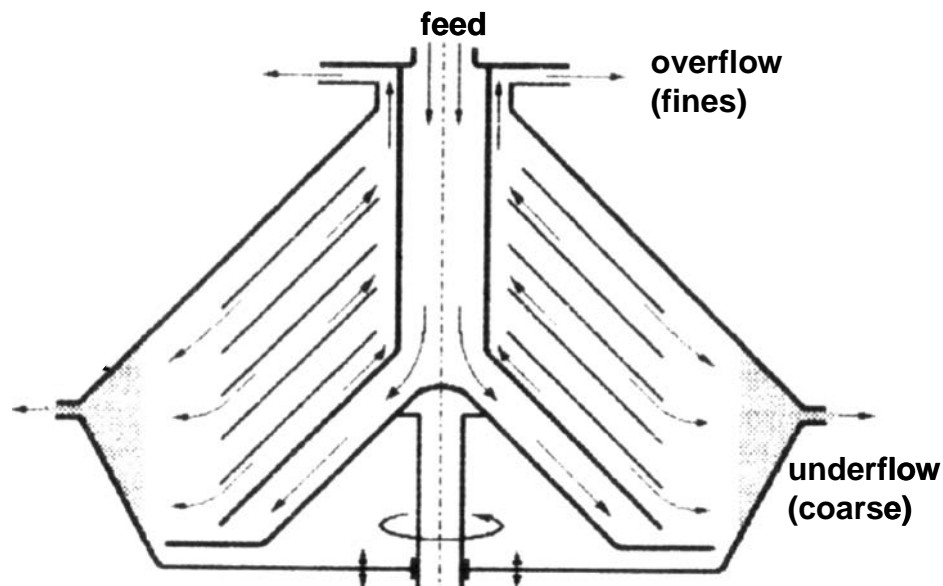


**Figure 2.8:** Principle of a disc stack centrifuge (Wang et. al, 1997)

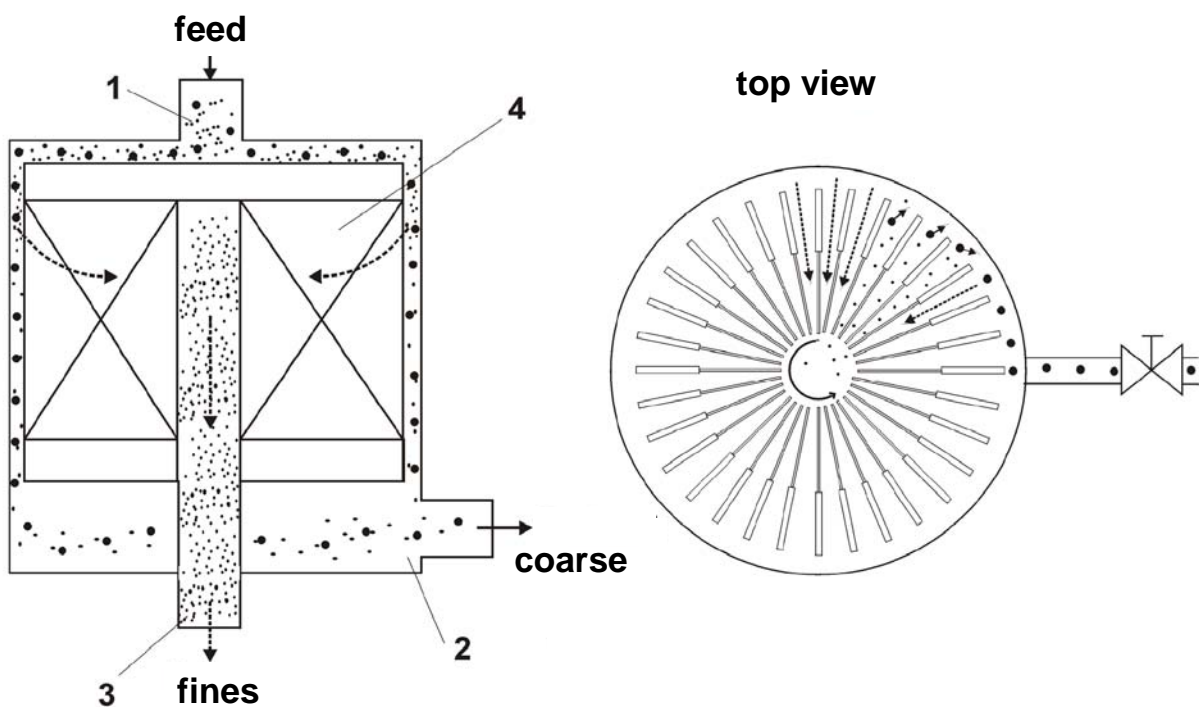


**Figure 2.9:** Principle of a spinning wheel separator (Schmidt, 2004)

fraction. Figure 2.10 shows a separation efficiency curve of such a classification. A cut size of 8  $\mu\text{m}$  was reached, but a large amount of fines were misclassified, what is indicated by the fishhook effect in the range below 4  $\mu\text{m}$ .

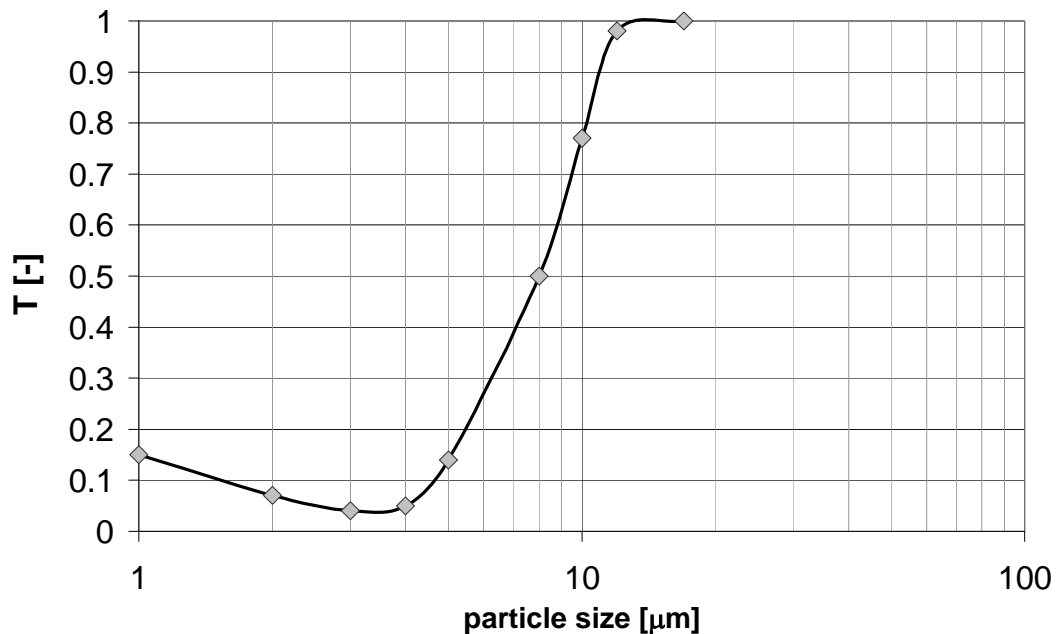


**Figure 2.10:** Separation efficiency of a soil classification with a spinning wheel separator (AHP 63, Hosokawa Alpine AG, Augsburg, Germany)

## 2.4. Classification from centrifugal fluidized beds

The devices presented above are capable for dewatering tasks and for the depletion of a sharp fines fraction. When coarse fractions without fines are required the presented classifiers show unacceptably strong fishhook effects. As the gravity elutriator is a mature technology for reliable and sharp classification tasks, approaches were made to transfer this technology to the micron range by applying a centrifugal field.

### 2.4.1 The principle of centrifugal elutriation

The principle of a centrifugal elutriator is the similar to the gravity elutriator. A particle collective is settling versus a counter current flow at different settling velocities, which are depending on the particle diameter. As smaller particles are settling slower than



larger particles a separation takes place when some particles are settling slower than the velocity of the counter current. The gravity is replaced by a centrifugal force, which can be orders of magnitude higher than the gravity, whereby particles in the micron range can be classified. In contrast to gravity elutriation the centrifugal force is varying with the radius and the flow pattern is influenced by the Coriolis force (Margraf and Werther, 2008) acting perpendicular to radial direction.

For the illustration of centrifugal elutriation a radial force balance on a settling particle can be applied (figure 2.11). The particle, when settling stationary, is experiencing a centrifugal force  $F_C$ , a buoyancy force  $F_B$  and a drag force  $F_D$ . The gravity force  $F_G$  can be neglected, when  $F_G \ll F_C$  is valid. This applies for the operation of the classifier in this work. For spheres the following definitions are valid:

$$\text{Centrifugal force: } F_C = \rho_S \cdot \pi/6 \cdot d_p^3 \cdot \omega^2 \cdot r \quad (2.1)$$

$$\text{Buoyancy force: } F_B = - \rho_L \cdot \pi/6 \cdot d_p^3 \cdot \omega^2 \cdot r \quad (2.2)$$

$$\text{Drag force: } F_D = - c_D(\text{Re}_p) \cdot \pi/8 \cdot d_p^2 \cdot \rho_L \cdot v_R^2, \quad (2.3)$$

with the densities of the particles and the liquid  $\rho_S$ ,  $\rho_L$ , the particle diameter  $d_p$  and the radial fluid velocity  $v_R$  and the angular velocity  $\omega$ .

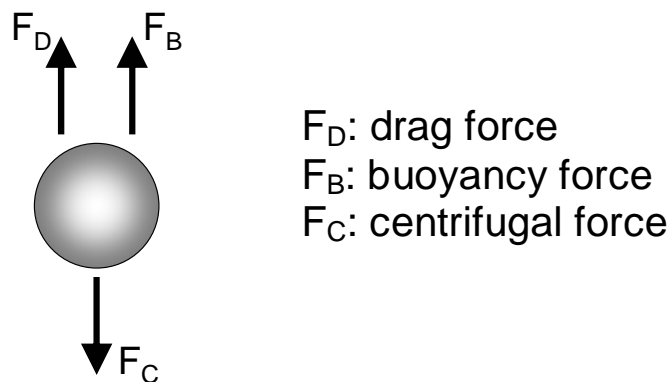


**Figure 2.11:** Radial forces acting on a stationary settling particle in a centrifugal field

A particle is theoretically floating at a constant radius in the upstream, when the sum of the radial forces equals zero.

$$F_B + F_C + F_D = 0 \quad (2.4)$$

In the Stokes range the drag coefficient  $c_D$  is defined:

$$c_D = 24/Re_p \quad (2.5)$$

With (2.5) the drag force  $F_D$  can be expressed by:

$$F_D = -3 \cdot \pi \cdot \eta \cdot v_R \cdot d_p, \quad (2.6)$$

where  $\eta$  denotes the viscosity of the fluid.

The radial fluid velocity  $v_R$  can be expressed by:

$$v_R = \frac{\dot{V}}{A_C} \quad (2.7)$$

In equation (2.7)  $\dot{V}$  denotes the liquid volume flow and  $A_C$  the cross sectional area at the radius  $r$ . For the theoretical cut size  $d_C$ , for which the radial fluid velocity equals the particle settling velocity, it holds:

$$d_C = \sqrt{\frac{\dot{V}}{A_C} \cdot \frac{18 \cdot \eta}{(\rho_S - \rho_L) \cdot \omega^2 \cdot r}} \quad (2.8)$$

#### 2.4.2 Centrifugal upstream classifiers

Preliminary studies to employ centrifugal counter current classification for cut sizes in the micron range were published by Colon (Colon et. al., 1970). Colon developed two prototypes, which are pictured in figures (2.12) and (2.13). The classification chamber in the first prototype (figure 2.12) is a segment of the rotor. The suspension is introduced in the center of the rotor (1) and then accelerated in 2 channels to the speed of the rotor. In the classification chambers the suspension is then channeled to the outer radius of the classification chamber and then turned back in direction of the

center. The fines are carried to the outlet (3), while the coarse particles accumulate in the fluidized bed. A non rotating housing collects the fluid and the fine particles. They are discharged at the outlet (2). The accumulated coarse particles in the classification chamber have to be removed periodically.

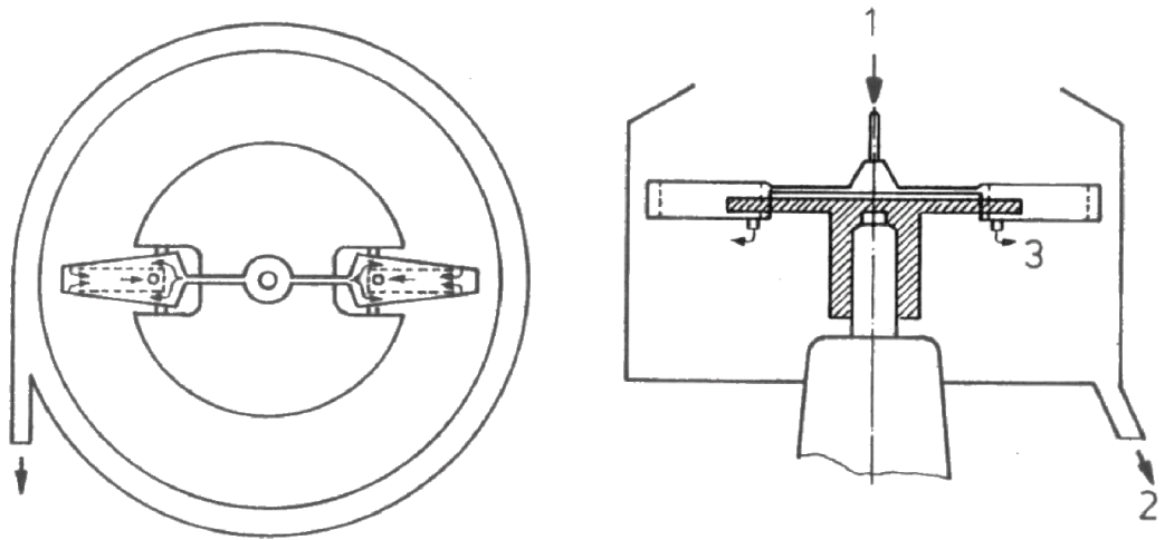


**Figure 2.12:** Centrifugal classifier by Colon (1970) – Prototype I

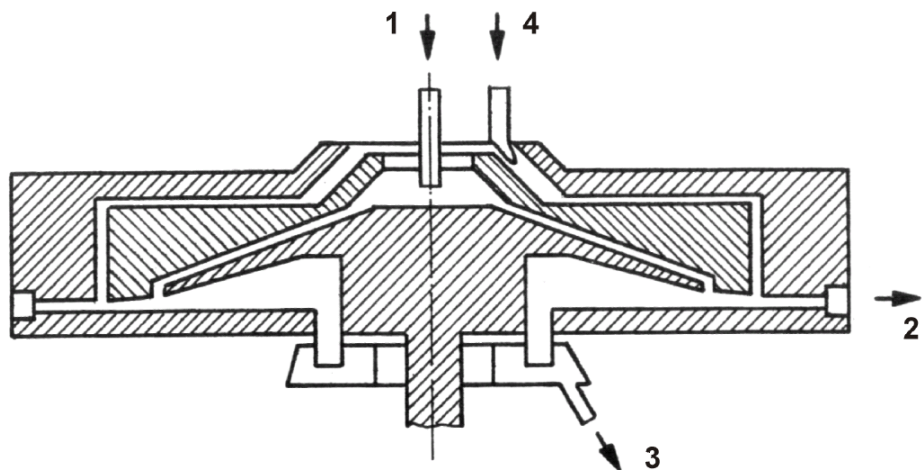


**Figure 2.13:** Centrifugal classifier by Colon (1970) – Prototype II

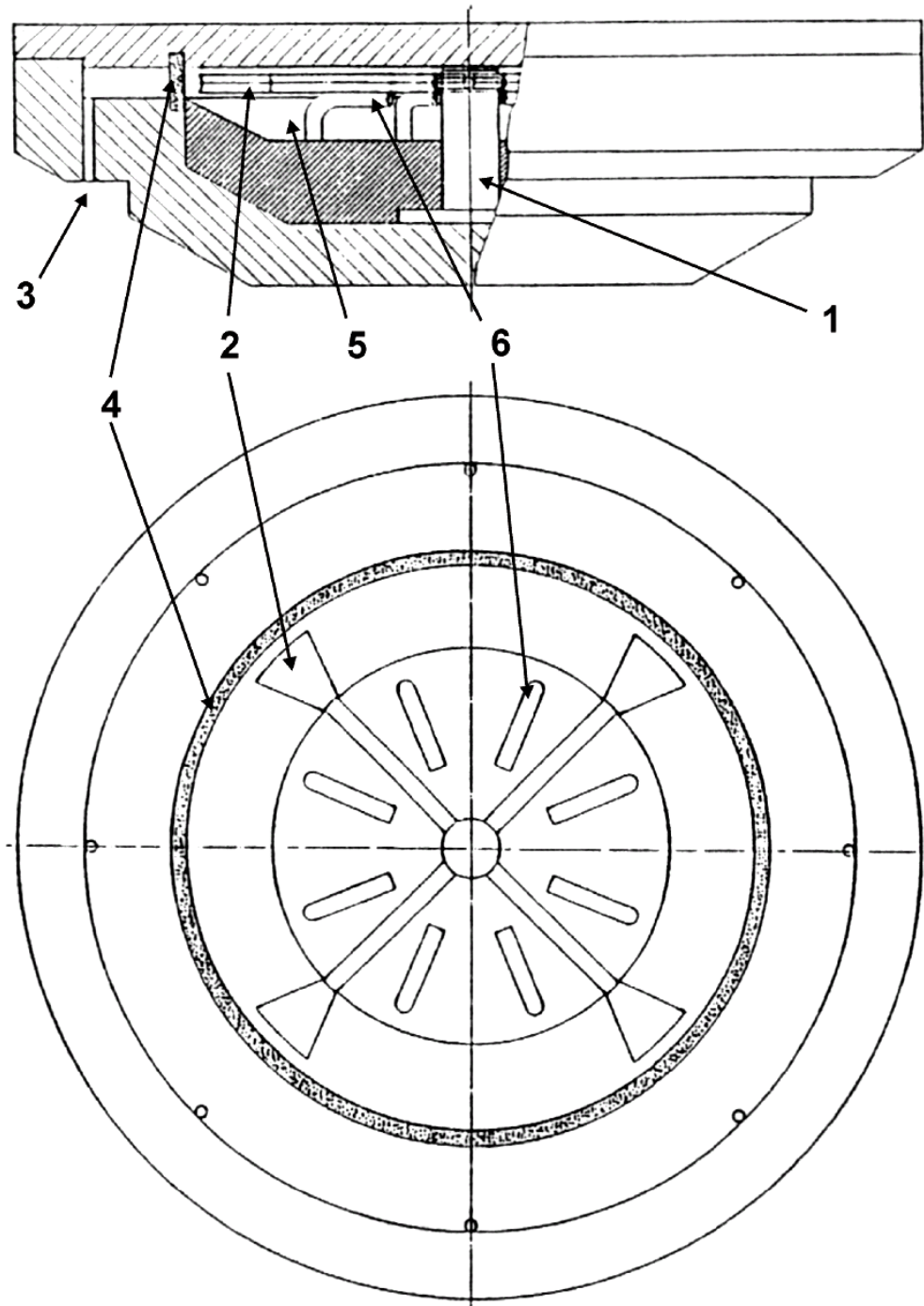
The second prototype (figure 2.13) can be operated continuously. The suspension is fed into the classification chamber at position (1), from where it is channeled to the classification chamber. Additional water is introduced at (4), which causes a counter current in the classification chamber. The coarse particles are settling versus the

centrifugal force and are discharged at the outlet (2). The fines are taken with the current to the overflow (3). Colon successfully performed classifications with glass beads for cut sizes down to 3  $\mu\text{m}$  (Schmidt, 2004). However, the achieved throughput lies in lab scale dimension and is therefore not applicable for industrial purpose.

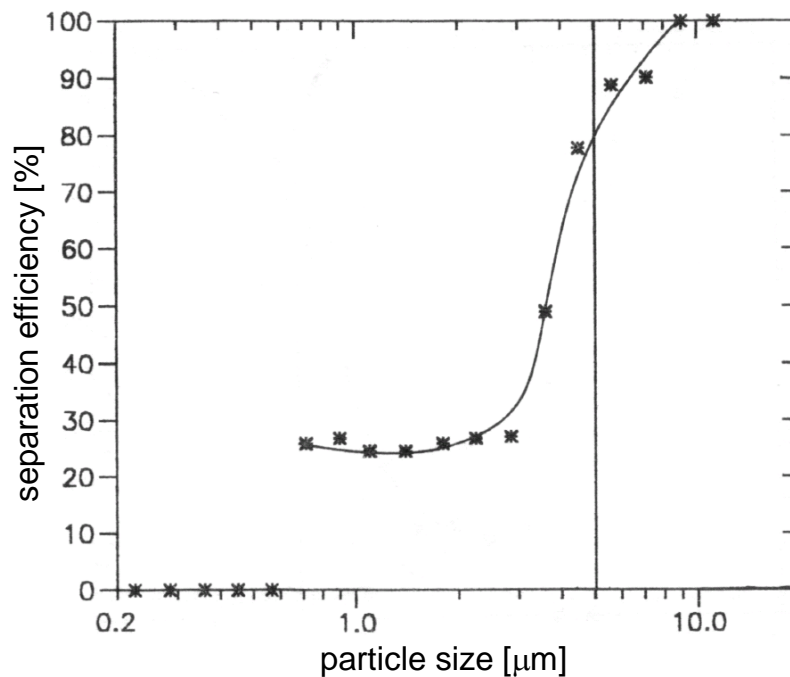
Priesemann (1994) designed a centrifugal upstream classifier with a circumferential classification chamber, where the chamber width is expanding with decreasing radius to assure a constant cut size over the chamber height. The classifier has to be operated batch-wise, the experimental setup is pictured in figure 2.14. The suspension is introduced into the classifier via a hollow shaft (1) and then channeled to the classification chamber (5) by four pipes with nozzles (2) at the end. For the generation of a counter current, additional water is injected to a ring chamber (3) at the outer radius of the classifier. The water is passing a porous sinter metal distributor and fluidizes the particles in the classification chamber. The fluidizing water with the fines fraction is leaving the classifier via eight pipes (6). The coarse fraction is accumulating in the fluidized bed and has to be removed, when a certain bed mass is reached. Priesemann reached sharp classifications with cut sizes down to 4  $\mu\text{m}$ , but still with a large amount of fines been misclassified. Figure 2.15 shows a separation efficiency curve of Priesemann with a suspension volume flow of 52 l/h and a centrifugal acceleration of 200g with quartz as solid feed. The diameter of the classification chamber at the distributor level was 200 mm. The separation efficiency curve looks a bit strange with a fishhook between 0.7 and 3  $\mu\text{m}$  and an ideal classification below 0.6  $\mu\text{m}$ .

Based on the findings of Priesemann, Timmermann (1998) designed a continuously operating centrifugal fluidized bed classifier for a higher throughput ratio. Contrary to Priesemann the classification chamber is not circumferential, but consisting of closed chambers. The rotor with a diameter of 200 mm can be rotated between 300 and 3000 rpm resulting in a range of centrifugal accelerations between 100 to 1000 times the

gravity acceleration. Cut sizes down to  $0.5\ \mu\text{m}$  are possible at a suspension volume flow up to 180 ml/min.

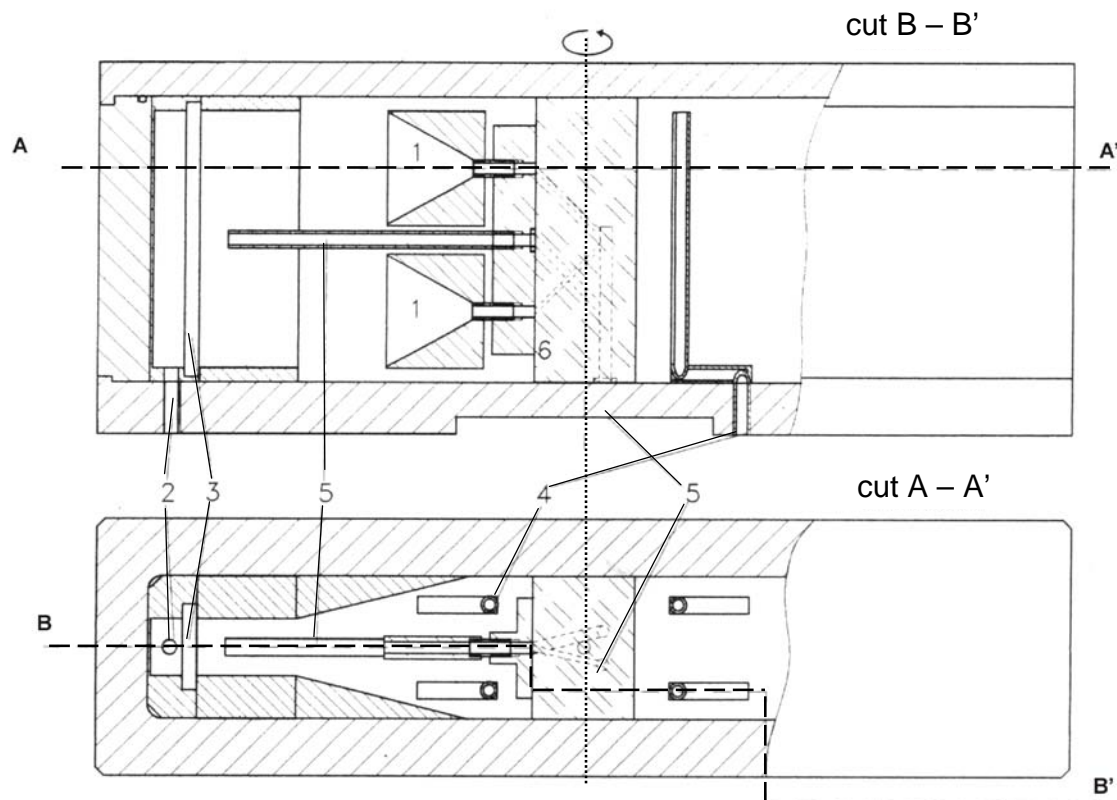


**Figure 2.14:** Setup of the centrifugal classifier of Priesemann (1994)



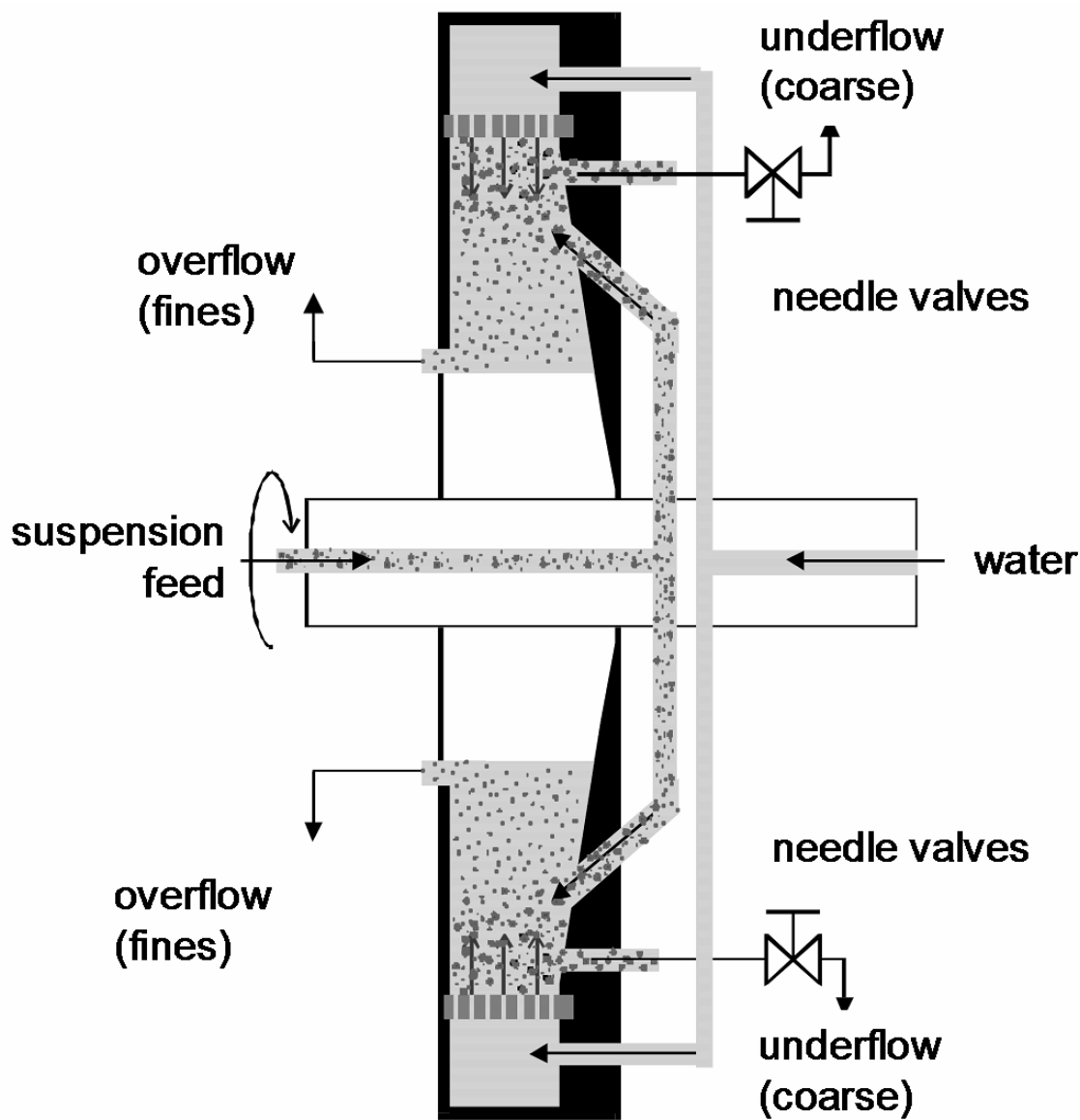
**Figure 2.15:** Separation efficiency curve of the centrifugal classifier by Priesemann (1994)

Figure 2.16 shows two cuts through the classification chamber of the apparatus of Timmermann (1998). Four suspension injection nozzles (1) are installed in the classification chamber and are fed with suspension from a hollow shaft. The fluidizing water is introduced to the apparatus at (2) and flows through a porous distributor (3), behind which it fluidizes the bed consisting of the coarse fraction. The coarse particles can be discharged by a suction tube (5) which is submerged in the fluidized bed during operation. It has to be mentioned that the suction velocity at the coarse discharge has to be higher than the settling velocity of the coarse particles. The fines are taken with the fluidizing water to the overflow (4), where they get discharged. Under this condition a high volume flow is passing through the coarse discharge pipe leading to a high dilution or low solids concentration in the coarse suspension. Timmermann reports in his work about comparable results like Priesemann in her batch experiments, but with continuous operation. For an industrial application the throughput ( $0.0006 - 0.019 \text{ m}^3/\text{h}$ ) and the separation efficiency are still not sufficient.



**Figure 2.16:** Setup of the centrifugal classifier of Timmermann (1998)

As the above presented classifiers do not show satisfactory results for classification in the micron range with throughputs adequate for industrial application, Schmidt (2004) designed a centrifugal counter current classifier, which is also the equipment of the present work. The principle is shown in figure 2.17. Like in a gravity elutriator the suspension is fed into the classification chamber where the settling of the particles is hindered by a counter current flow. The insertion of the suspension and the fluidizing water is realized by rotary feedthroughs to the hollow shafts in the axis. The fines are carried by the current to an overflow weir, while the coarse fraction is forming the fluidized bed, from where the coarse particles are discharged. The centrifugal force can be adjusted to exceed the gravitational force by orders of magnitudes to enable an appropriate settling of particles in the micron range.



**Figure 2.17:** Principle of the centrifugal counter current classifier (Schmidt, 2004)

The target of Schmidt's work was to design a classifier with the same separation efficiency like a gravity elutriator but with cut sizes down to few microns. On the contrary to the above presented prototypes the classifier of Schmidt is designed for suspension throughputs between 137 – 1900 l/h, which lies in the range of industrial demand (Schmidt, 2004). The rotor has a diameter of 1m and a circumferential classification chamber. The advantage of a circumferential classification chamber is the fact that a complete revolution, i.e. 360° of the rotor, is used for the separation. With a distributor area of 0.05592 m<sup>2</sup> the dimensions of the classifier are much larger



compared to those of Timmermann (1998) and Priesemann (1994). The principle of the chamber profile is based on the condition that the cut size has to be constant over the chamber height. As the cut size depends on the radial position in the classification chamber, the radial velocity has to be varied above the chamber height to maintain a constant cut size. Applying equation (2.8) leads to the conclusion that the ratio of the radial velocity and the radius has to be constant. The condition of constancy of the cut size was realized by Schmidt (2004) due to the design of the classification chamber.

According to Schmidt (2004) the existence of a fluidized bed is required for de-agglomeration and therefore the control of the bed height is one of the key tasks for the operation of the classifier. Schmidt selected needle valves operated with an elbow lever mechanism for the bed height control, which is presented in detail in chapter 3.

Schmidt conducted experiments to characterize the influences of the angular speed, the suspension to fluidizing water ratio and the influence of the suspension solids content. The experimental materials limestone and quartz with similar properties compared to the ones of the present work, were used by Schmidt. For the analysis of the particle size distributions a laser diffraction analyzer (Type HELOS 12 KA/LA, Sympatec Germany) was applied using the Fraunhofer model for evaluation.

The investigation of the influence of the angular velocity at a constant theoretical cut size (equation 2.8) was conducted by varying the water throughput depending on the angular velocity. Schmidt (2004) found that with increasing angular velocities the separation efficiency curves are shifted to larger particle diameters and the “fishhook effect” is reduced. Figure 2.18 shows a separation efficiency curve of limestone classification for different angular speeds at a fluidizing to suspension flow ratio of 2:1.

Further experiments were conducted to describe the influence of the fluidizing to volume flow ratio on the separation efficiency. Schmidt found that an increase of the ratio results in a higher separation efficiency and in a reduction of the fishhook. This can easily be seen in figure 2.19, where the fluidizing to suspension flow ratio was

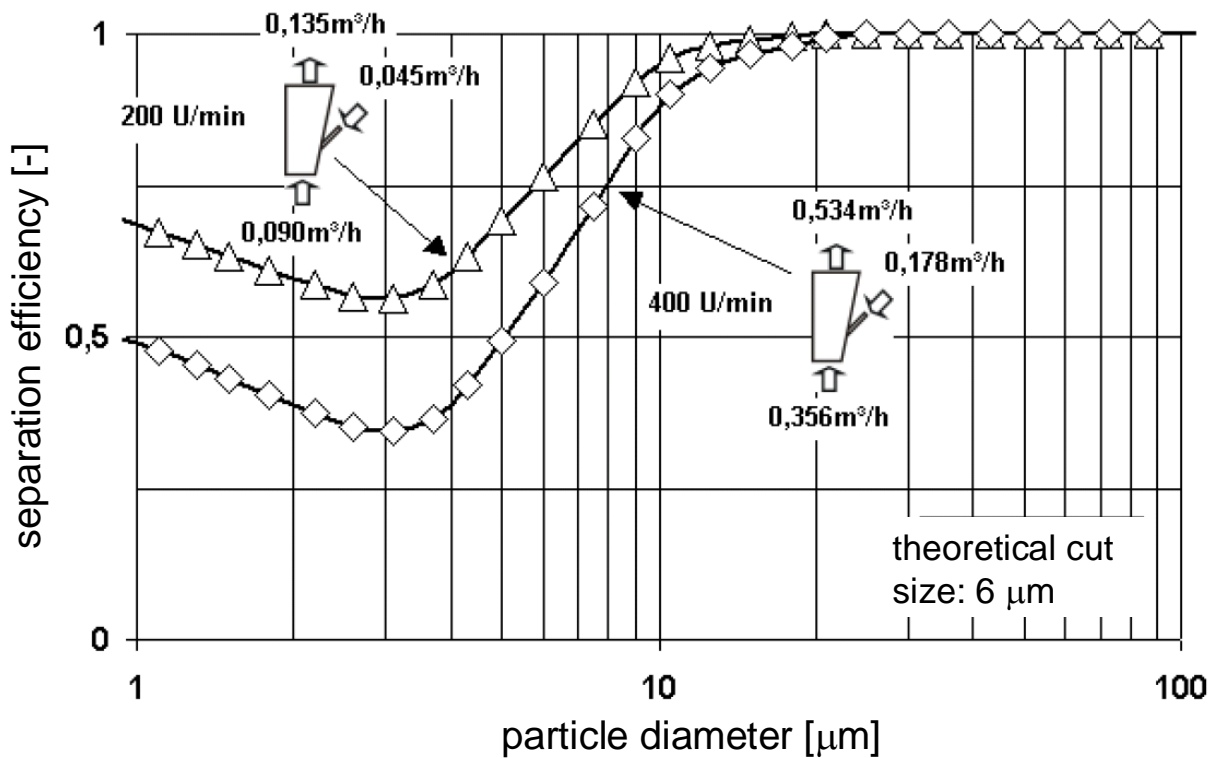


**Figure 2.18:** Influence of the angular speed on the separation efficiency (Schmidt, 2004)

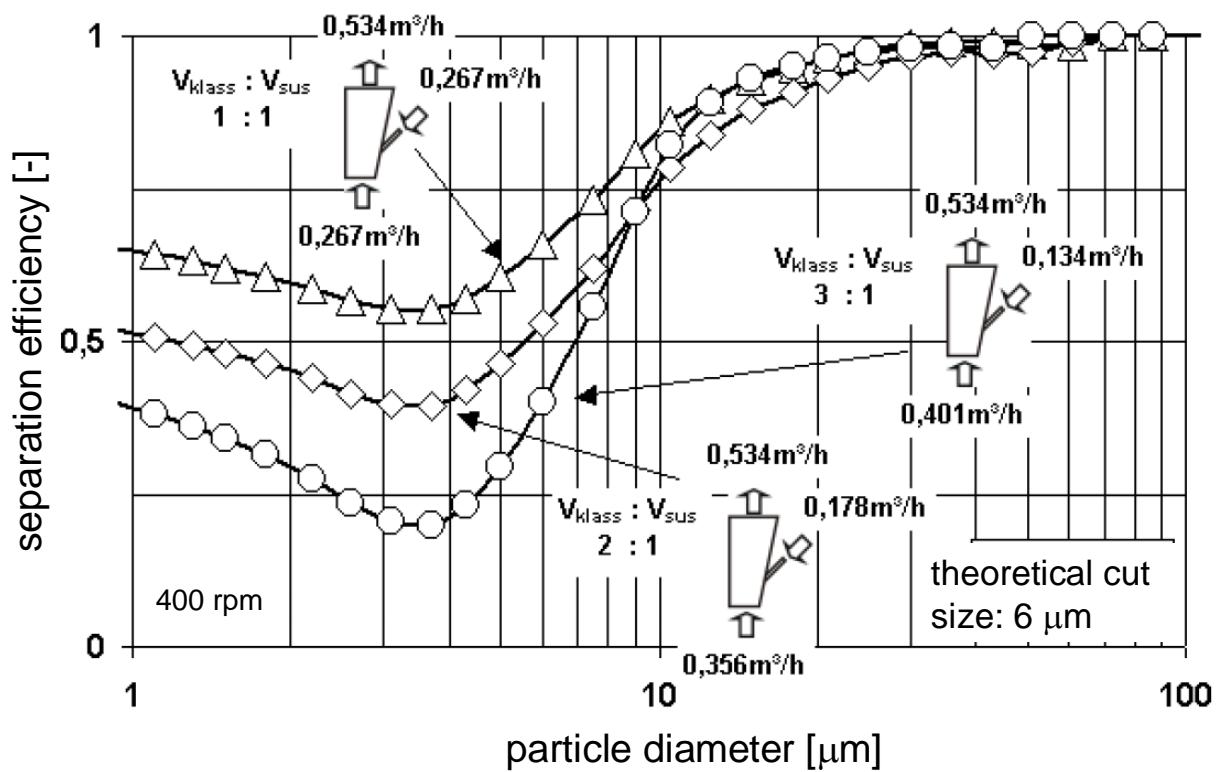


**Figure 2.19:** Influence of the fluidizing to suspension flow ratio on the separation efficiency (Schmidt, 2004)

varied for the classification of limestone at 400 rpm for a theoretical cut size of 6  $\mu\text{m}$ .

An influence of the feed solids concentration was studied as well, but Schmidt (2004) found no significant influence of the solids concentration on the separation performance.

Comparing the calculated cut sizes (equation 2.8) with the results of the experiments, Schmidt (2004) discovered an underestimation of the theoretical cut sizes, i.e. the measured cut sizes were almost always higher than the calculated ones. This is revealed in figure 2.20, where the measured cut sizes are plotted versus the calculated ones. Schmidt (2004) explained the deviation due to the occurrence of swarm settling instead of single particle settling in the classification zone of the freeboard, which was assumed in his model. The swarm settling leads to a reduction of the particle settling velocities, whereby the deviation of the calculated cut sizes to the experimental findings can be explained.

Although with the design of Schmidt (2004) cut sizes below 10  $\mu\text{m}$  were successfully reached, the sharpness of the classification was not satisfactory. Furthermore the separation efficiency curves by Schmidt revealed a strong “fishhook effect”, which could not be eliminated with the actual configuration of the classifier.

However, the principle of centrifugal elutriation has a high potential to fulfill the industrial demand for wet classification in the micron range. The classifier of Schmidt reaches the desired cut sizes as well as suspension throughputs for industrial applications. The elimination of the fishhook and the increase of the sharpness are therefore the key tasks for optimization. A problem with the classifier of Schmidt is that the needle valves, which are operated with an elbow lever mechanism, are not capable to control the bed height accurately. Another problem is the flushing out of the bed material, which lead to misclassification through bypassing of fines to the outlet.

Thus there is a lot of potential for optimization. Therefore the understanding of the fundamentals of the fluid mechanics and the wet centrifugal fluidization are essential. These fundamentals are not completely understood yet, so that their investigation is one of the key points of the present work.

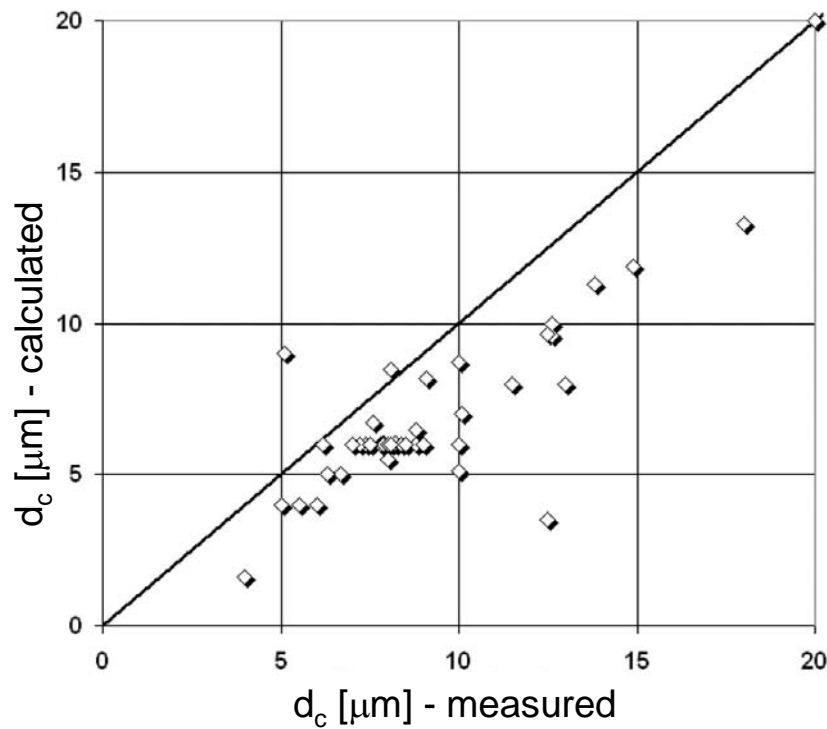


**Figure 2.20:** Comparison of the theoretical and experimental cut sizes (Schmidt, 2004)

In the following simulations of the pure liquid flow in a rotating chamber (i.e. according to the conditions in the solids-free chamber or in the freeboard of the fluidized bed, respectively) with the CFD software CFX will be performed and experiments will be carried out to verify the findings of the simulation and to describe the behavior of the fluidized bed. The characterization of the fluidized bed behavior will be conducted by the determination of its expansion and the pressure drop profile under different angular velocities. From the findings the classifier will be improved, especially an improvement of the coarse discharge is considered in this work, which plays an important role for the control of the bed height.

### **3 Setup and design of the centrifugal fluidized bed classifier**

In this chapter the setup of the classifier is presented, which is based on the previous work conducted by Schmidt (2004). The general data of the classifier are provided as well as a detailed explanation for the design of the classification chamber. The coarse discharge mechanism of Schmidt (2004) is presented, which plays an important role in separation performance. The coarse discharge is modified later, which is part of chapter 5.

#### **3.1 Experimental setup**

The classification process takes place in the classifier pictured in figure 3.1. The rotor with an outer diameter of 1 m can be operated up to 1000 rev/min, so that centrifugal accelerations above 500 times the gravity can be reached. The rotor is mounted to two bearings on opposite sides and driven by a direct current motor with a power rating of 6 kW. For continuous classification the fluidizing water and the suspension have to be introduced permanently into the classifier during operation. This is done by rotary feedthroughs, which are connected to a hollow shaft at the axis of the rotor. Suspension and fluidizing water are fed from opposite sides into the rotor and then distributed to the classification chamber by four radially oriented pipes, respectively. While the suspension is directly fed into the classification chamber, the fluidizing water is channelled to a distribution chamber. From there the fluidizing water enters the classification chamber through a porous distributor plate. In the classification chamber the particles of the suspension are split into coarse and fines. The fines suspension leaves the classification chamber via an overflow weir and the coarse accumulate in a fluidized bed and are then taken out through a coarse discharge mechanism. The coarse discharge is originally operated by 4 needle valves (figure 3.2). The 4 needle

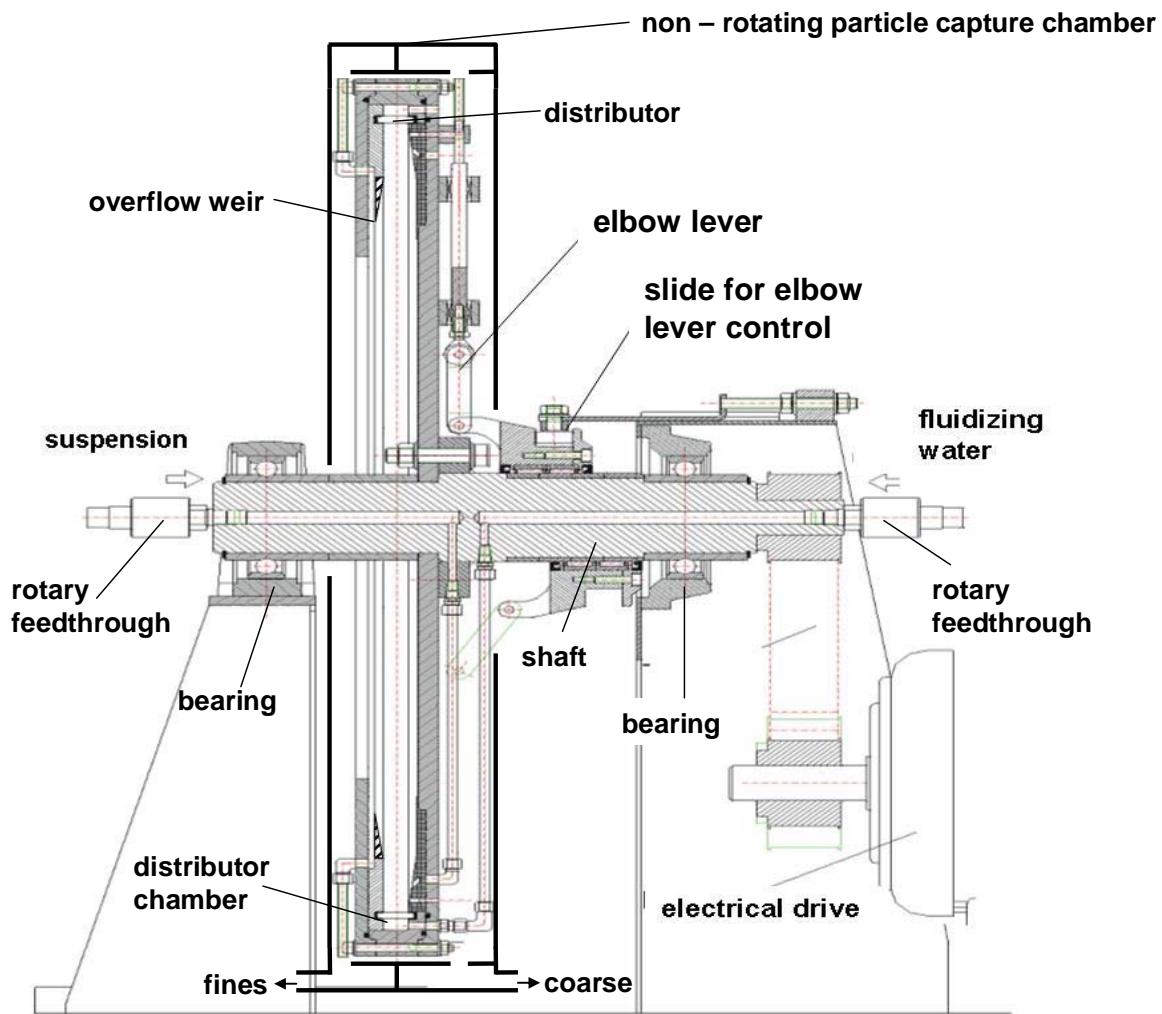


**Figure 3.1:** Design of the centrifugal fluidized bed classifier

valves are connected with an elbow lever mechanism to a ring, which can be moved on the shaft. A non-rotating slide with a wheel running in the ring enables the movement of the ring, which opens or closes the needle valves. The coarse discharge mechanism has a strong influence on the performance of the classifier and will be modified later according to the findings of the investigation of the fluid (chapter 5). The coarse and the fines are captured in a non-rotating ring chamber made of plexiglass. The ring chamber is divided into two sections, one for the coarse, the other one for the fines fraction. The fines and the coarse suspension leave the ring chamber at the bottom from opposite sides. Photographs of the classifier are shown in figure 3.3 (left: frontview; right: backview). The operational parameters are summarized in table 3.1 (Schmidt and Werther, 2005).

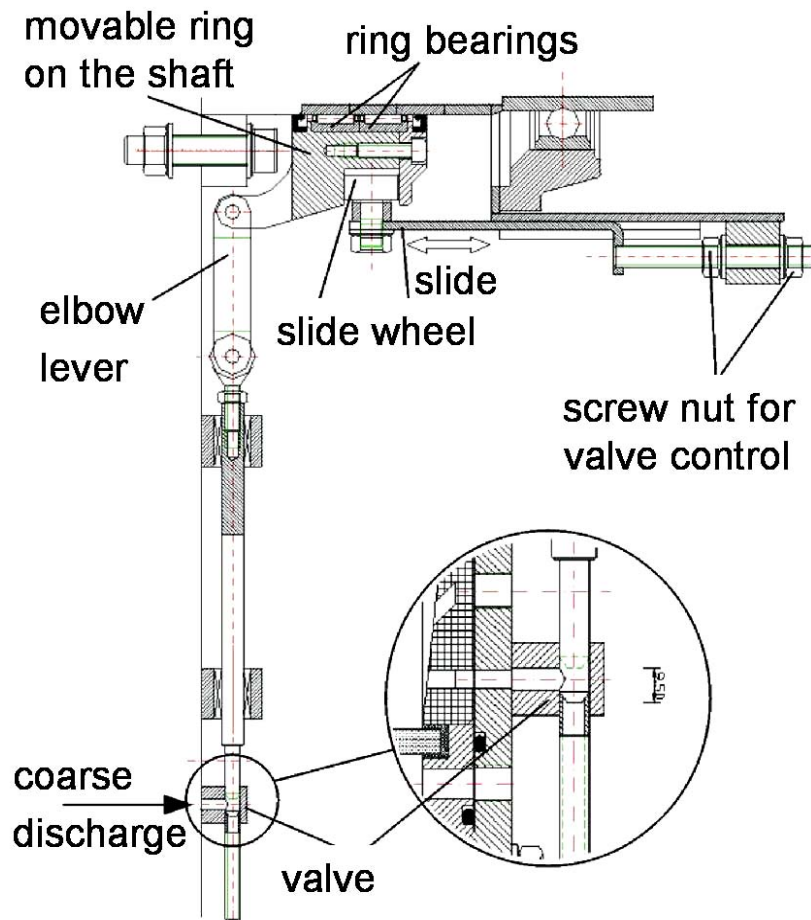


**Figure 3.2:** Coarse discharge with needle valves

Rotating speed	200 – 1000 rpm
Outer diameter of rotor	1.00 m
Outer diameter classification chamber	0.89 m
Suspension feed flow	0.137 – 1.9 m <sup>3</sup> /h
Classification or fluidizing water flow	0.150 – 2.3 m <sup>3</sup> /h
Centrifugal acceleration	20 – 500 g
Theoretical cut sizes (at 2650 kg/m <sup>3</sup> density)	1.5 – 25 μm

**Table 3.1:** Parameters of the centrifugal fluidized bed classifier

The complete experimental setup is presented in figure 3.4. The feed suspension is prepared in a storage vessel, which can hold 200 l of suspension. To prevent sedimentation the vessel is equipped with a stirrer. The suspension is pumped by a

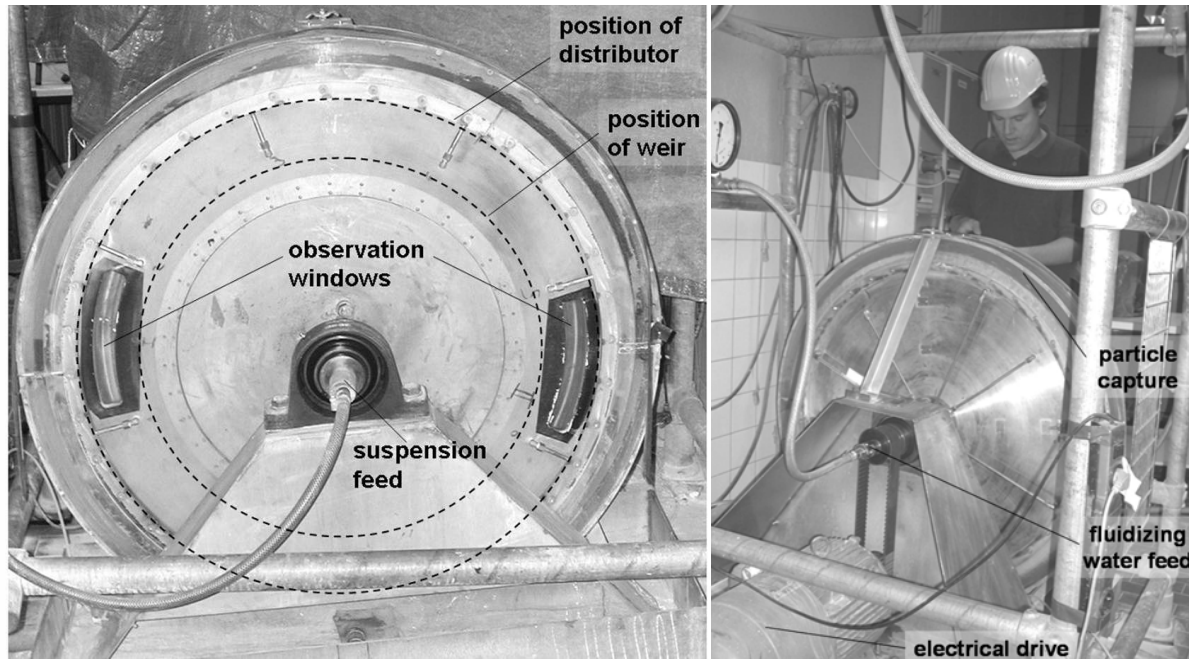


**Figure 3.3:** Photograph of the centrifugal fluidized bed classifier from the front (left) and back (right)

spiral pump (pump 1) with a maximal throughput of 700 l/h, the volume flow is measured by a magnetic flow meter (FI 1). A pressure gauge (PI 1) is installed behind the spiral pump as a safety device to indicate overpressure. The three way valve V1 is used to switch from backflow to the suspension vessel (bypass) to the classifier. The bypass is needed during startup to adjust the desired volume flow and to maintain the flow rate until the classifier is ready for operation.

The fluidizing water is taken from the water tap, a pump (pump 2) behind the tap is installed to enhance the maximum outtake up to 2800 l/h. The fluidizing water flow is adjusted by the valve V2 and the magnetic flow meter FI2. To adjust the flow before operation the flow can be switched to the drain by the three way valve V3. As the



desired flow is reached V3 can be switched to the classifier. A pressure gauge (PI2) indicates the pressure in front of the fluidizing water feedthrough.

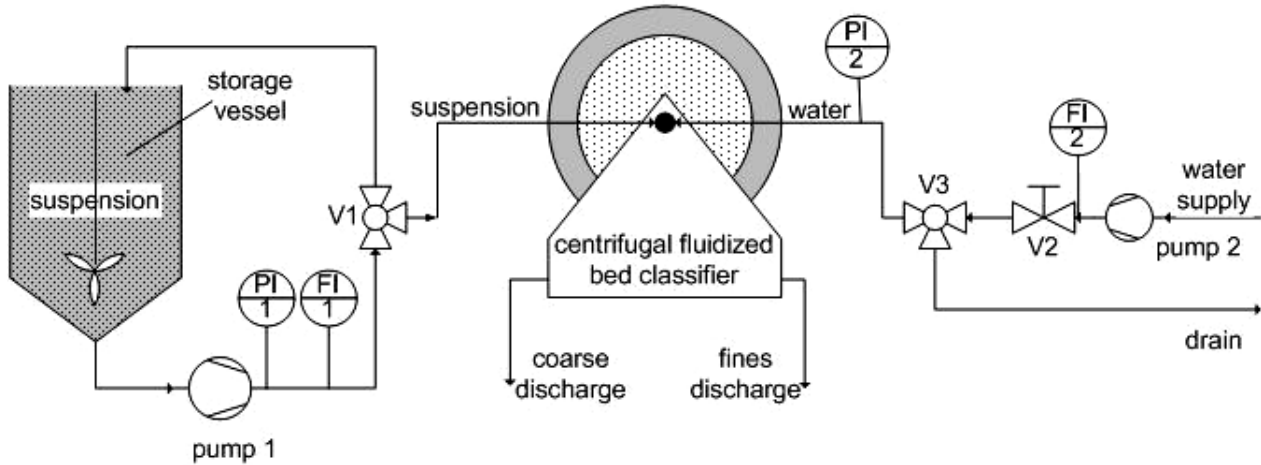


**Figure 3.4:** Experimental setup

### 3.2 The geometry of the classification chamber

The most important part is the circumferential classification chamber, where the split of the suspension into coarse and fines takes place. The design and the dimensions of the classification chamber are shown in figure 3.5.

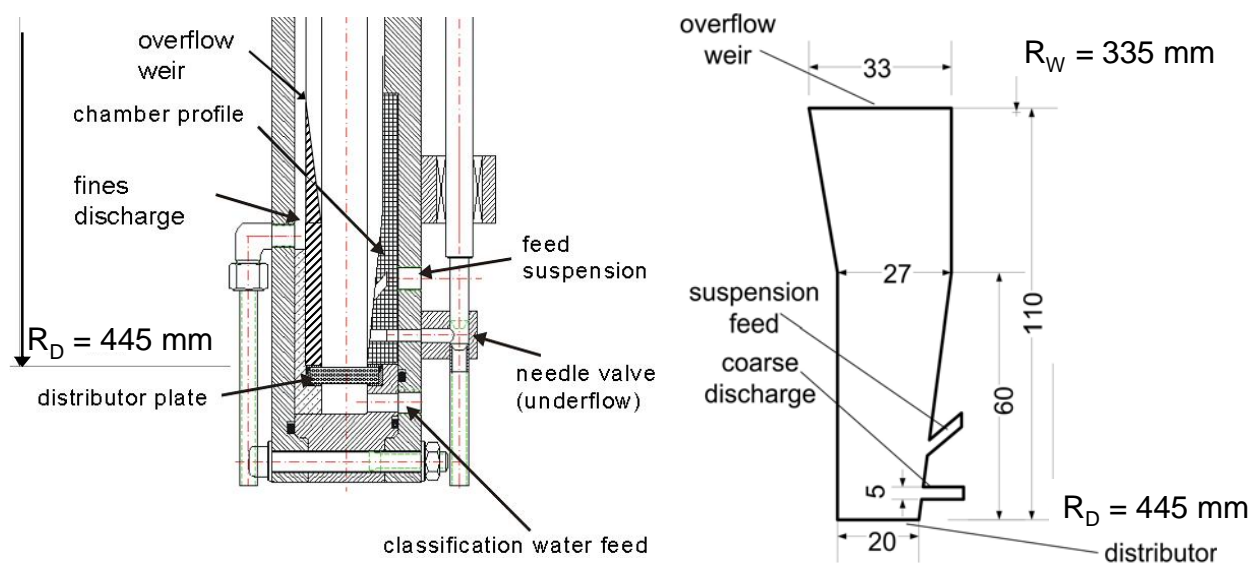


**Figure 3.5:** Drawing (left) and sketch (right) of the classification chamber

The suspension is injected to the classification chamber by 4 ports, 30 mm above the distributor at an angle of 45°. The injected particles inside the chamber are affected by a counter current, which causes the classification effect. While the coarse particles accumulate in the fluidizing bed, the fines are carried with the radial flow to the overflow weir. The fluidizing water is distributed across the circumference by a ring chamber and enters the classification chamber through a 8 mm thick porous distributor (CELLPOR – TYPE 152, Porex Technologies GmbH, Singwitz, Germany). The distributor has a linear pressure drop characteristics up to a fluid velocity of 0.02 m/s. The pressure drop at 0.02 m/s is 0.42 bar.

The classification chamber is equipped with two windows made from plexiglass (cf. figure 3.3), which enables the observation of the fluidized bed and particularly its freeboard with the help of a stroboscope and a high-speed camera (KODAK EKTAPRO). The camera is able to take up to 1000 frames per second.

The cut size  $d_c$ , i.e. the condition where the drag on a single particle equals the centrifugal force minus the buoyancy force is one of the most important aspects of classification. It determines the profile of the classification chamber and the operating conditions. Inserting the cross sectional area  $A_C$ , with

$$A_C = 2 \pi \cdot r \cdot B; \quad (3.1)$$

and with the chamber width  $B$ , into equation (2.8), it follows:

$$d_c = \sqrt{\frac{18 \cdot \eta}{(\rho_s - \rho_L) \cdot \omega^2 \cdot r} \cdot \frac{\dot{V}}{2 \cdot \pi \cdot r \cdot B}} \quad (3.2)$$

As a constant cut size is desired for all radial positions the product  $r^2 \cdot B$  must be kept constant. Therefore the width  $B$  of the chamber has to be reduced with increasing

distance from the axis. The resulting parabolic profile was approximated by two linear sections to facilitate manufacturing of the classification chamber (cf. figure 3.5). The deviation of the approximated chamber profile from the ideal profile was always below 2% (Schmidt 2004) and thus the assumption of a constant cut size over the chamber height is valid.

## 4 Theory

With the centrifugal fluidized bed classifier a novel system was designed to perform particle separation in the micron range. The classification takes place in a circumferential classification chamber, in which the fluid and the bed can freely move in tangential direction. The fluid enters the chamber in radial direction at the distributor (radial position of the distributor:  $R_D = 0.445$  m) and leaves it at the weir (radial position of the weir:  $R_W = 0.335$  m). The centrifugal acceleration varies with the distance from the axis and furthermore the flow is affected by the Coriolis force, which reaches high values at high angular speed rates.

The Coriolis force describes the influence of the rotation on an object in motion in a rotating reference frame. The Coriolis force is proportional to the speed of rotation and to the mass and the velocity of the object. The Coriolis force acts in a direction perpendicular to the rotation axis and to the velocity of the object in the rotating frame.

The Coriolis force vector  $\vec{S}_{cor}$  is defined:

$$\vec{S}_{cor} = -2m \cdot \vec{\omega} \times \vec{U}, \quad (4.1)$$

where  $m$  is the mass of the object,  $\vec{\omega}$  the angular velocity vector and  $\vec{U}$  the velocity vector of the object in the rotating reference frame.

Little research was done in the past to describe a flow in such a system. Schmidt (2004) assumed the Coriolis force to be negligible and conducted CFD – simulations for pure liquid flow without the Coriolis force. His results showed a radially oriented flow pattern, which was only influenced by the suspension injection ports.

As the Coriolis force acts perpendicular to the centrifugal force, i.e. in tangential direction, it can be expected, that the Coriolis force has a significant influence on the flow pattern in the annular chamber. A significant influence of the Coriolis force would

induce a velocity component in tangential direction. These expectations are contrary to Schmidt's (2004) assumptions and have to be investigated. In this chapter the theory of the computational investigation of the single phase liquid flow (water) is presented. For a rough estimation a simplified model was developed and the results are compared with a precise CFD simulation with the software CFX 5.7.

#### 4.1 A simplified hydrodynamic model of the liquid flow in the solids-free chamber (model I)

The model presented in this section describes the induction of tangential movement relative to the wall from the distributor in the direction to the overflow weir. The observer in this model is located outside, i.e. the velocity of the rotor is as well considered as the tangential flow.

The principle underlying this model is to apply the conservation of angular momentum (Dixon, 1998) on a ring element with the thickness  $dr$ . The massflow  $\dot{m}$  passes the ring element with the thickness  $dr$  in radial direction (figure 4.1). For the momentum balance the angular momentum  $M_F$  of the flow into the element, the angular momentum  $M_O$  of the flow out of the element and the torque  $M_W$  caused by wall friction have to be considered. The viscous momentum transfer between ring elements is neglected, since the velocity gradient between the walls is much higher than from the distributor to the weir and therefore the radial viscous momentum transfer is considered to be small compared to the wall friction. Conservation of angular momentum on a ring element with thickness  $dr$  means

$$\dot{m} \cdot (w + dw) \cdot (r + dr) - M_W - \dot{m} \cdot w \cdot r = 0 , \quad (4.2)$$

where  $\dot{m}$  is the fluid mass flow,  $w$  the absolute tangential velocity,  $r$  the radius and  $M_W$  the torque with regard to the axis.

Transforming equation (4.2) results in:

$$\dot{m} \cdot (r \cdot dw + w \cdot dr) = M_W \quad (4.3)$$

The angular torque  $M_W$  is a product of wall friction force  $F_W$  and radius  $r$ ,

$$M_W = F_W \cdot r \quad (4.4)$$

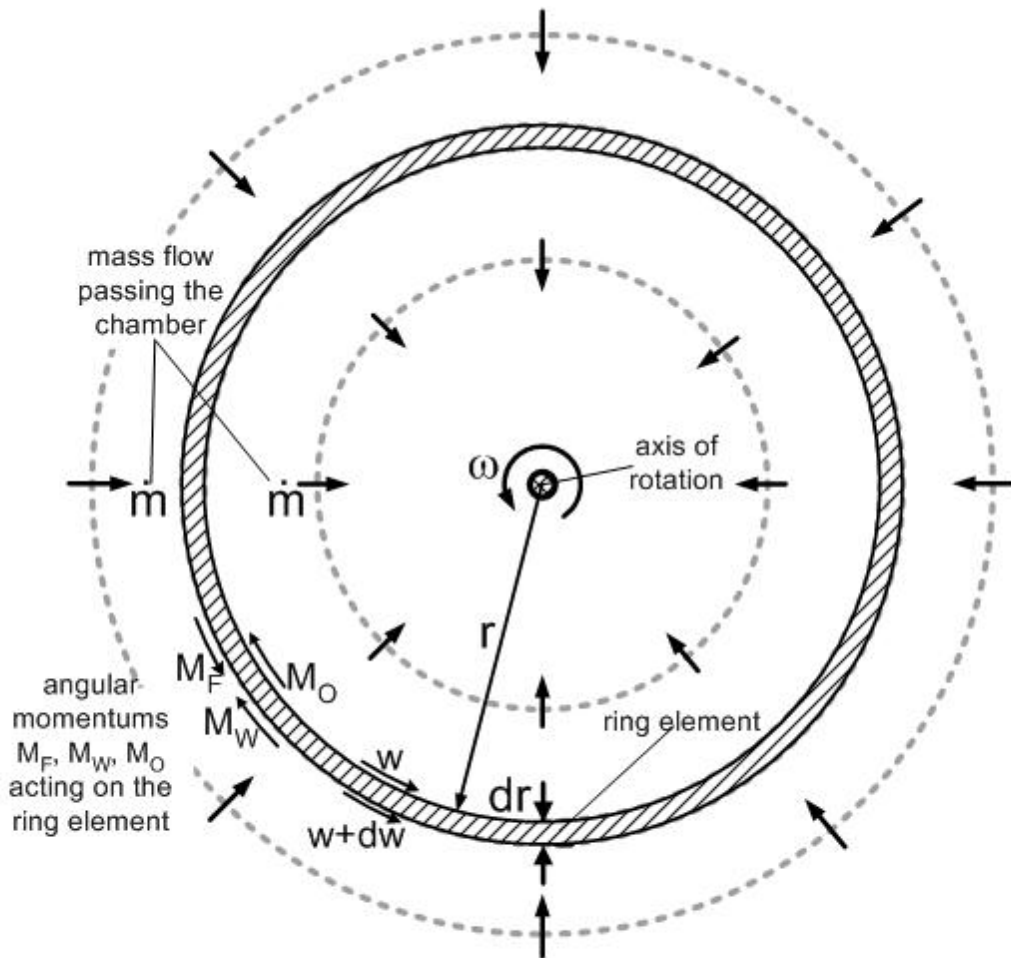


**Figure 4.1:** Balance of angular momentum on a ring element of the liquid in the classification chamber

The wall friction force can be derived from the pressure loss  $\Delta p$  for a through-flow system (Bohl, 1991):

$$\Delta p = 0.5 \cdot \lambda \cdot L/d_h \cdot \rho \cdot v_T^2, \quad (4.5)$$

where  $L$  is the circumference,  $d_h$  the hydraulic diameter,  $v_T$  the velocity of the fluid relative to the wall and  $\lambda$  the wall friction coefficient.

The pressure loss  $\Delta p$  equals the wall friction  $F_W$  divided by the cross sectional surface  $A_Q$ .

$$F_W = \Delta p \cdot A_Q \quad (4.6)$$

The relative tangential velocity  $v_T$  between the fluid and the wall is replaced by the absolute velocity  $w$  of the fluid minus the velocity of the wall at the radial position  $r$ .

$$v_T = w - r \cdot \omega, \quad (4.7)$$

where  $r$  is the radial position and  $\omega$  the angular velocity. It follows

$$F_W = 0.5 \cdot \lambda \cdot L/d_h \cdot \rho \cdot A_Q \cdot (w - r \cdot \omega)^2, \quad (4.8)$$

The hydraulic diameter  $d_h$  for slit flow (Schröder, 2004) results from the chamber width  $B$ :

$$d_h = 2 \cdot B(r) \quad (4.9)$$

It holds

$$A_Q = B(r) \cdot dr; \quad (4.10)$$

and

$$L(r) = 2 \cdot \pi \cdot r \quad (4.11)$$

which leads for the wall friction force of the ring element to

$$F_W = 0.5 \cdot \lambda \cdot \pi \cdot \rho \cdot (w - r \cdot \omega)^2 \cdot r \cdot dr \quad (4.12)$$

It follows for the torque

$$M_W = 0.5 \cdot \lambda \cdot \pi \cdot \rho \cdot (w - r \cdot \omega)^2 \cdot r^2 \cdot dr \quad (4.13)$$

Inserting equation (4.13) into equation (4.3) results in

$$\dot{m} \cdot (r \cdot dw + w \cdot dr) = 0.5 \cdot \lambda \cdot \pi \cdot \rho \cdot (w - r \cdot \omega)^2 \cdot r^2 \cdot dr \quad (4.14)$$

which leads to

$$dw = \frac{M_W - \dot{m} \cdot w \cdot dr}{\dot{m} \cdot r} \quad (4.15)$$

or

$$dw = \left[ \frac{\lambda \cdot \pi \cdot \rho \cdot (w - r \cdot \omega)^2 \cdot r}{2 \cdot \dot{m}} - \frac{w}{r} \right] dr \quad (4.16)$$

The calculation of profile of the tangential velocity along the height of the chamber was conducted in the following way: the starting point of the calculation of the tangential velocity distribution is at the distributor. At this point the tangential velocity of the fluid equals the velocity of the apparatus, i.e.  $v_T = 0$  m/s.

$$w(R_D) = R_D \cdot \omega \quad (4.17)$$

With equation (4.16) the change  $\Delta w$  of the absolute tangential velocity of the fluid after the distance  $-\Delta r$  can be calculated. With  $\Delta w$  from equation (4.16) the starting value for the next iteration is then given by:

$$w(r = R_D - \Delta r) = w(r = R_D) + \Delta w \quad (4.18)$$

The local relative tangential velocity  $v_T(r)$  can be calculated as the difference between the tangential velocity of the apparatus and the absolute tangential velocity of the fluid.

## 4.2 CFD simulation of the pure liquid flow (model II)

The CFD simulation is a complex Eulerian flow calculation and is used to predict flow patterns. It is presently used to confirm the validity of the simplified model and to give more detailed information about the flow behavior inside the classification chamber. For this purpose the CFD software CFX 5.7 by ANSYS, Inc. was used. Due to complexity a single phase model with water as liquid phase is considered only. This chapter consists of two parts, the geometry and the CFD model part. In chapter 4.2.1 the geometry and the grid as well as cell types are presented. Chapter 4.2.2 describes the equations to be solved in each cell of the domain and the turbulence model. The domain is the body of the geometry, in which the fluid flow is calculated. The calculation of the CFD model was conducted for an observer inside the system, i.e.



only the velocities relative to the rotating reference frame are considered. The effect of the rotation on the flow pattern is contributed by adding centrifugal and Coriolis force terms to the Navier-Stokes equations.

#### 4.2.1 Geometry and computational grid

Because a single-phase model is used only, the suspension feed and the coarse discharge can be neglected for the determination of the flow pattern. For the determination of a general tangential flow pattern this simplification is valid as the flow through the distributor to the weir is much larger than the flow through the feed and discharge ports. The modeling of the classification of particle collectives this way is too inaccurate as local radial velocities in the near discharge and feed port regions play an important role for classifications. Therefore simulations of classifications were not conducted in this work. Neglecting the feed and discharge ports, the classification chamber becomes completely rotational symmetric to the axis. Due to symmetry it is possible to consider just a small section of the classification chamber for the CFD – model. As the total amount of cells for this model was limited to approximately 300000 cells due to the available computing power, it is advisable to use a section less than  $10^\circ$  of the whole classification chamber to achieve a sufficient cell number in the model. This enables a high mesh refinement, especially in the near wall region, where high shear stresses occur. A higher number of cells would result in an unacceptably high calculation time.

Figure 4.2 shows the domain of the model used for the calculation, which is defined as a rotating reference frame, meaning that the calculated velocities are related to the wall velocity. At the front and back of figure 4.2 the side walls are visible. The wall surfaces are defined as no slip walls, i.e. the velocity is zero. The left and right surfaces of the domain are modeled as periodic boundaries. Periodic boundary condition means that a value transported over the periodic boundary will reenter the

geometry at the corresponding other periodic boundary. The periodic boundary condition is valid for a completely rotationally symmetric system. The shapes of the periodic boundary surfaces are identical to the real chamber profile, like presented in figure 3.5 (right), but without feed and coarse discharge.

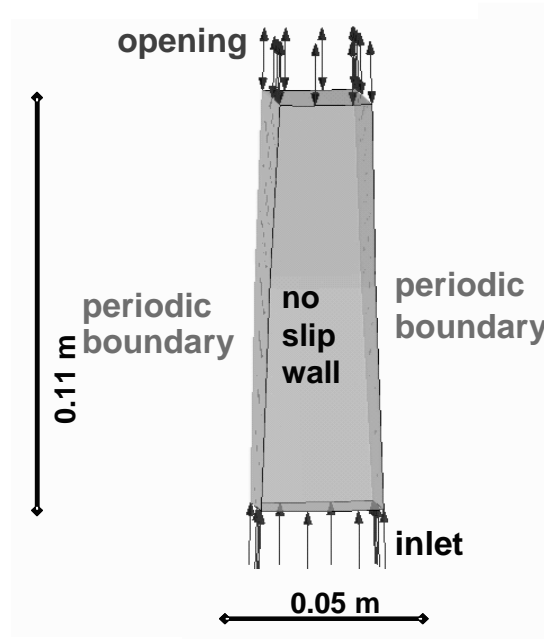


**Figure 4.2:** Frame of the CFD model for the calculation of the liquid flow in the classification chamber

In the real chamber a porous distributor plate is used as water inlet. To simplify the calculation and to increase the robustness of the solver the porous distributor is not considered. Instead the inlet with a constant velocity in radial direction only is assumed.

At the top of the chamber the fluid leaves the fluid domain. This boundary is modeled as an opening with a relative pressure of 0 Pa. The opening boundary condition allows the fluid to leave and also to enter the domain. Although only a flow out of the domain is possible, the opening condition achieves a higher stability of the solver (CFX Manual, 2004).

Figure 4.3 shows the hexahedral mesh on the domain surfaces. A hexahedral mesh was chosen, because the solver shows a faster convergence of the equation system than with a tetrahedral mesh, what was tested on the domain of figure 4.2. Another reason for using a hexahedral mesh is the fact, that a more effective mesh refinement in the near wall region is achieved.

The refinement of the mesh in the wall region, where the highest velocity gradients occur and shear stresses occur, can be seen in figure 4.3. A cell width of 0.1 mm in that region is achieved, which is necessary for an accurate modeling. The whole grid of the chamber consists of 236,811 hexahedron cells and has a height of 110 mm and a width of 20 to 33 mm.

The geometry presented above is valid for a circumferential classification chamber, i.e. the fluid can move freely in tangential direction. Previous works (Timmermann, 1998; Priesemann, 1994) dealt with a closed classification chamber, i.e. the fluid is surrounded by four walls while passing through the classification chamber. The question arises, how the flow is influenced in a closed system by the rotational forces in such a system. A simulation with a closed system can be easily carried out by replacing the periodic boundaries of figure 4.2 by no slip walls. The fluid mechanics of that system were also investigated in the present work.

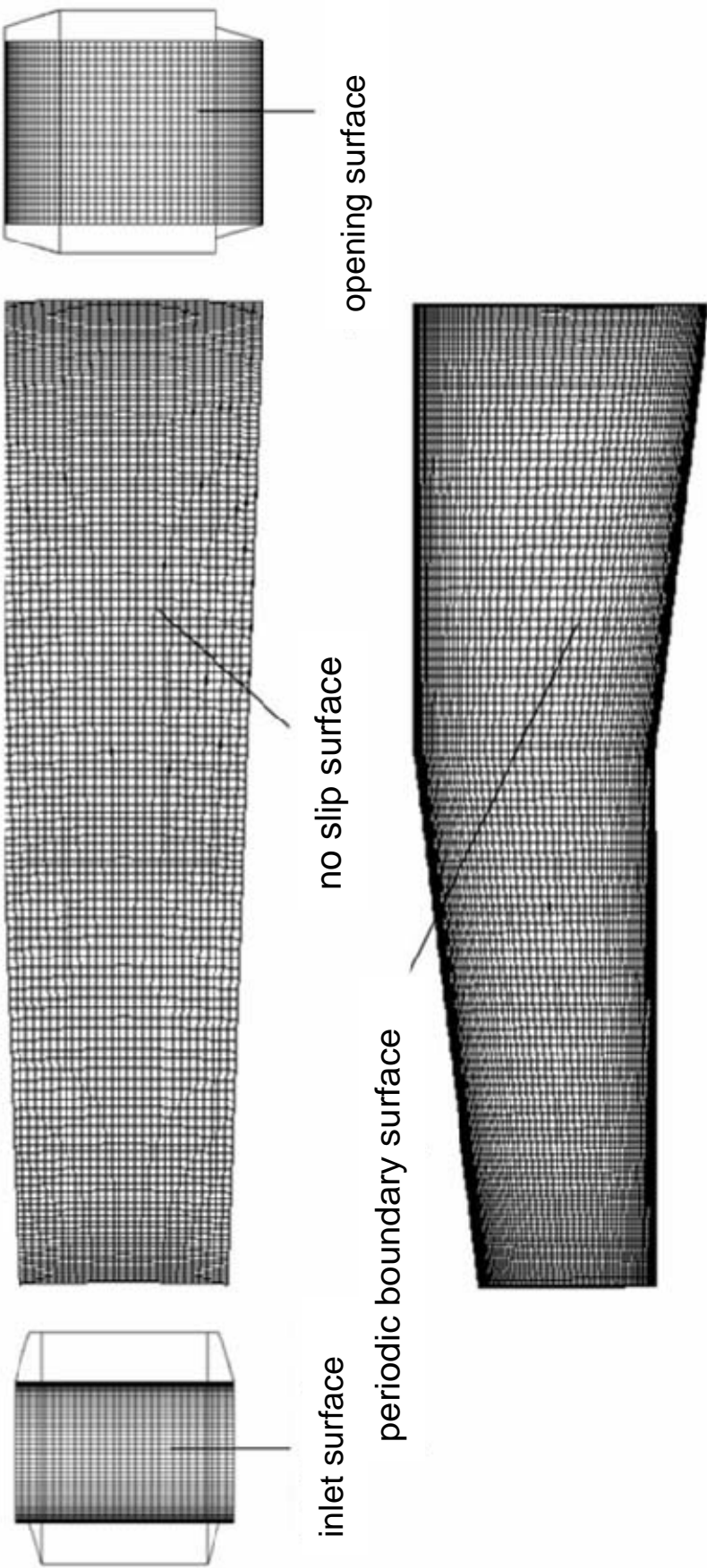


Figure 4.3: Hexahedral mesh of the CFD model

### 4.2.2 The CFD model

The domain consists of a multitude of cells. For each of them the conservation equations of a turbulent flow are calculated. A turbulent flow means that instationary fluctuations are governing the flow pattern and thus for the calculation the velocity is divided into a stationary and instationary part:

$$\vec{U} = \vec{\bar{U}} + \vec{u} \quad (4.19)$$

The velocity of equation (4.19) is implemented in the conservation equation of CFX and averaged which leads to the RANS(Reynolds Averaged Navier Stokes)-equations:

$$\text{Conservation of mass: } \frac{\partial \rho}{\partial t} + \nabla \bullet (\rho \vec{U}) = 0 \quad (4.20)$$

$$\text{Conservation of momentum: } \frac{\partial \rho \vec{U}}{\partial t} + \nabla \bullet (\rho \vec{U} \otimes \vec{U}) = \vec{B} - \nabla p + \nabla \bullet (\mu_{eff} (\nabla \vec{U} + (\nabla \vec{U})^T)) \quad (4.21)$$

The first term of the equations (4.20) and (4.21) is the transient terms, which becomes zero for stationary applications, while the second term describes the transportation due to convection.  $\vec{B}$  is the body force term, which contains gravity, centrifugal force, Coriolis force etc.

In this model the body force term consists of the centrifugal  $\vec{S}_{cfg}$  and Coriolis force  $\vec{S}_{cor}$  term only:

$$\vec{B} = \vec{S}_{cor} + \vec{S}_{cfg} \quad (4.22)$$

The Coriolis force and the centrifugal force are calculated from

$$\text{Coriolis force: } \vec{S}_{cor} = -2 \rho \vec{\omega} \times \vec{U} \quad (4.23)$$

$$\text{Centrifugal force: } \vec{S}_{cfg} = -\rho \vec{\omega} \times (\vec{\omega} \times \vec{r}) \quad (4.24)$$

where  $\vec{r}$  is the location vector and  $\vec{U}$  is the relative frame velocity.

The second term on the right side of equation (4.21) is the momentum transfer by pressure gradients. The third term on the right of equation (4.21) represents the diffusive momentum transport by shear stresses. The shear stresses due to turbulence is contained in the effective viscosity  $\mu_{\text{eff}} = \mu + \mu_t$ , with the bulk viscosity  $\mu$  and the turbulent viscosity  $\mu_t$ .

The used k- $\Omega$  model assumes that the turbulent viscosity is linked to the turbulent kinetic energy  $k$  and turbulent frequency  $\Omega$  via the relation:

$$\mu_t = \rho \cdot k / \Omega \quad (4.25)$$

The starting point of the present formulation is the k- $\Omega$  model developed by Wilcox (Manual CFX 5.7, 2004). It solves two transport equations, one for the turbulent kinetic energy,  $k$ , and one for the turbulent frequency,  $\Omega$ .

Turbulent kinetic energy:

$$\frac{\partial(\rho k)}{\partial t} + \nabla \cdot (\rho \vec{U} k) = \nabla \cdot \left[ \left( \mu + \frac{\mu_t}{\sigma_k} \right) \nabla k \right] + P_k - \beta' \rho k \Omega \quad (4.26)$$

Turbulent frequency:

$$\frac{\partial(\rho \Omega)}{\partial t} + \nabla \cdot (\rho \vec{U} \Omega) = \nabla \cdot \left[ \left( \mu + \frac{\mu_t}{\sigma_\Omega} \right) \nabla \Omega \right] + \alpha' \frac{\Omega}{k} P_k - \beta \rho \Omega^2 \quad (4.27)$$

$P_k$  is the turbulence production due to viscous forces, which is modelled using:

$$P_k = \mu_t \nabla \vec{U} \cdot (\nabla \vec{U} + \nabla \vec{U}^T) - \frac{2}{3} \nabla \cdot \vec{U} (3 \mu_t \nabla \cdot \vec{U} + \rho k) \quad (4.28)$$

The model constants are given by:

$$\beta' = 0.09; \alpha' = 0.5556; \beta = 0.075; \sigma_k = 2; \sigma_\Omega = 2$$

The equation system (4.19) – (4.28) is solved by the finite volume method in each cell of the grid. Additionally, to compare the influence of the fluid a simulation with air was conducted. In the simulations water (density  $\rho = 999 \text{ kg/m}^3$ ; dynamic viscosity  $\eta = 0.0013 \text{ kg/m s}$  at  $10^\circ\text{C}$ ) and air at ambient conditions (density  $\rho = 1.2 \text{ kg/m}^3$ ; dynamic viscosity  $\eta = 0.0018 \text{ kg/m s}$ ) were used.

## **5 Experimental**

In this chapter the techniques to measure the properties of the centrifugal fluidized bed are presented. Particularly the measurement of the fluid dynamics is of major interest to confirm the results of the simulation and to gain knowledge of the influence of the particles in the fluid. As already mentioned in chapter 4 a strong velocity in the circumferential direction is expected due to the Coriolis force. The available simulation techniques only consider a single phase flow, so measurements are necessary to find out about the influence of particles on the flow pattern. In this regard the methods to determine the flow behavior of the freeboard and of the fluidized bed will be presented. Furthermore the techniques for measuring the bed pressure drop and the expansion behavior will be explained. The measurement and the modeling of the bed pressure drop profile depending on the fluidizing velocity are important to find the limiting cut sizes for classifications. The pressure drop profiles reveal the minimal fluidizing velocities at given conditions, where the bed is stably fluidized. Below the minimum fluidization point the operation of the classifier is not recommended as defluidized zones reduce the classification performance or completely block the coarse discharge. To model the pressure drop profile, the knowledge of the expansion behavior is necessary. This enables the calculation of the bed height from the pressure drop and allows an estimation of the flow through the modified coarse discharge. Other topics of this chapter are the presentations of the coarse discharge modifications as well as the analysis methods and the bed materials used in the experiments.

### **5.1 Experimental materials**

For the experimental investigation of the centrifugal fluidized bed and for the characterization of the classification performance suitable materials had to be chosen. Limestone and quartz powder are often used for this purpose, because they are

cheap, available in many particle sizes and are not dissolvable or reactive in aqueous media. With densities between  $2500 \text{ kg/m}^3$  and  $3000 \text{ kg/m}^3$  quartz and limestone are good to handle and have adequate settling velocities for classification in the micron range. Other advantages of limestone and quartz are that they are 99.9 % pure and well studied, i.e. properties like the refraction index, which is important for the determination of the particle size distribution by the laser diffraction analysis, are documented in the literature. Thus they were used in this work. The quartz powder (SF300, Quarzwerke Frechen, Frechen Germany) had as density of  $2650 \text{ kg/m}^3$  and a refraction index of 1.54 (specification of the producer). Quartz was used for the determination of the tangential bed movement, for the bed expansion and for classification experiments. Limestone (Saxolith 10HE, Geomin, Hermsdorf/Germany) with a density of  $2620 \text{ kg/m}^3$  and a refraction index of 1.59 was used for bed expansion and classification experiments. Limestone and quartz are natural products and have therefore irregular shapes. To compare the findings of the investigations of quartz and limestone with spheres, glass beads (Strahlperlen 0-50  $\mu\text{m}$ , Strahlperlen Auer GmbH, Mannheim/Germany) with a density of  $2500 \text{ kg/m}^3$  and a refraction index of 1.50 were used for classification experiments and for the determination of the expansion behavior. The particle size distributions of the used materials are shown in figure 5.1 and photographs by a scanning electron microscope (SEM) in figure 5.2.

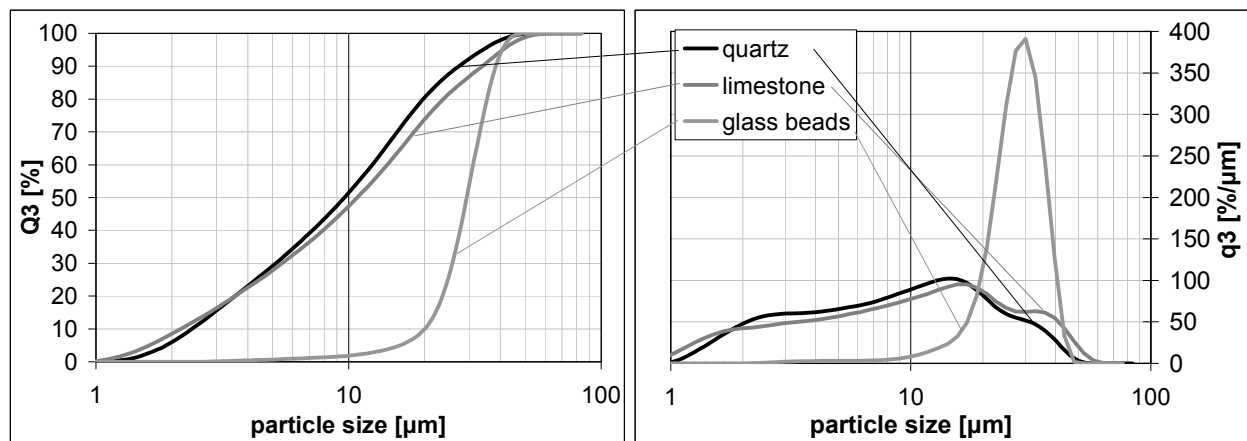


**Figure 5.1:** Cumulative mass (left) and mass density (right) distributions of the experimental materials quartz, limestone and glass beads



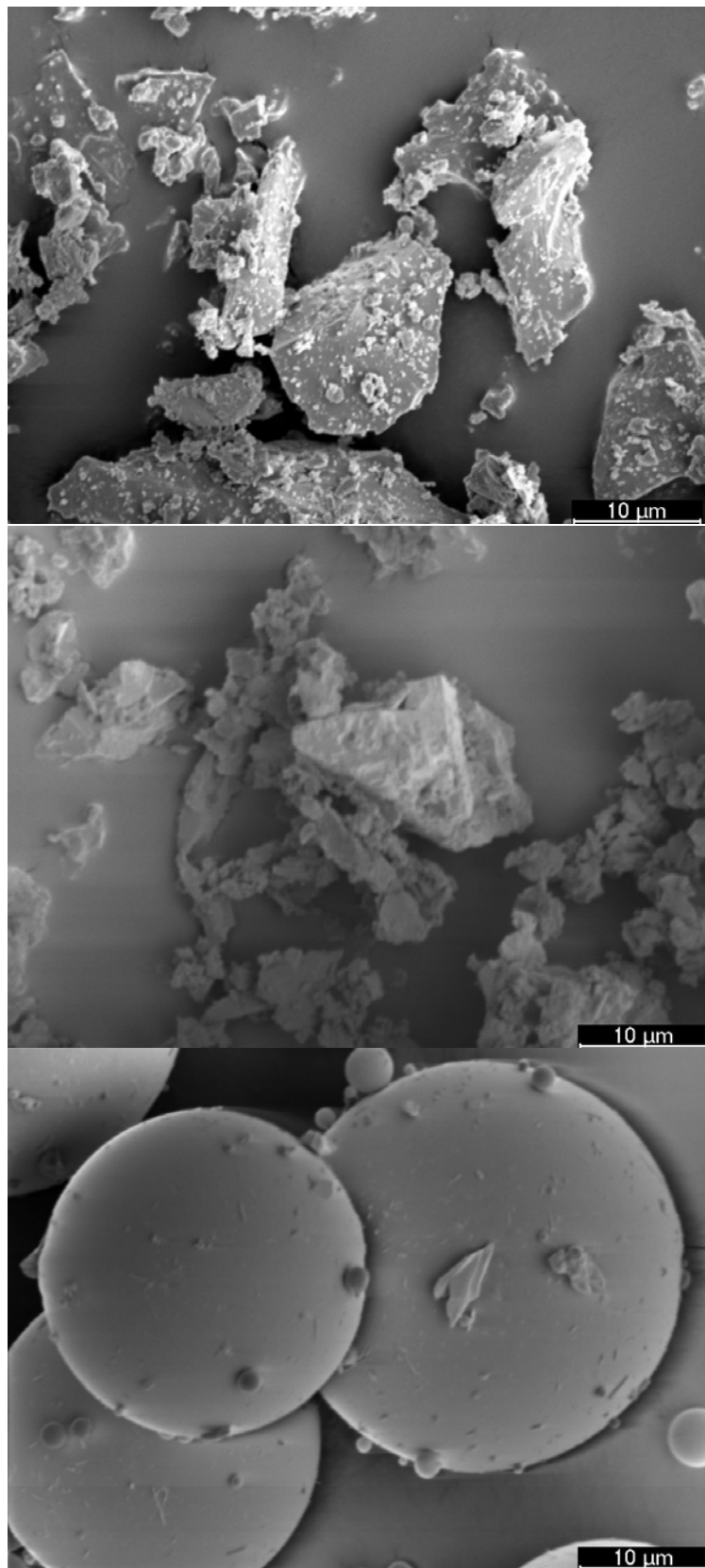


**Figure 5.2:** SEM pictures of quartz (top), limestone (center) and glass beads (bottom) at 2000x magnification

## 5.2 Flow measurement techniques in the rotating classification chamber

In this section the techniques to measure the flow in circumferential direction due to the Coriolis force will be presented. First of all the measurement of the pure liquid flow will be discussed and in the second part the determination of the movement of the fluidized bed will be explained.

### 5.2.1 Pure liquid flow in the rotating classification chamber

The measurement of the flow velocity is a standard task in industry. The simplest form to measure the velocity is the Pitot tube (John G. Webster, 1999). The basic Pitot tube simply consists of a tube pointing directly into the fluid flow and the pressure can be measured as the moving fluid is brought to rest. This pressure is the stagnation pressure of the fluid, also known as the total pressure. The measured stagnation pressure cannot of itself be used to determine the flow speed. However, since Bernoulli's equation states that

$$\text{Stagnation Pressure} = \text{Static Pressure} + \text{Dynamic Pressure}$$

the dynamic pressure is simply the difference between the static pressure and the stagnation pressure. The static pressure is generally measured using the static ports on the side of the Pitot tube. From the dynamic pressure the flow speed can be calculated. Other standard methods to determine the fluid velocity are impellers or thermal mass flow sensors. The flow velocity measured by the impeller is calculated by its rotational speed, when the fluid properties viscosity and density are known. The thermal mass flow sensor uses the dependence of the heat transfer on the fluid velocity, i.e. the higher the velocity the more heat is transferred. The heat transfer can be measured and from it the fluid velocity can be calculated.

The methods described above require wiring for power supply and data transfer, what is not a problem for standard applications in normal gravity environment. In a rotating

system wiring is not possible unless the data receiver and the power supply are rotating with the system. Installing a rotating power supply and receiver brings an unfavorable unbalance to the rotating system. Other problems are the high centrifugal acceleration forces and the high pressure gradients in the system, an environment where standard sensors are not designed and calibrated for.

For that reason it was necessary to think about a novel technique to measure the tangential flow velocity, where no wiring is required and no unbalance is brought to the rotor. The idea is to determine the velocity by a tracer, which is observed through the vision panels of the rotor.

This was done with the help of spheres which were attached to a fixing 13.5 mm above the distributor by a thread. The sphere and the thread are deflected from the radial direction by a tangential flow. With the angle of deflection the tangential velocity can be calculated by applying a force balance on the sphere. The principle of the tangential flow measurement is presented in figure 5.3. Two spheres with diameters of  $d_{ts1} = 9.9 \text{ mm}$  (volume  $V_{ts1} = 0.5 \text{ cm}^3$ ) and of  $d_{ts2} = 4.5 \text{ mm}$  (volume  $V_{ts2} = 0.06 \text{ cm}^3$ ), respectively, were used. The sphere materials were plastics with the densities  $\rho_{ts1} = 920 \text{ kg/m}^3$  for the larger sphere and  $\rho_{ts2} = 1200 \text{ kg/m}^3$  for the small sphere. Thus the first sphere was buoying towards the center while the second was sinking in the direction of the distributor. The latter one was used to determine the tangential velocities in the distributor region. The length of the thread was varied to be able to measure the fluid's tangential velocity at different locations in the chamber. For the determination of the angle of deflection from the radial direction, photographs were taken with the high speed video camera and graphically analyzed. Figure 5.4 shows these photographs for cases of the water filled classification chamber with no water throughput (left) and in the presence of a water current (right). The sphere on the right is significantly deflected by a tangential flow.

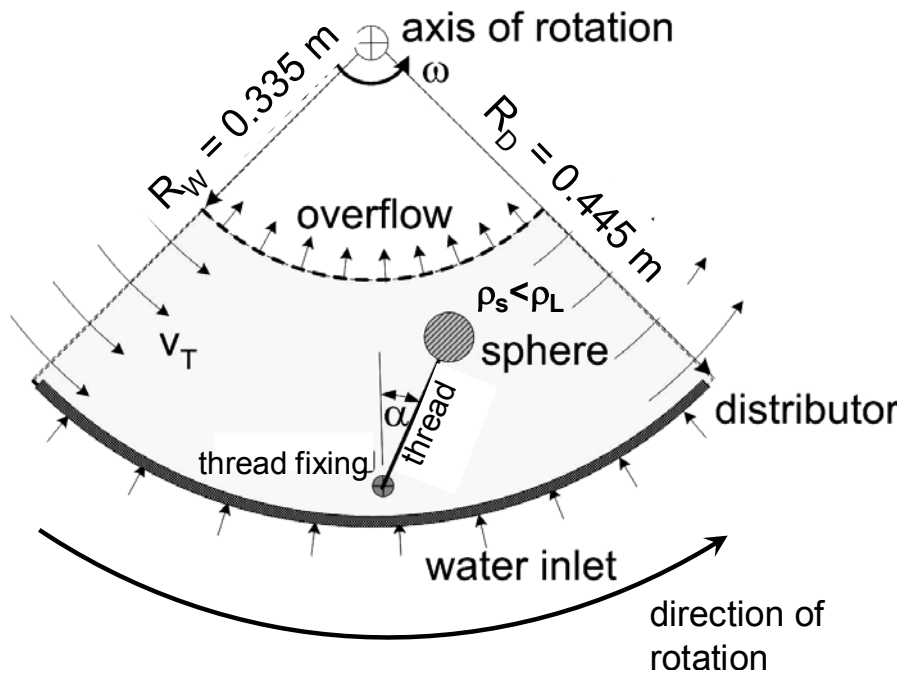


**Figure 5.3:** Principle of tangential flow measurement by the deflection of a buoying tracer sphere

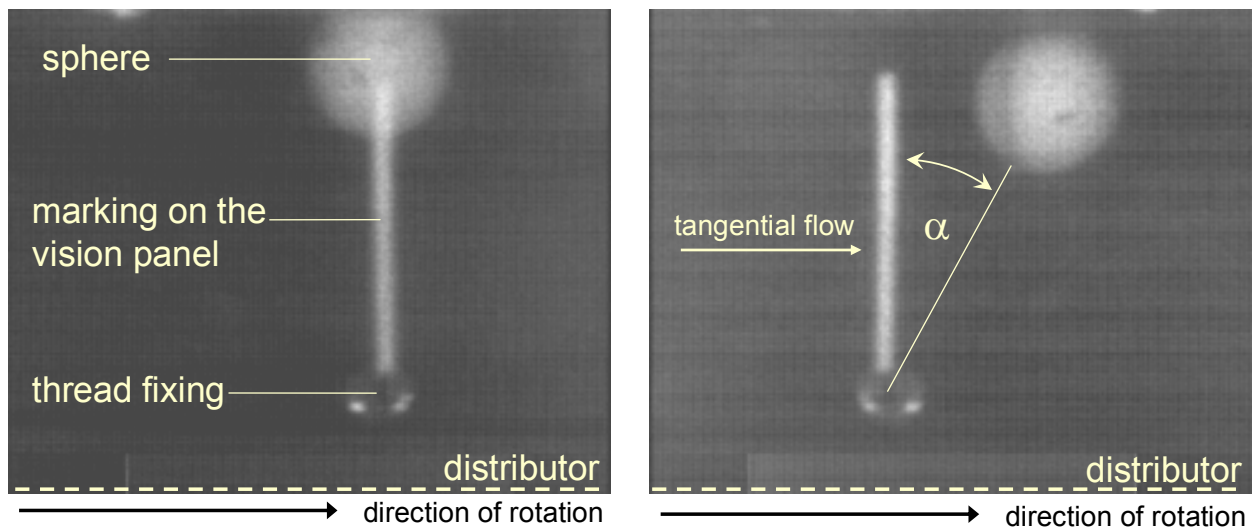


**Figure 5.4:** Sphere in water-filled classification chamber at 400 rpm  
left: water flow shut down; right: deflected sphere at a water throughput of 1200 l/h

To calculate the relative tangential velocity  $v_T$  from the deflection angle  $\alpha$ , it is necessary to apply a force balance (figure 5.5) on the sphere in radial and tangential directions:

$$F_B + F_{DR} = F_C + F_S \cdot \sin \delta \quad (5.1);$$

$$F_{DT} = F_S \cdot \cos \delta \quad (5.2);$$

where  $F_B$  is the buoyancy force,  $F_C$  the centrifugal force,  $F_{DT}$  the tangential drag,  $F_{DR}$  the radial drag and  $F_S$  the force on the thread. For the forces it holds

$$F_B = V_{ts} \cdot \rho_L \cdot r_{ts} \cdot \omega^2 \quad (5.3)$$

$$F_C = m_{ts} \cdot r_{ts} \cdot \omega^2 \quad (5.4)$$

$$F_{DR} = \frac{1}{2} \cdot c_D \cdot \frac{\pi}{4} \cdot d_{ts}^2 \cdot \rho_L \cdot \left( \frac{\dot{V}}{A_C} \right)^2 \quad (5.5)$$

$$F_{DT} = \frac{1}{2} \cdot c_D \cdot \frac{\pi}{4} \cdot d_{ts}^2 \cdot \rho_L \cdot v_T^2 \quad (5.6)$$

where  $\dot{V}$  is the total volume flow and  $A_C$  the cross sectional area in the classification chamber.

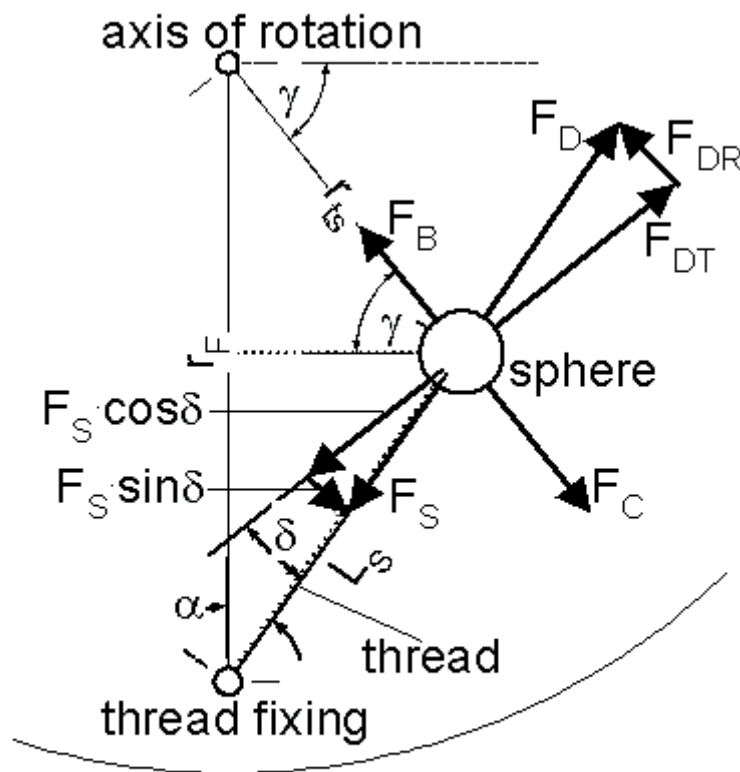


**Figure 5.5:** Force balance on the tracer sphere buoying in the direction of the weir

For a fully turbulent flow ( $Re_{ts} > 2300$ ) the drag coefficient  $c_D$  is set to 0.44. The experimental results showed that this condition was always fulfilled. The angle  $\delta$  can be calculated from the deflection angle  $\alpha$  and the angle  $\gamma$  (c.f. figure 5.5):

$$\delta = \gamma - \alpha \quad (5.7)$$

$$\gamma = \arctan [(r_F - L_S \cdot \cos \alpha) / (L_S \cdot \sin \alpha)] \quad (5.8)$$

$$r_{ts} = (r_F^2 + L_S^2 - 2 \cdot r_F \cdot L_S \cdot \cos \alpha)^{0.5} \quad (5.9)$$

where  $r_F$  is the distance from the center of the classifier to the thread fixing and  $L_S$  the length of the thread.

Combining the equations (5.1) and (5.2) results in

$$F_{DT} = \frac{F_B + F_{DR} - F_C}{\tan \delta} \quad (5.10)$$

which leads to

$$v_T = \sqrt{5.78 \cdot \left| \frac{F_B + F_{DR} - F_C}{d_{ts}^2 \cdot \rho_L \cdot \tan \delta} \right|} \quad (5.11)$$

The force balance on figure 5.5, which leads to equation (5.11), was performed for a buoying sphere with a density smaller than the fluid density. In the case of a sinking sphere, i.e. the sphere's density is higher than the one of the fluid, the angle  $\delta$  would become negative. Since the absolute value of  $\delta$  is used in (5.11) the equation is also valid for this case.

### 5.2.2 Flow of the fluidized bed in the rotating classification chamber

For the design of the coarse discharge, especially to answer the question how many feed ports and coarse discharges are necessary for the performance of the classifier, the study of the tangential movement of the bed is of major interest. The method for

the determination of the pure liquid is not applicable for the fluidized bed, because the apparent local viscosities are unknown, so that the drag forces are not calculable. However, although models exist to estimate the apparent viscosity (Tsuchiya et. al., 1997), a determination of the circumferential bed movement is not possible, because the precision of these models for this purpose is not sufficient.

Here a freely floating submerged tracer body (figure 5.6) in the fluidized bed was used and its time of circulation was recorded. On top of the submerged tracer body a small flag was fixed as an indicator. This indicator in the freeboard can be observed and allows to determine the position of the sphere in the fluidized bed. The indicator was a small and very thin flag, so that the influence of the liquid flow in the freeboard on the tracer was small. A sphere with a diameter  $d_{ts3} = 12\text{mm}$  was used and the flag was located 15 mm above the sphere's center. The weight of the tracer

was adjusted by adding some iron to achieve the desired weight, such that the tracer is submerged and only the indicator is visible above the surface of the bed. With the help of a stroboscope it is possible to follow the movement of the indicator. Pictures taken by the high speed camera allowed the determination of the bed height and of the position of the indicator in the freeboard. The exact position of the sphere's center can be calculated from the position of the indicator. With the time of circulation the tangential velocity of the bed can be determined.

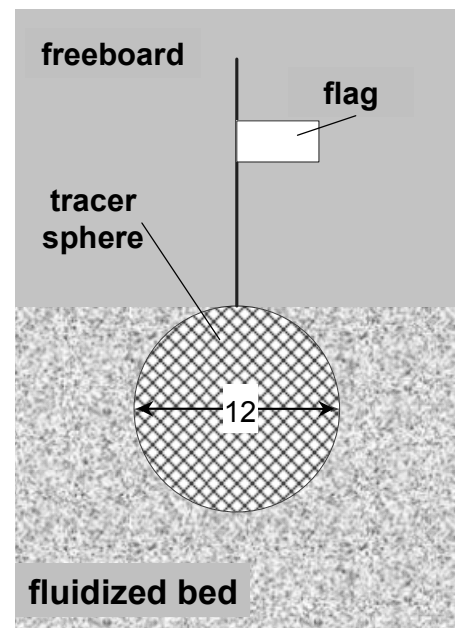


**Figure 5.6:** Floating sphere and indicator in the fluidized bed

### 5.3 Optimization of the coarse discharge

The coarse discharge plays an important role for the performance of the classifier. The operation of the needle valves with the elbow lever was found to cause severe disturbances to the classification process. For a high separation efficiency and a stable cut size a constant bed height during operation is essential. It is also important, that the coarse discharge is always submerged in the fluidized bed to avoid bypassing of fines into the coarse fraction. The four needle valves operated by an elbow lever mechanism have the drawback that the adjustment of the coarse suspension flow is not sufficiently precise. To control the bed height, the bed is observed by a stroboscope through the vision panels. As long as the bed height is below a certain level the needle valves remain closed. When the bed height becomes too high, the valves are opened. When the needle valves are open, a high volume flow leaving the classifier at the coarse discharge can be observed. The coarse discharge volume flow reduces significantly the radial flow of the classification water above the coarse discharge, i.e. the cut size changes, while the coarse discharge is open.

Experiments showed also that the opening of the 4 needle valves results in a flushing out of the bed material in a short time, such that the bed height was very fast reduced to the height of the coarse outlet. In that case fines were misclassified into the coarse fraction due to bypassing. In order to achieve a better separation performance a constant flow rate of the coarse drain and a constant bed height above the coarse discharge is necessary. The key to achieve these conditions is a modification of the coarse discharge design. For that reason a coarse discharge based on an outlet nozzle with constant aperture was introduced. The bed height in this system is self-adjusting. An increase of the bed height increases the pressure at the nozzle, which results in an increase of coarse suspension outflow, i.e. if the bed height is too high, the solid off-take is increased and vice versa. At a certain bed height, an equilibrium is



reached and the outgoing flow and the bed height remain constant. Different types of coarse discharges (figure 5.7) were tested and compared.

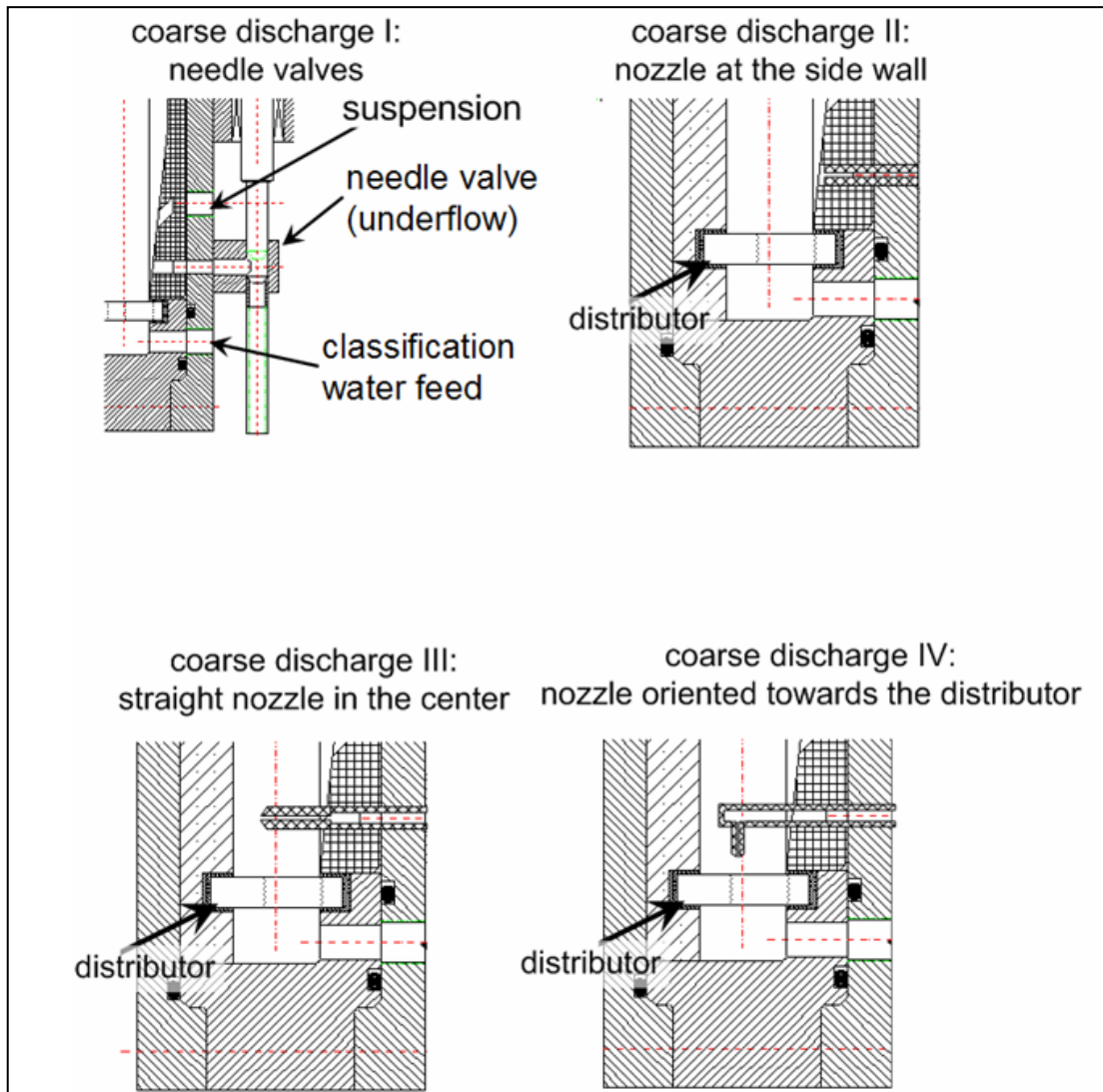


**Figure 5.7:** Types of coarse discharge mechanisms

The coarse discharge nozzle type II is a small pipe with a constant diameter of 1 mm, installed at the side of the classification chamber 13.5 mm above the distributor. The nozzle type III is quite similar to type II, but the difference is the tip of the type III nozzle is located at the centre of the fluidized bed. The tip of the discharge nozzle type IV is vertically oriented and facing the distributor at a height of 5 mm. In this case the

finer, which are supposed to be misclassified, have a longer tracking distance through the fluidized bed, so that a reduction of misclassification can be expected.

#### **5.4 The usage of the Richardson Zaki correlation for the prediction of the expansion behavior**

The intention to model the expansion behavior of the fluidized bed is the prediction of the bed porosity  $\varepsilon$  depending on the operating conditions. The knowledge of  $\varepsilon$  allows the calculation of the bed mass  $m_B$  and the bed height  $H_B$  with the help of the bed pressure drop  $\Delta p_B$ . The bed mass and the bed height are important parameters for the operation of the classifier, which have to be controlled in industrial classification processes. The control of the bed height for a given throughput can be achieved by a partial recirculation of the coarse fraction to enhance the feed mass flow in case of a too low bed height. The control of the bed height by recirculation is not part of the present work, but might be of interest for later industrial applications. For the present work the bed height is a parameter which is important to be determined for the investigation of its influence. In the classification process at high feed rates it is impossible to determine the bed surface directly due to turbidity, so that the bed pressure drop is the only usable information. To model the coarse discharge the knowledge of the bed porosity is also of importance, because the pressure drop over the discharge nozzle is depending on both, the bed height and the porosity.

In the fluidized state the bed is completely supported by the liquid, an increase of the fluidizing velocity results in an increase of the bed porosity  $\varepsilon$  at a constant bed pressure drop in the gravity field. In the centrifugal field the centrifugal acceleration changes with the radius, whereby the pressure drop decreases during expansion due to a radial shift of the mass center. Different approaches have been proposed in literature to model the expansion behavior of the bed (G. Bickert, 1997; N. Hidaka et al., 1994). One of the simplest and most handy approaches is the one by Richardson

and Zaki (J.F. Richardson, W.N. Zaki, 1954). They investigated the swarm settling of monodisperse spheres and found the following power law, which nowadays is also widely used to describe the expansion behavior of liquid fluidized beds:

$$u/u_t = \varepsilon^n, \quad (5.12)$$

where  $u$  is the swarm settling velocity and  $u_t$  denotes the terminal velocity of a single particle. If a fluidized bed is described  $u$  stands for the superficial fluidizing velocity. The Richardson Zaki exponent  $n$  is depending on the particle Reynolds number  $Re_p$ :

$$n = \begin{cases} 4,65 & 0 < Re_p \leq 0,2 \\ 4,35 \cdot Re_p^{-0,03} & 0,2 < Re_p \leq 1 \\ 4,45 \cdot Re_p^{-0,1} & 1 < Re_p \leq 500 \\ 2,39 & 500 < Re_p \end{cases} \quad (5.13)$$

where  $Re_p$  is defined by:

$$Re_p = u_t * d_p * \nu^{-1} \quad (5.14)$$

The terminal settling velocity  $u_t$  is related to the particle diameter  $d_p$  and is in the centrifugal field calculated from

$$u_t = \sqrt{\frac{4}{3} * \frac{\rho_s}{\rho_L} * \frac{d_p}{c_D} * \left(1 - \frac{\rho_L}{\rho_s}\right) * r * \omega^2} \quad (5.15)$$

In the present work the settling velocity of the mean particle diameter  $d_{p,50}$  is used to characterize the size distribution of the fluidized particles. As particle Re-numbers for the  $d_{p,50}$  exceed the validity limits for the Stokes law ( $Re > 0.25$ ) at higher angular velocities, the KASKAS drag model (Stieß, 1993):

$$c_D = \frac{24}{Re_p} + \frac{4}{\sqrt{Re_p}} + 0.4 \quad (5.16)$$

has been used for calculations of  $u_t$ . The correlation by Kaskas is valid for Reynolds numbers  $Re_p < 2 \cdot 10^5$ .

An explicit expression for the terminal velocity is not possible, because of the dependence of the drag coefficient on the terminal velocity and vice versa. The terminal velocities were therefore calculated by a MATLAB iteration and can be taken from the diagram in figure 5.8 for different operating conditions. Figure 5.9 shows the corresponding Reynolds numbers.

Although the terminal velocity  $u_t$  and the radial velocity  $u$  are depending on the radius in a rotating system, the ratio  $u/u_t$  turns out to be nearly constant due to the special shape of the classification chamber. This is illustrated in the example shown in figure 5.10. For a fluidizing throughput of  $1 \text{ m}^3/\text{h}$ , which is equivalent to  $0.005 \text{ m/s}$  fluidizing velocity, the ratio of  $u/u_t$  is plotted over the radius of the classification chamber. It can be seen that the deviations of the radius-depending ratios  $u(r)/u_t(r)$  from the ratio  $u(R_D)/u_t(R_D)$  at the distributor are very small and can therefore be neglected. In the following the term  $u/u_t$  is always related to the radius of the distributor.

To apply the Richardson Zaki model on the bed expansion behavior of the classifier the porosity  $\varepsilon$  must be determined experimentally and correlated with  $u/u_t$ . If the condition

$$d(\log u/u_t)/d(\log \varepsilon) = \text{const.} \quad (5.17)$$

is fulfilled the Richardson Zaki correlation is valid. The Richardson Zaki exponent  $n$  can then be determined by plotting  $\log(u/u_t)$  versus  $\log(\varepsilon)$ . The slope of a straight line through the plotted values is the Richardson Zaki exponent  $n$ . The porosity  $\varepsilon$  can be calculated from

$$\varepsilon = 1 - \frac{m_s}{V_B \cdot \rho_s}, \quad (5.18)$$

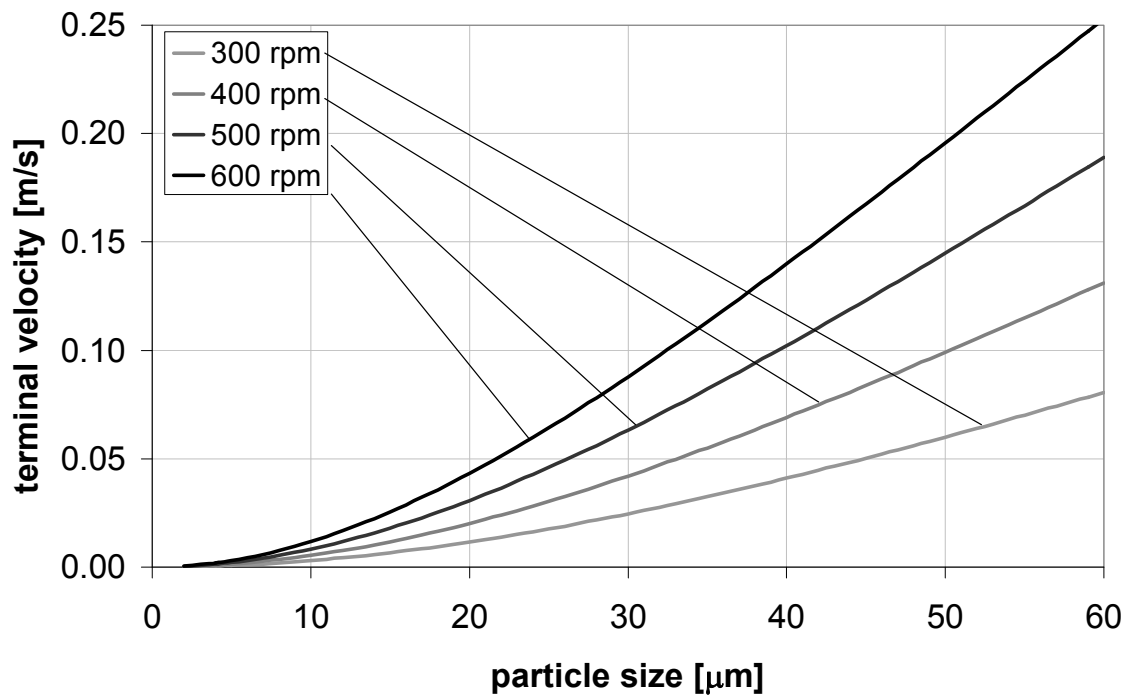


**Figure 5.8:** Terminal velocities for particles at the distributor radius ( $R_D = 0.445$  m) with a density of  $2650 \text{ kg/m}^3$  settling in the centrifugal classifier operated with water at  $10^\circ\text{C}$  ( $\eta = 1300 \text{ kg / m s}$ )

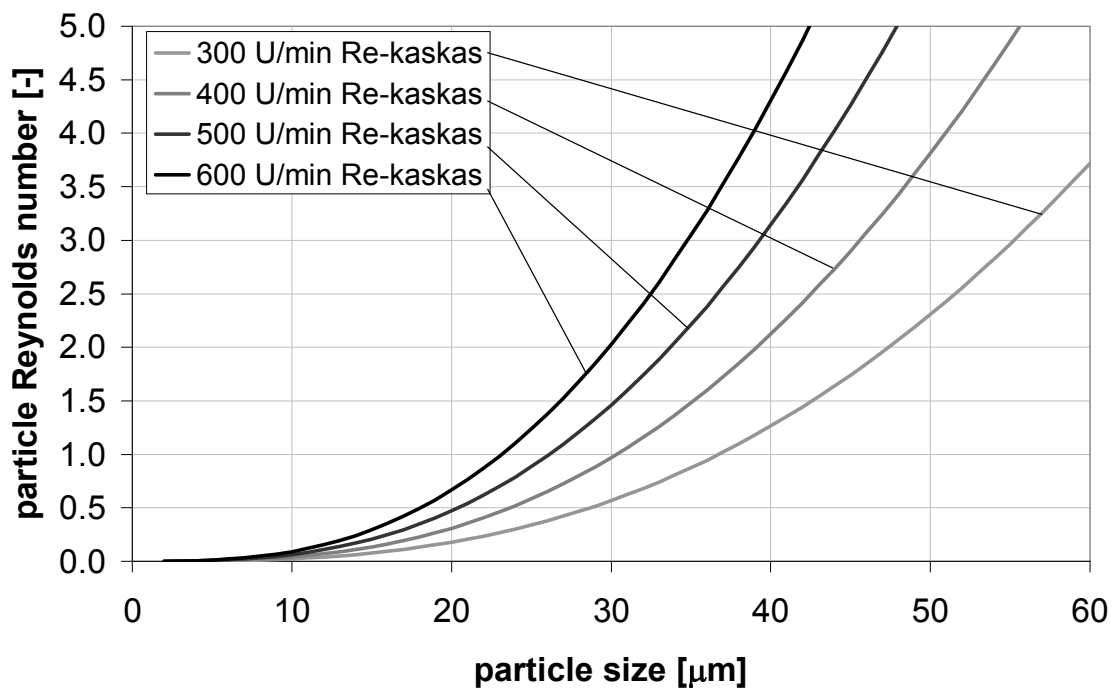


**Figure 5.9:** Reynolds numbers for particles at the distributor radius ( $R_D = 0.445$  m) with a density of  $2650 \text{ kg/m}^3$  settling in the centrifugal classifier operated with water at  $10^\circ\text{C}$  ( $\eta = 1300 \text{ kg / m s}$ )

if solids mass of the fluidized bed  $m_s$ , solids density  $\rho_s$  and bed volume  $V_B$  are known. The bed mass  $m_s$  is determined by balancing all of the incoming and outgoing flows and concentrations during the build-up of the bed. By taking pictures of the bed with the high speed camera through the observation window the bed height  $H_B$  was measured and then the bed volume  $V_B$  was calculated. It has to be mentioned that  $\varepsilon$  is the average porosity of the fluidized bed, possible porosity gradients are not considered in this work.

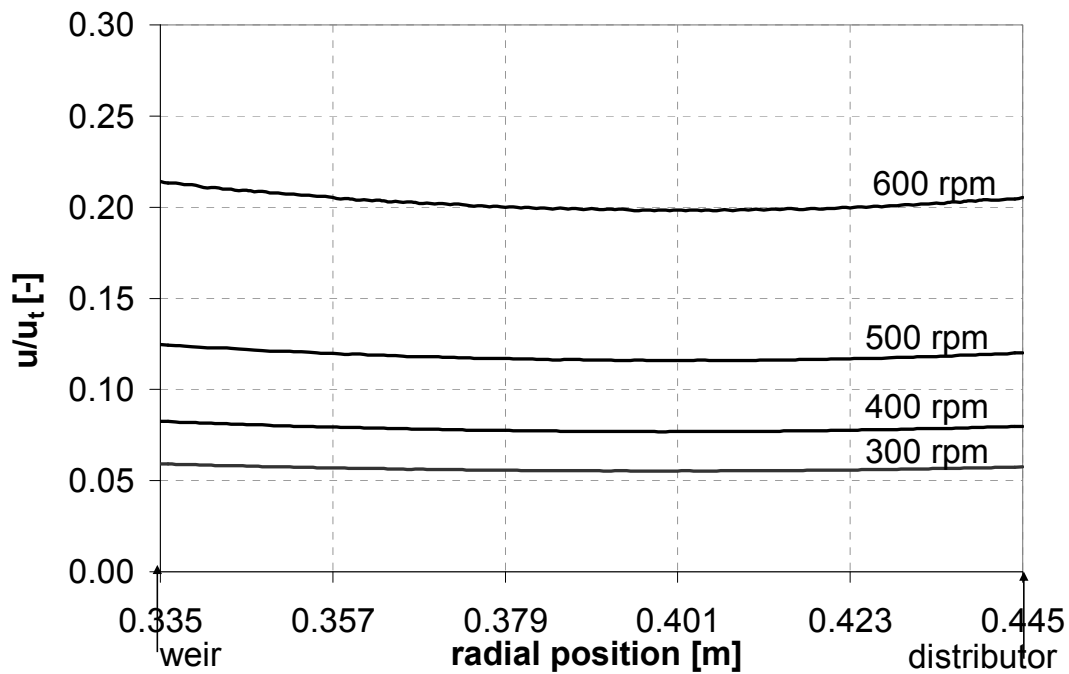


**Figure 5.10:** Fluidizing to terminal velocity ratios for a 30  $\mu\text{m}$  particle over the radius of the classification chamber for a fluidizing water throughput of  $1\text{m}^3/\text{h}$

For the comparison of different bed materials at different centrifugal accelerations, it is important to investigate fluidized beds with similar particle size distributions. Therefore the same procedure was always carried out for building up the fluidizing bed: a number of revolution of 300 rpm was adjusted with a fluidizing velocity of 0.005 m/s. Then  $0.2\text{ m}^3/\text{h}$  feed suspension with 4 vol-% solids content was introduced into the classification chamber until the desired bed height was reached. During the built up

classification took place, whereby particles smaller than the cut size were elutriated and the particle size distribution of the bed became significantly coarser than the one of the original material. As the densities of the investigated materials were almost the same (quartz sand:  $\rho_Q = 2650 \text{ kg/m}^3$ ; glass:  $\rho_G = 2500 \text{ kg/m}^3$ ; limestone:  $\rho_{Li}=2620 \text{ kg/m}^3$ ) similar particle size distributions were achieved.

### 5.5 Measurement of the bed pressure drop

The proper characterization of the hydrodynamics is an important aspect in the wet fluidization technology. The major interest in fluidized bed classification technology is the minimum superficial velocity at which the bed is stably and completely fluidized. Stability means that the bed is homogeneous and free from defluidized zones. Instabilities can be observed through the vision panel as shown in figure 5.11 on its left side. At the fluidized bed surface erupting voids are observed and the fluidized bed surface is uneven. Possible reasons are insufficient distributor pressure drop, or the existence of a wide particle size distribution, for which the radial velocity is not high enough to achieve complete fluidization. Contrary, on the right hand side of figure 5.11 no eruptions of voids are visible and the bed surface is even, so that this bed can be considered to be a stable, completely fluidized bed. The slightly concave shape of the bed surface in figure 5.11 is caused by the curvature of the classification chamber.

When the fluid velocity for a polydisperse fixed bed of a wide size distribution is increased the smaller particles are apt to slip into the voids between the larger particles and are fluidized while the larger remain stationary. This partial fluidization behavior causes the well-known smooth transition between fixed and fluidized bed pressure drop. The classifier should be operated beyond this transition regime to achieve a completely fluidized bed. On the other hand a too high fluidizing velocity via the effect of the Coriolis force causes a strong tangential flow, which will induce turbulence, what is certainly not favourable for the classification. Therefore a velocity

range has to be found, which is optimal for classification. For the purpose of finding the optimum fluidization velocity a measurement of the pressure drop characteristics in the centrifugal field is necessary.

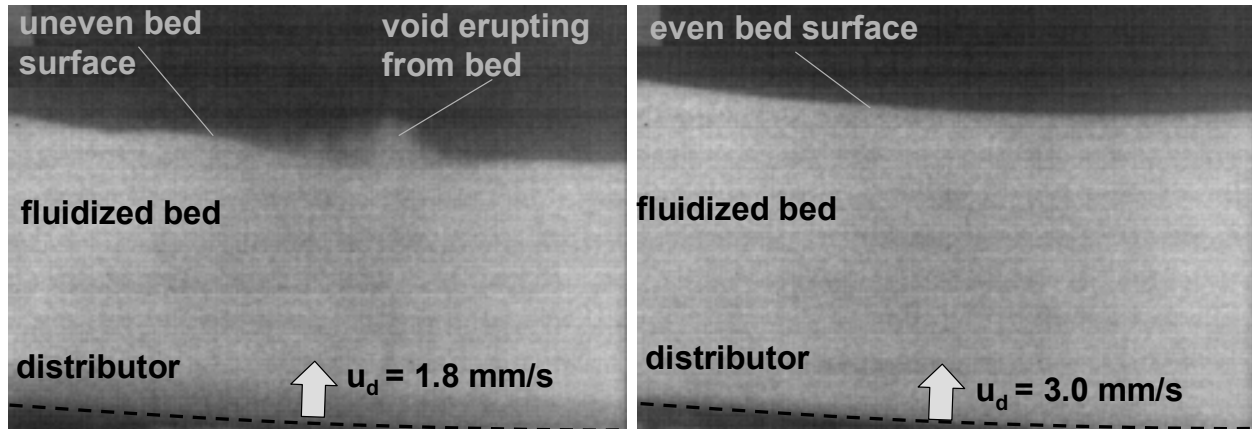


**Figure 5.11:** Fluidized bed with instabilities (left) and stable fluidized bed (right) at 400 rpm

A standard technique of pressure drop measurement in fluidization technology is the liquid column gauge. Liquid column gauges consist of a vertical column of liquid in a tube whose ends are exposed to different pressures. The column will rise or fall until its weight is in equilibrium with the pressure differential between the two ends of the tube. A very simple version is the U-tube (figure 5.12 left). One side is connected to the region of interest while the reference pressure (which might be the atmospheric pressure or a vacuum) is applied to the other. The difference in liquid level represents the applied pressure. The pressure  $p$  exerted by a column of liquid of height  $h$  and density  $\rho_L$  is given by the hydrostatic pressure equation,

$$p = h \cdot g \cdot \rho_L \quad (5.19)$$

Therefore the pressure difference between the applied pressure  $p_a$  and the reference pressure  $p_o$  in a U-tube manometer can be found by solving



$$p_a - p_o = h \cdot g \cdot \rho_L. \quad (5.20)$$

The U-tube cannot directly be used in the rotating classifier, because it cannot be assured that no water losses occur during startup and shutdown of the rotor. Therefore a modified approach is considered. A single transparent tube is installed below the distributor (figure 5.12 – right), which can be observed by the stroboscope or high speed camera during operation. In the water filled classification chamber the water column in the tube is levelled to the radial position of the weir, when no additional water is introduced. If the water flow is turned on, the distributor pressure drop  $\Delta p_D$  is indicated by the rise of the water column in the transparent tube by  $\Delta r_D$ .

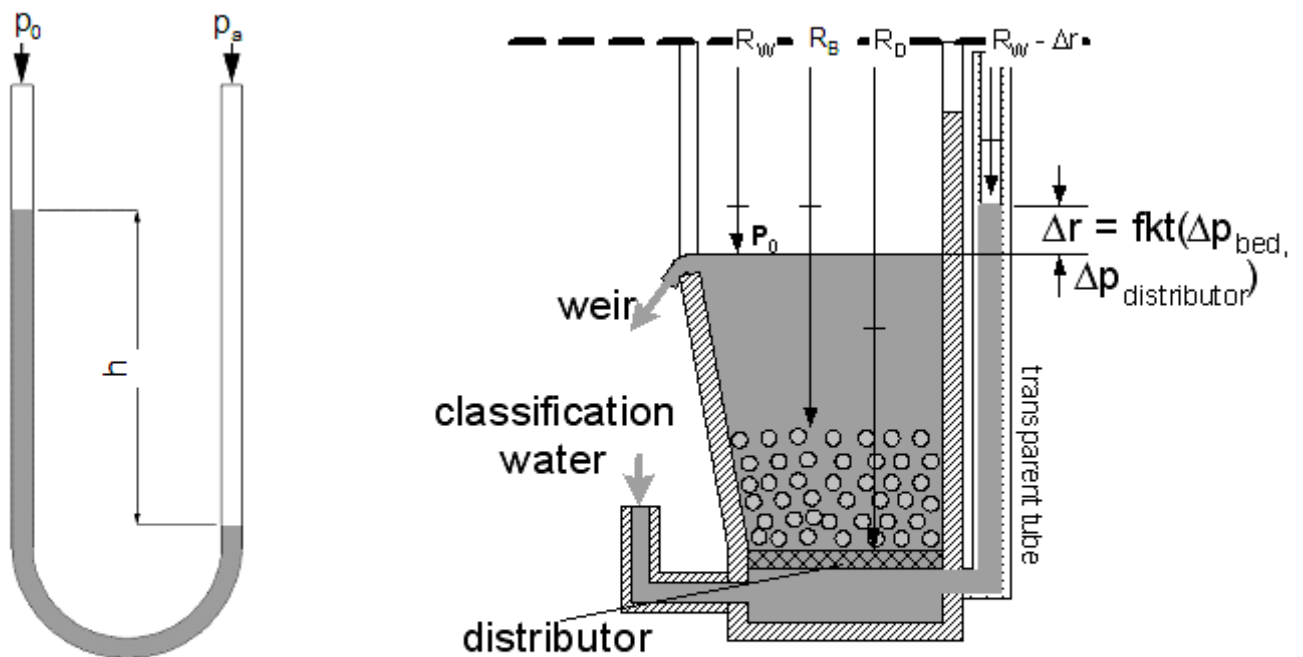


**Figure 5.12:** Pressure drop measurement by liquid column gauges.

Left: U-tube for normal gravity condition. Right: liquid column tube for rotating environment

The flow  $\dot{V}$  through the distributor with the area  $A_D$  can be treated as a laminar flow with a linear pressure drop characteristic.

$$\Delta p_D = K_D \cdot \dot{V} / A_D \quad (5.21)$$

The constant  $K_D$  can be determined by varying the volume flow  $\dot{V}$  in the solids free chamber and measuring  $\Delta p_D$  by taking photographs of the water column with the high speed camera. The principle is illustrated by the photographs in figure 5.13.

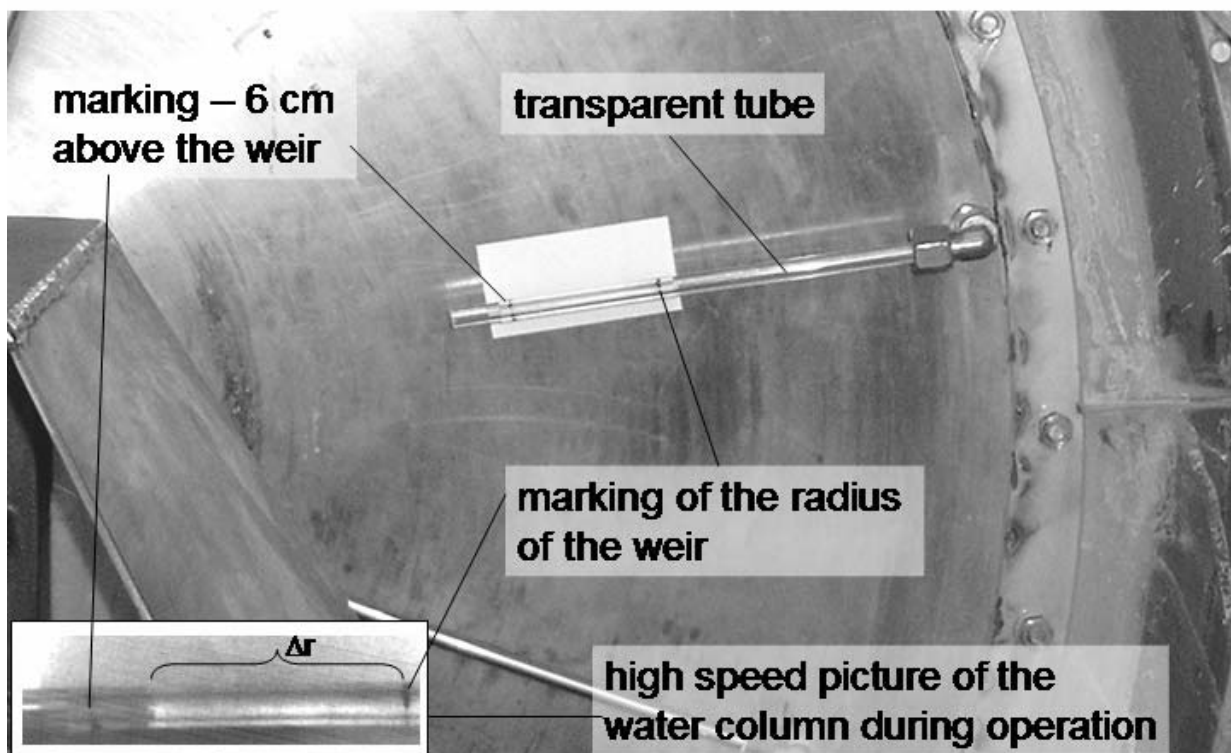


**Figure 5.13:** Photograph of the transparent tube on the classifier and highspeed picture of the water filled transparent tube during operation

### 5.6 A concept of the control of the operation of the classifier

In order to achieve a stationary operation the coarse offtake was equipped with a discharge nozzle. As has been shown above the flow through this nozzle is self-adjusting within certain limits. However, in order to avoid overloading of the apparatus it is necessary to always keep the bed level in a position between the overflow weir

and the opening of the coarse discharge nozzle. Monitoring the bed height is therefore necessary for a control of the fluidized bed classifier.

The bed height can be observed through the windows by stroboscope lighting. However, this is not possible under all operating conditions. For wide particle size distributions in the classifier feed the boundary between the bed surface and the freeboard is often difficult to distinguish. However, a measurement of the pressure drop via the liquid column gauge is comparatively easy. Unfortunately, the relationship between the bed height and the measured pressure drop is not straightforward. Therefore, in the following the pressure drop of the distributor, fixed bed and fluidized bed in the centrifugal field will be discussed in detail.

### **5.6.1 Calculation of the fluidized bed pressure drop from the liquid column gauge**

In the absence of a fluidized bed the indicated pressure drop  $\Delta p_i$  of the liquid column gauge equals the distributor pressure drop  $\Delta p_D$ .

$$\Delta p_i = \Delta p_D \quad (5.22)$$

In the presence of a fluidized bed the indicated excess height  $\Delta r$  of the water column is changed due to the additional bed pressure drop

$$\Delta p_i = \Delta p_D + \Delta p_B \quad (5.23)$$

For the calculation of the bed pressure drop the distributor pressure drop has to be subtracted from the indicated pressure drop  $\Delta p_i$ :

$$\Delta p_B = \Delta p_i - \Delta p_D \quad (5.24)$$

The pressure drop for a fluidized bed in the gravitational field is:

$$\Delta p_B = (\rho_s - \rho_L) \cdot (1 - \varepsilon) \cdot g \cdot H_B \quad (5.25)$$

where  $H_B$  denotes the fluidized bed height. For the differential bed pressure drop in the rotating fluidized bed it holds

$$dp/dr = (\rho_s - \rho_L) \cdot (1 - \varepsilon) \cdot r \cdot \omega^2 \quad (5.26)$$

from which it follows after integration

$$\Delta p_B = 0.5 \cdot (\rho_s - \rho_L) \cdot (1 - \varepsilon) \cdot \omega^2 \cdot [R_D^2 - R_B^2] \quad (5.27)$$

which relates the radius of the bed surface  $R_B$  to the bed pressure drop  $\Delta p_B$ . Conducting pressure drop measurements in the absence of a fluidized bed allows the determination of the distributor pressure drop coefficient  $K_D$ . In analogy to equations (5.26) and (5.27) it holds for the indicated pressure drop  $\Delta p_i$ :

$$\Delta p_i = 0.5 \cdot \rho_L \cdot \omega^2 \cdot [R_W^2 - (R_W - \Delta r)^2] \quad (5.28)$$

Inserting equations (5.28), (5.21) and (5.27) into (5.24) yields

$$0.5 \cdot (\rho_s - \rho_L) \cdot (1 - \varepsilon) \cdot \omega^2 \cdot [R_D^2 - R_B^2] = 0.5 \cdot \rho_L \cdot \omega^2 \cdot [R_W^2 - (R_W - \Delta r)^2] - K_D \cdot \dot{V} / A_D \quad (5.29)$$

Equation (5.29) provides a relationship between the radius of the fluidized bed surface  $R_B$  and the excess height  $\Delta r$  of the liquid column, which can now be used to calculate the bed height  $H_B$  from the indication of the liquid column gauge. The bed height is given by:

$$H_B = R_D - R_B \quad (5.30)$$

### 5.6.2 Bed pressure drop model

Knowing the bed expansion behavior of the fluidized bed, the pressure drop can be modelled when the bed mass and the operation parameters are known. The bed expansion behaviour is expressed by a Richardson-Zaki type relationship as defined by equation (5.12).

The pressure drop of the fluidized bed is

$$\Delta p_B = 0.5 \cdot (\rho_s - \rho_L) \cdot (1 - \varepsilon) \cdot (R_D^2 - R_B^2) \cdot \omega^2 \quad (5.31),$$

where  $R_D$  is radius of the distributor and  $R_B$  the radius of the bed surface.

A differential volume element  $dV$  of the bed is described by:

$$dV = 2 \cdot \pi \cdot B \cdot r \cdot dr; \quad (5.32)$$

with the chamber width

$$B = K \cdot r^{-2} \quad (5.33)$$

and the chamber profile constant  $K = 0.00396 \text{ m}^3$ . Equation 5.33 is employed under the assumption of a parabolic classification chamber profile as proposed by Schmidt. The deviation of the realized two linear profiles (cf. figure 3.5) from the parabolic one was proven (Schmidt, 2007) to be less than 2%, so that the use of (5.33) is justified.

The integration of (5.32) leads to the bed volume  $V_B$ :

$$V_B = 2 \cdot \pi \cdot K \cdot \ln(R_D/R_B) \quad (5.34)$$

With

$$V_B = m_s / [\rho_s \cdot (1 - \varepsilon)] \quad (5.35)$$

the following expression for the bed surface radius  $R_B$  can be derived:

$$R_B = R_D \cdot \exp \left[ \frac{-m_s}{2 \cdot \pi \cdot K \cdot \rho_s \cdot (1 - \varepsilon)} \right] \quad (5.36)$$

The usage of the Richardson - Zaki equation, (5.12) combined with (5.36) and (5.31) results in

$$\Delta p_B = \frac{1}{2} \cdot (\rho_s - \rho_L) \cdot \left(1 - \sqrt[n]{\frac{u}{u_t}}\right) \cdot R_D^2 \cdot \omega^2 \cdot \left(1 - \exp\left[\frac{-m_s}{\pi \cdot K \cdot \rho_s \cdot (1 - \sqrt[n]{u/u_t})}\right]\right) \quad (5.37)$$

With equation (5.37) the bed pressure drop in the fluidized state is related to the solids mass in the fluidized bed mass. If the bed pressure drop was measured, equation (5.31) combined with the Richardson Zaki equation (5.12) can be used to calculate the radius of the fluidized bed surface  $R_B$ :

$$R_B = \sqrt{R_D^2 - \frac{2 \cdot \Delta p_B}{(\rho_s - \rho_L) \cdot \left(1 - \sqrt[n]{\frac{u}{u_t}}\right) \cdot \omega^2}} \quad (5.38)$$

For the case, that the radius of the bed surface  $R_B$  is known, the solids mass of the bed can be calculated by transforming equation (5.36) in combination with (5.12) in

$$m_s = 2 \cdot \pi \cdot K \cdot \rho_s \cdot \left(1 - \sqrt[n]{\frac{u}{u_t}}\right) \cdot \ln \frac{R_D}{R_B} \quad (5.39)$$

As shown in chapter 5.4 the ratio of  $u/u_t$  is approximately constant over the whole radius of the classification chamber, so that

$$\frac{u}{u_t} = \frac{u_D}{u_t(R_D)} \quad (5.40)$$

is valid, where  $u_t(R_D)$  denotes the terminal particle velocity at the location  $r = R_D$ .  $u_t(R_D)$  is related to the Sauter diameter  $d_{ps}$  of the coarse fraction, which was determined from samples, which were analyzed by laser diffraction analysis.

### 5.6.3 Pressure drop model for rotating fixed beds

For a given rotational speed the classification water throughput is limited at the lower end by the minimum fluidizing velocity  $u_{mf}$ . Below  $u_{mf}$  the bed is in the fixed bed state and thus no classification is possible. The estimation of  $u_{mf}$  in advance is therefore essential for the selection of the operation parameters such as the angular speed of the rotor and the classifying water throughput. The minimum fluidizing velocity  $u_{mf}$  can be determined by the intersection of the fixed bed and the fluidized pressure drop profile.

For the description of the fixed bed pressure drop it holds for the presently considered fine particle system (Stieß, 1993):

$$\frac{dp}{dr} = C_K \cdot \frac{(1 - \varepsilon_{FB})^2}{\varepsilon_{FB}^3} \cdot S_V^2 \cdot \eta \cdot u, \quad (5.41)$$

Equation 5.41 is the Carman and Kozeny equation in its differential form.  $S_V$  is the specific surface of the particles,  $C_K$  is the Kozeny coefficient and  $\varepsilon_{FB}$  denotes the fixed bed porosity. The Carman-Kozeny equation is valid for pure laminar flow for  $Re_p < 3$  (Stieß, 1993). For glass beads in water the particle Reynolds number  $Re_p = 3$  is reached at 600 rpm for a Sauter diameter of 35  $\mu\text{m}$ . The Sauter diameters of the particle beds in the present work were always below that value, so that the Carman-Kozeny equation can be assumed to be valid. The relationship between the specific surface  $S_V$  and the Sauter diameter for spheres is:

$$S_V = 6 / d_{ps} \quad (5.42)$$

In equation (5.41) the dependence of the flow velocity  $u$  on the radius  $r$  due to the chamber profile has to be taken into account. It holds

$$u = \frac{u_D}{R_D} \cdot r \quad (5.43)$$

It follows

$$\frac{dp}{dr} = C_K \cdot \frac{(1 - \varepsilon_{FB})^2}{\varepsilon_{FB}^3} \cdot S_V^2 \cdot \eta \cdot \frac{u_D \cdot r}{R_D} \quad (5.44)$$

and after integration

$$\Delta p_{FB} = 0.5 \cdot S_V^2 \cdot C_K \cdot \frac{(1 - \varepsilon_{FB})^2}{\varepsilon_{FB}^3} \cdot \eta \cdot u_D \cdot \frac{R_D^2 - R_{FB}^2}{R_D} \quad (5.45)$$

Equation (5.45) describes the pressure drop of the flow through the rotating fixed bed. For the Kozeny constant a value of  $C_K = 4$  was used as proposed in literature (Stieß, 1993). The radial position of the fixed bed surface  $R_{FB}$  can be calculated with equation (5.36), when the fixed bed porosity  $\varepsilon_{FB}$  and the solids mass of the bed  $m_S$  are known.

The minimum fluidizing velocity can now be determined from the intersection of the fixed bed pressure drop  $\Delta p_{FB}(u_D)$  with the fluidized bed pressure drop  $\Delta p_B$  from equation (5.37) for  $\varepsilon = \varepsilon_{FB}$ . The fixed bed porosities were experimentally determined for various conditions and can be found in chapter 6.

#### 5.6.4 Determination of the operational parameters

In this chapter the operational parameters according to the separation task are discussed. A separation task is normally defined by the solids feed mass flow  $\dot{M}_S$  and the desired cut size  $d_C$ . The resulting solids flow  $\dot{M}_C$  of the coarse fraction through the discharge nozzle is then given by:

$$\dot{M}_C = \dot{M}_S \cdot (1 - Q_3(d_C)) \quad (5.46)$$



The key parameters for designing the classification process in the present case with regard to the cut size  $d_C$  and solids throughput are the bed height, the angular velocity  $\omega$  and the coarse suspension mass flow  $\dot{M}_{\text{SUS,C}}$ . The coarse suspension mass flow  $\dot{M}_{\text{SUS,C}}$  is defined as the sum of the solids mass flow  $\dot{M}_C$  and the water mass flow  $C$  through the coarse discharge nozzle. The bed height can be chosen according to the findings discussed in chapter 6. An adequate angular velocity has to be selected corresponding to the cut size. Schmidt (2004) found that a higher angular speed of the rotor results in a higher classification sharpness, so choosing a high angular speed is recommendable for the achievement of a high classification performance. On the other hand more water is consumed due to a higher demand of classification water throughput and the cut size is deviating more from the theoretical one in direction to larger particle sizes (Schmidt, 2004). Rotational speeds between 400 and 800 rpm are recommended for cut sizes between 3 and 20  $\mu\text{m}$  for a particle density of 2650  $\text{kg/m}^3$  in water.

For a specified classification task the coarse suspension mass flow through the discharge nozzle  $\dot{M}_{\text{SUS,C}}$  is the parameter, which has to be adapted. This can be obtained by selecting an appropriate discharge nozzle with the required orifice diameter, which determines the throughflow. Therefore a model was developed to calculate the flow  $\dot{M}_{\text{SUS,C}}$  through the nozzle depending on the radius of the bed surface  $R_B$ , on the angular velocity  $\omega$  and on the nozzle diameter  $d_N$ . In this model a nozzle friction coefficient  $\xi$  was introduced, which was determined for the nozzles of the present work by the experiments presented in chapter 6.

In the present work, where discharge nozzles, each with an orifice diameter of 1mm, were used, the suspension mass flow through the nozzle is specified by the orifice diameter for the operating point to be investigated. Therefore the model can be used to estimate the permissible suspension feed flow corresponding to the operating

parameters and the nozzle orifice. Furthermore the model can be employed to compare the measured coarse discharge with the theoretical one to detect bypasses from the freeboard directly to the coarse recovery. In that case the bypass is indicated, when the measured coarse discharge flow is significantly below the theoretical one.

The hydrostatic pressure increase  $dp$  over a ring element  $dr$  is defined as:

$$dp = [\varepsilon \cdot \rho_L + (1 - \varepsilon) \cdot \rho_S] \cdot r \cdot \omega^2 \cdot dr, \quad (5.47)$$

With the mean fluidized bed density  $\rho_m$ :

$$\rho_m = \varepsilon \cdot \rho_L + (1 - \varepsilon) \cdot \rho_S \quad (5.48)$$

it follows:

$$dp = \rho_m \cdot r \cdot \omega^2 \cdot dr \quad (5.49)$$

The pressure drop of the nozzle  $\Delta p_N$  is defined as the difference of the hydrostatic pressure at the radial position of the nozzle inside the chamber and the ambient pressure. The nozzle pressure drop  $\Delta p_N$  can be calculated by integration of equation (5.49) in the radial intervals of freeboard and fluidized bed:

$$\Delta p_N = 0.5 \cdot \rho_m \cdot (R_N^2 - R_B^2) \omega^2 + 0.5 \cdot \rho_L \cdot (R_B^2 - R_W^2) \cdot \omega^2 \quad (5.50)$$

$R_N$ ,  $R_W$  and  $R_B$ , are the radial positions of the coarse discharge, the weir and the fluidized bed surface, respectively.

The pressure drop of a nozzle is defined (Bohl, 1991) for a single phase flow:

$$\Delta p_N = 0.5 \cdot \rho_L \cdot \xi \cdot v_N^2 \quad (5.51)$$

with  $v_N$  being the fluid velocity in the nozzle and  $\xi$  denoting the nozzle pressure drop coefficient. For a liquid-solid suspension with  $d_p \ll d_N$  a similar relationship to hold

$$\Delta p_N = 0.5 \cdot \rho_m \cdot \xi \cdot v_N^2 \quad (5.52)$$

is assumed, where  $\rho_L$  is replaced by the mean density  $\rho_m$ . The suspension velocity in the nozzle (diameter  $d_N$ ) can be expressed by the suspension massflow  $\dot{M}_{\text{sus,C}}$  through the nozzle:

$$\dot{M}_{\text{sus,C}} = \frac{\pi}{4} \cdot d_N^2 \cdot v_N \cdot \rho_m \quad (5.53)$$

or with regard to  $v_N$ :

$$v_N = \frac{4 \cdot \dot{M}_{\text{sus,C}}}{\pi \cdot d_N^2 \cdot \rho_m} \quad (5.54)$$

Equating equations (5.52) and (5.50) and inserting (5.54) gives the suspension mass flow through the nozzle:

$$\dot{M}_{\text{sus,C}} = \sqrt{\rho_m \frac{\rho_m \cdot (R_N^2 - R_B^2) + \rho_L \cdot (R_B^2 - R_W^2)}{\xi}} \cdot \frac{\pi}{4} \cdot d_N^2 \cdot \omega \quad (5.55)$$

The coarse mass flow is then

$$\dot{M}_C = \dot{M}_{\text{sus,C}} \cdot (1 - \varepsilon) \cdot \frac{\rho_s}{\rho_m} \quad (5.56)$$

The porosity  $\varepsilon$  can be obtained from the Richardson – Zaki correlation after rearranging it to the porosity  $\varepsilon$ :

$$\varepsilon = \sqrt[n]{\frac{u}{u_t}} \quad (5.57)$$

The experimentally determined values of the Richardson Zaki coefficient  $n$  are presented in chapter 6.

For the Richardson Zaki correlation the required fluidizing velocity  $u$  and the average particle settling velocity of the fluidized bed  $u_t$  have to be estimated. The fluidizing

velocity  $u$  is correlated to the single particle settling velocity of the cut size  $d_c$  at the distributor:

$$u = \frac{R_D \cdot (\rho_s - \rho_L) \cdot \omega^2 \cdot d_c^2}{18 \cdot \eta}, \quad (5.58)$$

which is valid in the Stokes range. The average particle diameter  $d_{p,50}$  of the fluidized bed can be obtained from the particle size distribution of the suspension feed under the assumption of an ideal classification at the cut size  $d_c$ . The corresponding terminal velocity  $u_t$  can then be taken from figure 5.8. By solving equation (5.55) with regard to  $d_N$ , a suitable nozzle diameter can be selected for the given classification task.

This model describes the outflow through the coarse discharge orifice under completely turbulent conditions, i.e. the influence of the apparent suspension viscosity is neglected. Furthermore a likely slip between liquid and particles is neglected. Therefore the present model can only provide a rough estimation for choosing the operating conditions. The pressure drop coefficient of the nozzle is determined experimentally and can be found in chapter 6. Schmidt (2004) reported that the real cut sizes are on average overestimated in the range of a few microns. However this approach can be used for choosing appropriate operating parameters.

To verify the feasibility of the classification task under the desired operating conditions, the minimum fluidizing velocity of the bed material, i.e. the coarse fraction, has to be estimated by equating the pressure drop models for the rotating fixed bed (equation 5.45) and fluidizing bed (equation 5.37), respectively. The particle size distribution of the coarse fraction is given when an ideal classification at the cut size  $d_c$  is assumed. When the chosen fluidizing velocity  $u_D$  is larger than the calculated minimum fluidizing velocity the feasibility of the classification at that angular velocity is proven. In the final chapter 6.10 a practical example of the above control strategy is provided.

### 5.7 Evaluation of classification experiments

In this chapter the determination of the solid and the fluid mass flows is presented. For that reason mass balances of the fluid and the solid phase were set up and the unknown mass flows were solved. With the knowledge of the mass flows, the separation efficiency curve  $T(d_p)$  can be calculated, which characterizes the performance of classifications. Different options are available to define the separation efficiency curve, these options are also discussed in this chapter.

As described in chapter 3.1 the volume flows of the classification water and the feed suspension are measured by magnetic flowmeters.  $S$  is the water mass flow in the feed suspension with the mass load  $x_S$ .  $W$  is the mass flow of fluidizing water.  $S$  and  $W$  can be calculated from the indicated volume flows  $\dot{V}_S$  and  $\dot{V}_W$ . The indicated volume flow  $\dot{V}_S$  can be expressed by the sum of solid and fluid flow:

$$\dot{V}_S = \frac{S}{\rho_L} + \frac{\dot{M}_S}{\rho_S} = \frac{S}{\rho_L} + \frac{S \cdot x_S}{\rho_S} \quad (5.59)$$

Solving equation (5.59) with regard to  $S$  gives:

$$S = \dot{V}_S \cdot \rho_L \left[ 1 + x_S \cdot \frac{\rho_L}{\rho_S} \right]^{-1} \quad (5.60)$$

The mass flow of the fluidizing water is obtained from:

$$W = \dot{V}_W \cdot \rho_L \quad (5.61)$$

The solid feed loading  $x_S$  as well as  $x_F$  and  $x_C$  (solids loading of fines and coarse flow) are determined by sampling and weighing before and after evaporating the water fraction.

The water mass flows of the coarse' and fines fraction (C and F) are determined by balancing the water and the solids mass flows:

$$\text{Water mass balance: } \frac{dm_L}{dt} = -\frac{dm_S}{dt} \cdot \frac{\rho_L}{\rho_S} = S + W - F - C \quad (5.62),$$

where  $m_L$  and  $m_S$  are the water and solids mass in the classification chamber, respectively. Bed and water mass in the classification chamber are linked due to the displacement of water when bed mass is added.

$$\text{Solids mass balance: } \frac{dm_S}{dt} = S \cdot x_S - F \cdot x_F - C \cdot x_C \quad (5.63)$$

The change of the solids mass in the bed  $dm_S/dt$  can be determined by evaluating the bed pressure drop during the build-up of the bed. When a constant bed height is achieved it holds  $dm_S/dt = 0$ . This is the case for the classification experiments, where the sampling is started when the desired bed height is reached.

Combining the solid mass balance (5.63) with the water mass balance (5.62), the water mass flows of the fines and coarse, F and C, can be obtained:

$$\text{Fines: } F = \frac{\frac{dm_S}{dt} \cdot \left( \frac{\rho_L}{\rho_S} \cdot x_C + 1 \right) + W \cdot x_C - S \cdot (x_S - x_C)}{x_C - x_F} \quad (5.64)$$

$$\text{Coarse: } C = \frac{\frac{dm_S}{dt} \cdot \left( \frac{\rho_L}{\rho_S} \cdot x_F + 1 \right) + W \cdot x_F - S \cdot (x_S - x_F)}{x_F - x_C} \quad (5.65)$$

The mass fractions of coarse and fines are:

$$c = \frac{C \cdot x_C}{F \cdot x_F + C \cdot x_C} \quad (5.66)$$

$$f = \frac{F \cdot x_F}{F \cdot x_F + C \cdot x_C} \quad (5.67),$$

where  $c$  and  $f$  are the ratios of solid mass recovered in the coarse and fines fractions to the solids mass in the feed. At a constant bed height, i.e.  $dm_S/dt = 0$ , the coarse and fines fraction can directly be calculated from the measured mass flows and solids contents.

$$c = \frac{[W \cdot x_F - S \cdot (x_S - x_F)] \cdot x_C}{[W \cdot x_F - S \cdot (x_S - x_F)] \cdot x_C - [W \cdot x_C - S \cdot (x_S - x_C)] \cdot x_F} \quad (5.68)$$

$$f = 1 - c \quad (5.69)$$

The performance of the classification is characterized by the separation efficiency curve  $T(d_p)$ . The separation efficiency is defined for a size class between  $d_p$  and  $(d_p + dd_p)$  as the ratio of the mass recovered in the coarse fraction to the mass initially present in the feed. The separation efficiency can be calculated from different measurements, because the dependence

$$q_S(d_p) = c \cdot q_C(d_p) + f \cdot q_F(d_p) \quad (5.70)$$

allows different expressions for the definition of the separation efficiency curve, which are presented below:

$$T(d_p) = \frac{c \cdot q_C(d_p)}{c \cdot q_C(d_p) + f \cdot q_F(d_p)} \quad (5.71)$$

$$T(d_p) = \frac{c \cdot q_C(d_p)}{q_S(d_p)} \quad (5.72)$$

$$T(d_p) = 1 - \frac{f \cdot q_F(d_p)}{q_S(d_p)} \quad (5.73)$$

In the first case (equation 5.71), the separation efficiency curve is determined by measuring the mass fraction of coarse' and fines (c and f) and their density distributions  $q_C(d_p)$  and  $q_F(d_p)$ , respectively. The initially present particles of the feed are expressed by the sum of particle masses recovered in the coarse and fines fractions.

In the second case (equation 5.72) the mass fraction of the coarse recovery c and their density distribution  $q_C(d_p)$  was measured and correlated with the density distribution of the feed  $q_S(d_p)$ .

In the third case (equation 5.73) the mass fraction of the fines recovery f and their density distribution  $q_F(d_p)$  was measured and correlated with the density distribution of the feed  $q_S(d_p)$ .

Theoretically all three definitions should result into the same separation efficiency curve. However errors occur in the measurement of the particle size distributions. This results in a distortion of the separation efficiency curve, which can be expressed by an error particle mass flow  $E(d_{p,i})$ :

$$E(d_{p,i}) = S \cdot x_S \cdot [Q_{3,S}(d_{p,i+1}) - Q_{3,S}(d_{p,i})] - C \cdot x_C \cdot [Q_{3,C}(d_{p,i+1}) - Q_{3,C}(d_{p,i})] - F \cdot x_F \cdot [Q_{3,F}(d_{p,i+1}) - Q_{3,F}(d_{p,i})] \quad (5.74)$$

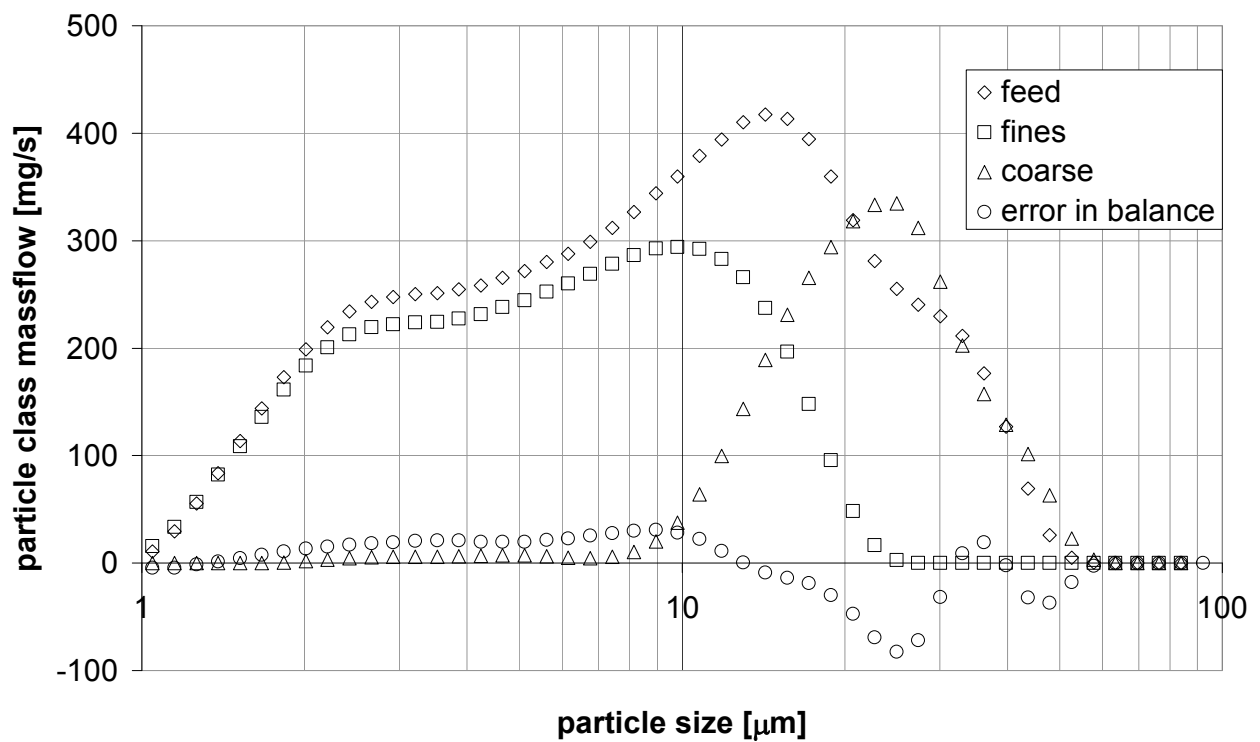
If  $E(d_{p,i}) \neq 0$ , the mass balances of the interval  $(d_{p,i+1} - d_{p,i})$  are not fulfilled due to errors in measurement or due to particle breakage and attrition. Even if a small amount of particles are affected, especially for particle classes at the lower or higher



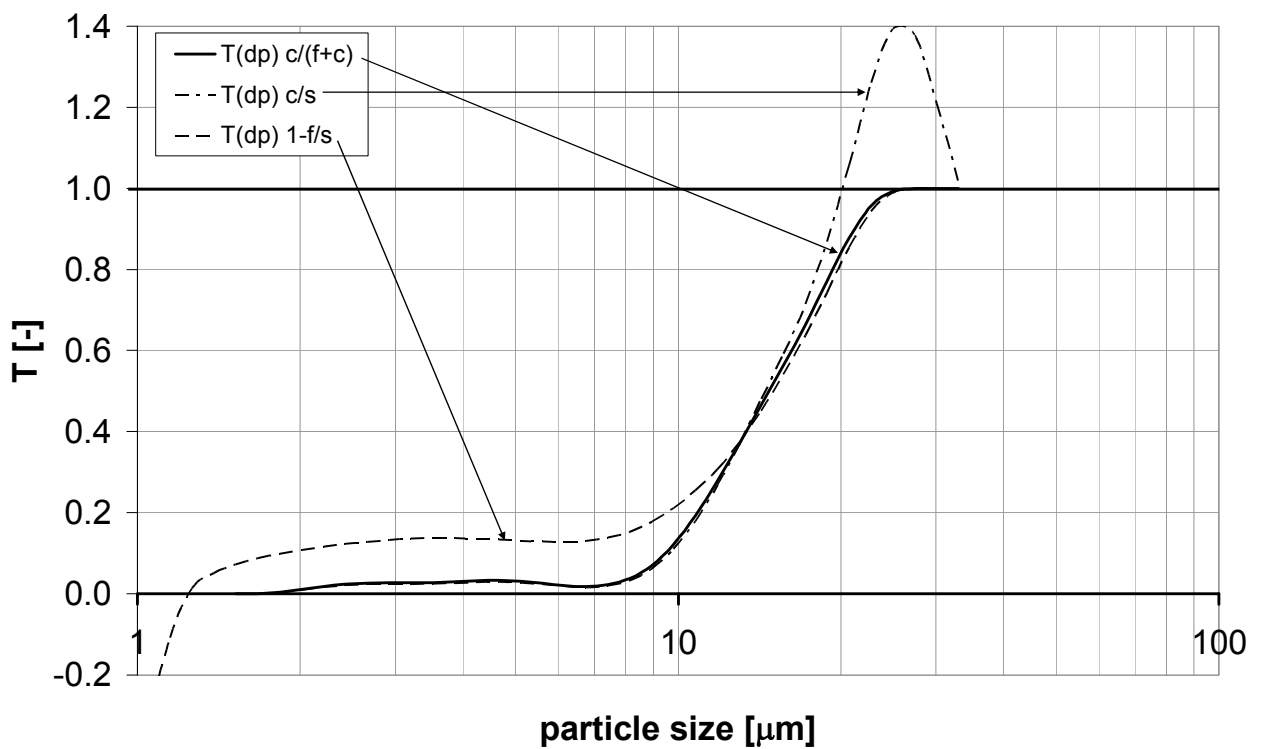
boundaries, the separation efficiency curve can be changed significantly. A definition has to be chosen which is most robust to disturbances caused by errors and particle comminution.

Figure 5.14 shows the mass flows of each particle class for feed, coarse and fines as well as the balance error “mass flow” of the classification experiment from 24<sup>th</sup> of April 2008 as an example. In general the mass flow error is quite small, but has a high contribution in the classes at the lower and higher end. It should be discussed how this error is affecting the separation efficiency curves depending on their definition.

Therefore the separation efficiency curves of the classification experiments from 24<sup>th</sup> of April 2008 are compared in figure 5.15. The definition of equation (5.73) shows a huge error in the separation efficiency curve in the lower micron range, because the curve exceeds the limits of validity by becoming negative. The separation efficiency curve defined by equation (5.72) exceeds the limits of validity in the coarse range by becoming large than one. These errors originate from the sources discussed above. The separation efficiency curves using these definitions are very sensitive to errors in the particle class balances. When using the definition of equation (5.71), however, the separation efficiency curve stays in the limits between zero and one. The latter definition shows a very robust behavior concerning errors in the particle class mass balances. Hence this definition is used for the calculation of the separation efficiency curves in this work.



**Figure 5.14:** Mass flows of the particle classes and error mass flow (classification 24<sup>th</sup> April 2008)



**Figure 5.15:** Separation efficiency curves with different definitions (classification 24<sup>th</sup> April 2008)

Besides the separation efficiency curve the sharpness defined by Eder (Stieß, 1993) is a common definition for the characterization of the classification performance. The sharpness  $\kappa$  is defined as the ratio of the particle sizes  $d_{p,25}$  and  $d_{p,75}$ , where the separation efficiency curves reaches 25% and 75% respectively:

$$\kappa = d_{p,25} / d_{p,75} \quad (5.75)$$

Rumpf (Stieß, 1993) characterizes analytical sharp separations in the range between  $0.9 < \kappa < 0.8$ , technically sharp separations between  $0.8 < \kappa < 0.6$  and usual technical separations between  $0.3 < \kappa < 0.6$ . The drawback of that definition is the fact, that fishhook effects and local minima are not considered. For a more detailed characterization the separation efficiency curve has to be considered.

## 6 Results and discussion

### 6.1 Fluid mechanics of the flow in the classification chamber

#### 6.1.1 Results of the simplified model

The pure liquid flow in the classification chamber is calculated as described in chapter 4. The reason of the investigation is the generation of a tangential flow by the Coriolis force, which turned out to have a strong influence on the flow pattern. For a rough estimation a simplified model was used. In this model the observer is located outside the system, so the absolute velocities are considered.

Equating the conservation of angular momentum with the wall friction results in a tangential velocity profile. The profile is calculated with MATLAB iterating the equations (4.16) to (4.18) over the chamber profile with a step width of  $\Delta r = 0.0001$  m. Calculations of the tangential velocity of the pure fluid have been done with the simplified model with radial velocities at the distributor of 5.0 and 6.5 mm/s and rotational speeds of 300, 400 and 600 rpm, respectively. The fluidization velocities were chosen to be significantly higher than the minimum fluidization velocities in order to allow a stable operation of the fluidized bed during the experiments, which were carried out with the same velocities.

To check the influence of density and viscosity on the fluid mechanics, additional calculations with air as fluid have been carried out with the same velocities and rotational speeds. The wall friction coefficients are depending on the turbulence and the Reynolds number of the flow, respectively. For Reynolds numbers  $Re > 2300$  the wall friction coefficient  $\lambda$  was set to 0.055, for  $Re < 1000$  it was set to

$$\lambda = 96/Re \quad (6.1)$$

(Schröder, 2004). For the calculations with water it turned out, that the flow was for all simulated operating conditions fully turbulent. The Reynolds number was calculated by

$$Re = \frac{d_{hc} \cdot v}{\nu} \quad (6.2)$$

with

$$v = \sqrt{v_R^2 + v_T^2}, \quad (6.3)$$

where  $d_{hc}$  is the hydraulic diameter of the classification chamber. The Reynolds number varied in the calculations from 9500 to 13800 for water. For air the Reynolds numbers were much lower with  $400 < Re < 841$ . Thus equation (6.1) was used to calculate the wall friction coefficient.

Figure 6.1 shows calculated profiles of the absolute tangential water and the wall velocities for the rotational speeds of 300, 400 and 600 rpm over the chamber height at a radial injection velocity of 0.005 m/s. At the distributor the tangential velocities of the wall and the fluid are the same. Due to the conservation of momentum the tangential movement of the fluid is increased as the fluid moves inward (negative radial direction). With increasing velocity difference between fluid and wall, the wall friction is also increased resulting in a peak of the absolute tangential fluid velocity closely above the distributor. After the peak the absolute tangential velocities are following the wall velocities (dashed in figure 6.1) with a slight increase of the velocity difference. The relative tangential velocity profile results from subtracting the wall velocity from absolute tangential fluid velocity. Figure 6.2 shows the relative tangential velocity profiles at a classification water velocity of 0.005 m/s for the rotational speeds of 300, 400 and 600 rpm, respectively. In the distributor region the velocity is increased with a high slope at the beginning until the influence of the wall friction becomes significant. This happens between 0.01 and 0.02 m above the distributor, whereby the increase of the tangential velocity profile is reduced. At the overflow weir

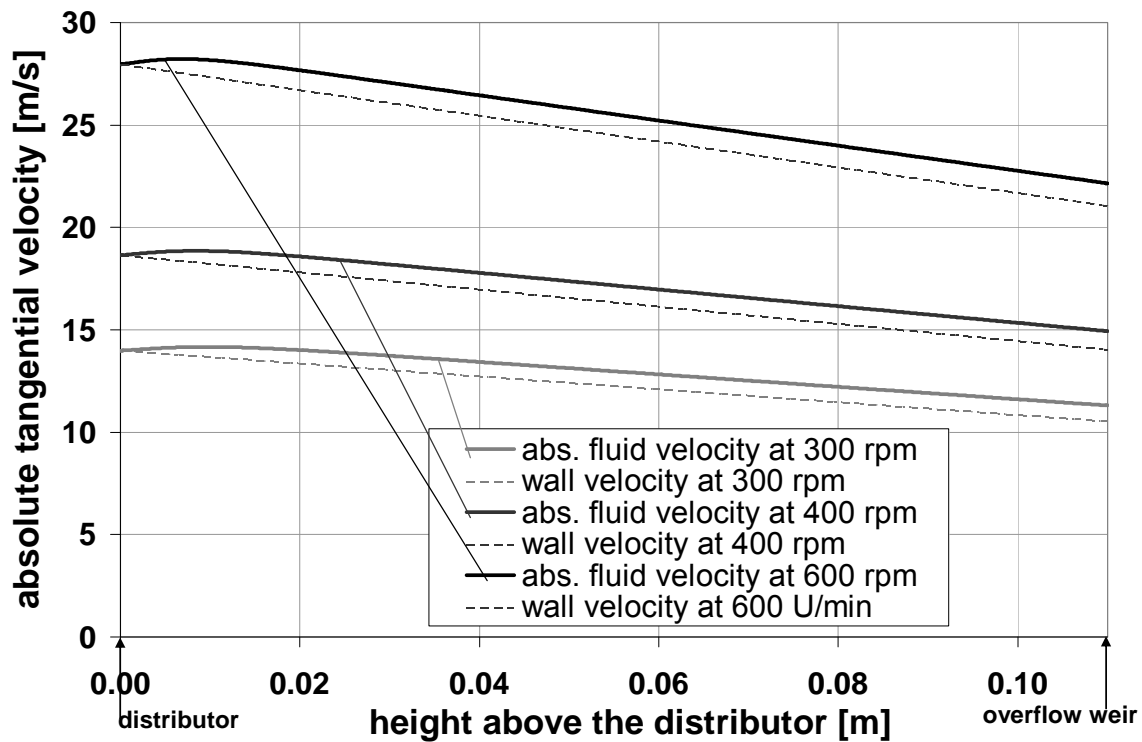


**Figure 6.1:** Absolute tangential velocities calculated with the simplified model for different rotational speeds and a constant fluidizing velocity of 5 mm/s at the distributor

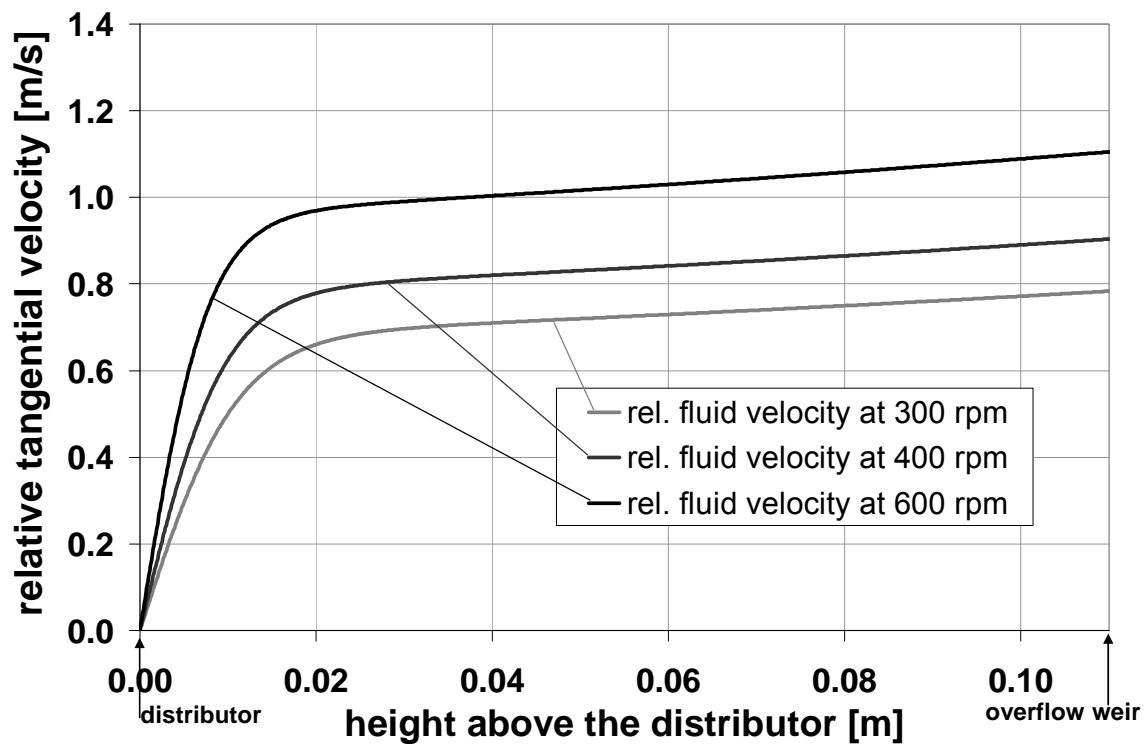


**Figure 6.2:** Relative tangential velocity profiles calculated from the simplified model at different rotational speeds at a constant fluidizing velocity of 5 mm/s at the distributor

at 0.11 m above the distributor relative tangential velocities of about 0.8 m/s (300 rpm), 0.9 m/s (400 rpm) and 1.1 m/s (600 rpm) were reached. The tangential velocity profile was also calculated for water and air with a radial flow velocity of  $u_D = 0.0065$  m/s at the distributor. The result is pictured in figure 6.3. The transition of the water velocity profile from a steep to a slight slope is much smoother than in the case of  $u_D = 0.005$  m/s. Also the tangential velocities of 0.85 m/s and 0.35 m/s for 300 rpm and 600 rpm at the overflow weir are much higher than in the case of 0.005 m/s.

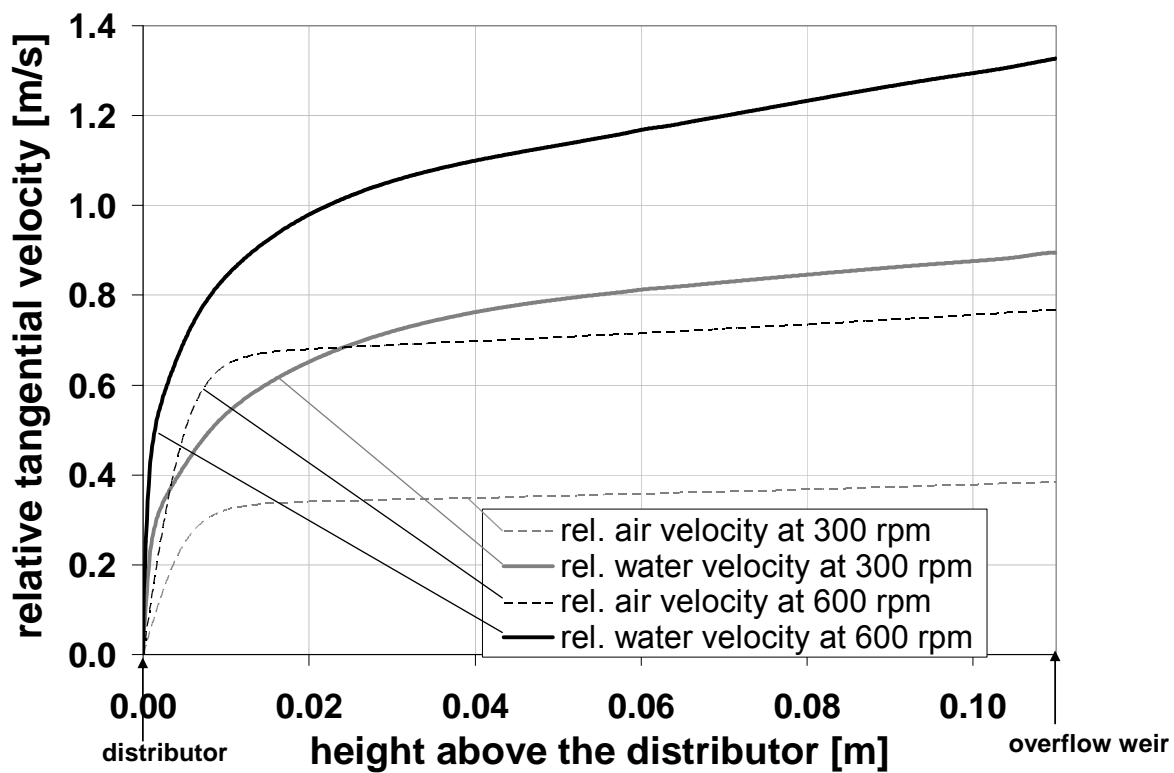


**Figure 6.3:** Profiles of the relative tangential velocities calculated from the simplified model for water and air at a constant fluidizing velocity of 6.5 mm/s at the distributor

It can be seen from the calculation result that for both fluids the tangential velocity component is two orders of magnitude higher than the radial one. Another result is the increase of the tangential velocity with increasing rotational speed and also with increasing radial velocities. For air the tangential velocity is much lower compared to water for the same operating conditions. The reason is the change of the ratio of the

inertial force and the frictional forces due to the lower density and higher viscosity of the gas.

### 6.1.2 Results of the CFD simulation

A more complicated but also more precise way to predict the flow pattern is the CFD simulation. The advantage of the CFD simulation is that a 3 dimensional flow pattern is provided and that all forces acting on the fluid are considered. High computing power and long calculation times are required for an accurate calculation. A CFD calculation can be applied to confirm the findings of the simplified model and to give a deeper insight into the behavior of the flow. A vertical profile of the flow for a classification velocity of  $u_D = 0.005$  m/s at a rotational speed of 300 rpm in the water-filled and solids-free classification chamber calculated by the CFD-Simulation is shown in figure 6.4 a. The velocity vectors on a cut line through the chamber are mainly oriented in tangential direction, the vertical component of the velocities can hardly be detected. In figure 6.4 b it can be seen that the tangential velocity in the case of air is much lower compared to water under the same conditions, although the Coriolis acceleration

$$\vec{a}_c = -2\vec{\omega} \times \vec{u} \quad (6.4)$$

is independent of density and viscosity. As explained before, the effect of friction, which is much higher for air, causes the lower tangential velocities. The tangential flow pattern itself can not directly be assessed as a negative effect on the classification performance as long as the radial velocity component is undisturbed. However, it can be expected that turbulence is induced in the freeboard influencing the radial velocity profile. This influence may result in blurring the separation efficiency curve  $T(d_p)$ , which does not occur in the normal gravity field.



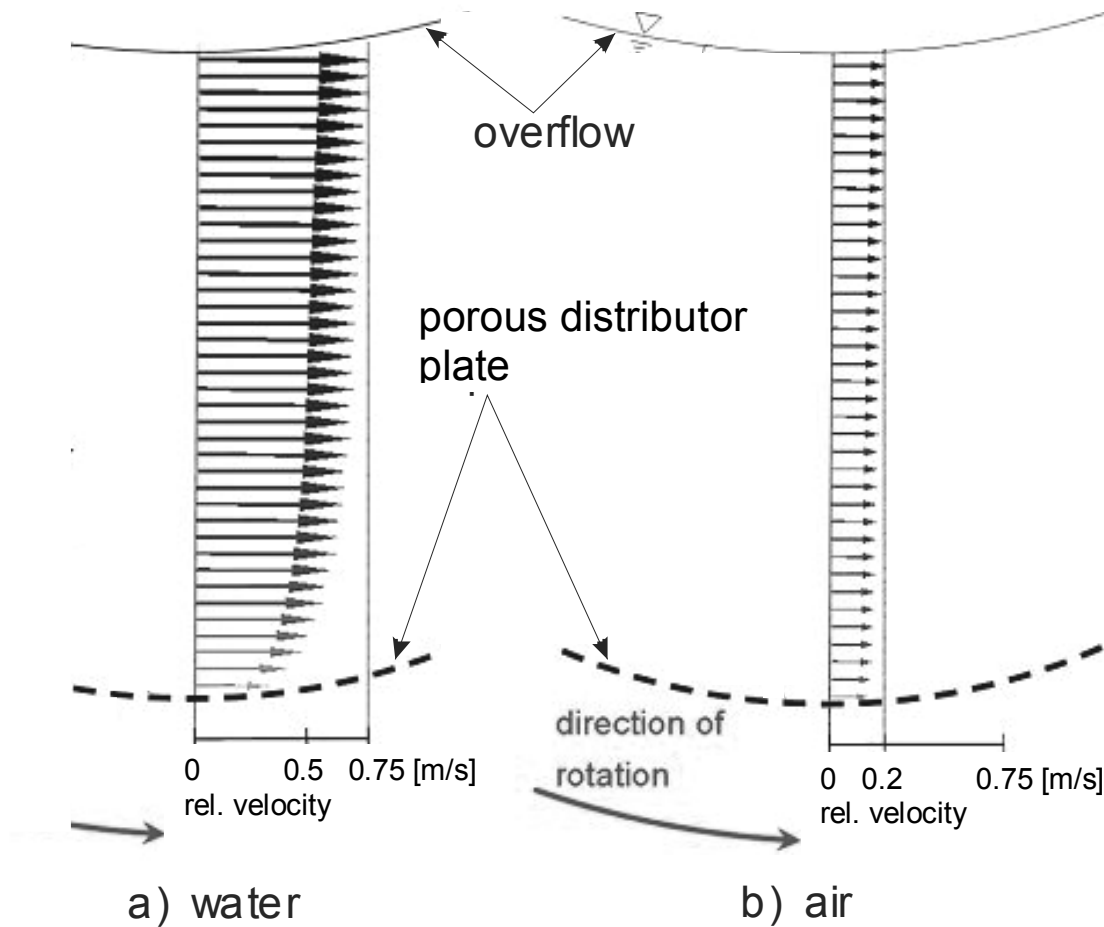


**Figure 6.4:** CFD-simulation of the pure fluid flow: (a) with water and (b) with air (rotational speed: 300 rpm, radial velocity at distributor: 5.0 mm/s)

One could imagine that a segmentation of the classification chamber could suppress the Coriolis-induced tangential flow. Therefore this case was investigated, too. Figure 6.5 shows the flow pattern on a cut surface of the classification chamber for a completely closed classification chamber at the same conditions as for the circumferential system (300 rpm;  $u_D = 0.005$  m/s). In this configuration much lower tangential velocities occur than in the circumferential chamber. The velocity vectors are not oriented radially, as it is desired for high separation efficiencies. On the contrary, vortices are found caused by the presence of the Coriolis force, with vortex velocities of one magnitude higher than the fluidizing velocity. It can be expected that the occurrence of vortices decreases the classification performance significantly, because vortices are affecting directly the radial velocity component, which is decisive

for classification. It can be expected that large particles are lifted inside vortices, whereas very fine particles are transported downwards. Therefore coarse and fines can be misclassified due to vortices. Such a configuration (which has been used by Timmermann, 1998) is therefore not recommended for classification purposes.

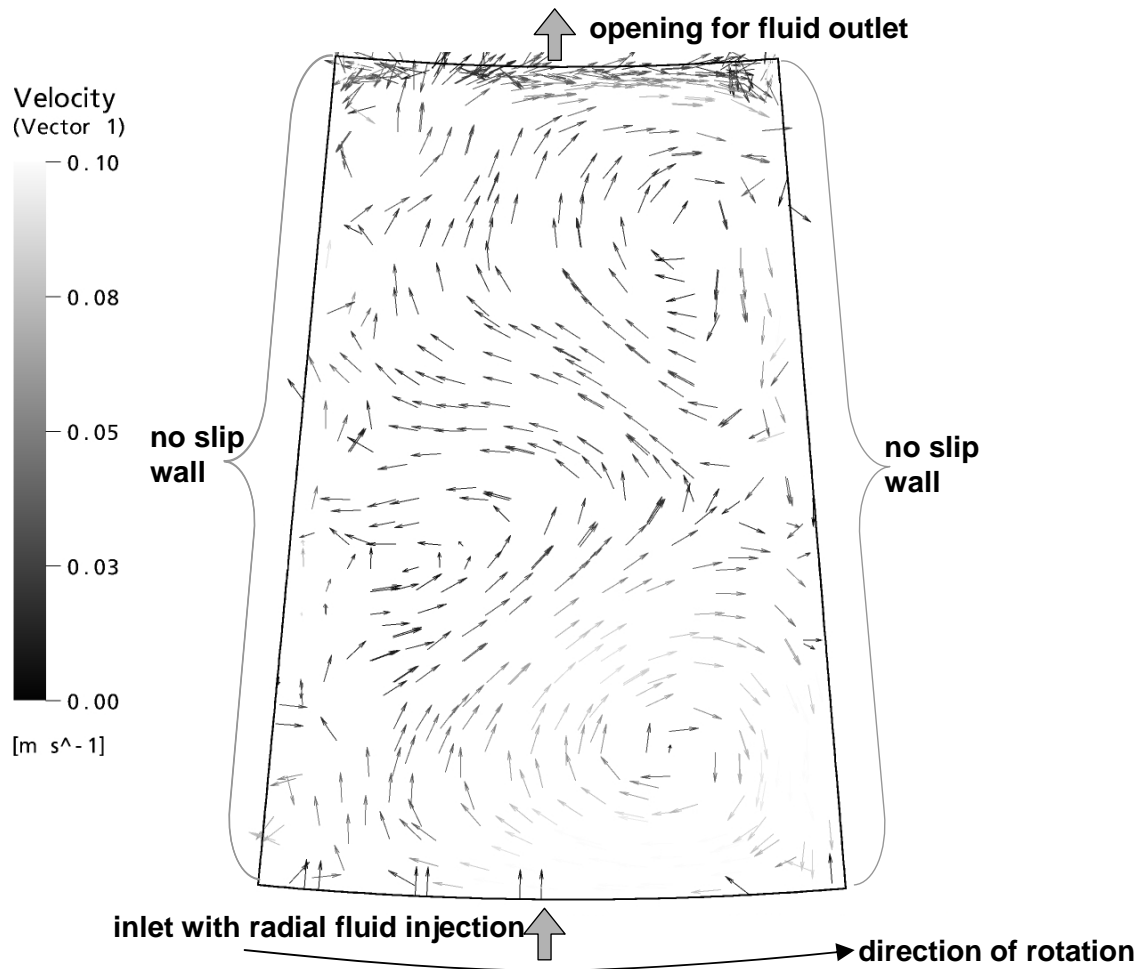


**Figure 6.5:** CFD-simulation of the pure water flow in a closed chamber (rotational speed: 300 rpm, radial velocity at distributor: 5.0 mm/s)

### **6.1.3 Comparison of the results of the simplified model with CFD calculations and experiments conducted with a tracer sphere**

To verify the theoretical results of the circumferential velocity profile, the tangential velocities have been determined experimentally by the method described in section 5.2. The figures 6.6 and 6.7 show comparisons between calculation and measurements. Water flows of 1.0 and 1.3 m<sup>3</sup>/h, respectively, corresponding to the radial classification velocities of 5.0 and 6.5 mm/s were used.

It can be seen that the results of the CFD-simulation, the simplified model and the experimental data are in good agreement. This provides evidence that both, the CFD-simulation and the simplified model give reasonable results.

However in the distributor region some of the experimental results show larger values than the calculated ones. An explanation lies in the fact, that for these measurements the thread to the deflecting sphere is very short, which results in a reduced accuracy for the velocity measurements. Also inhomogeneities in the flow through the distributor may have an effect on the flow in the distributor region; such inhomogeneities will dissipate with increasing distance to the distributor.

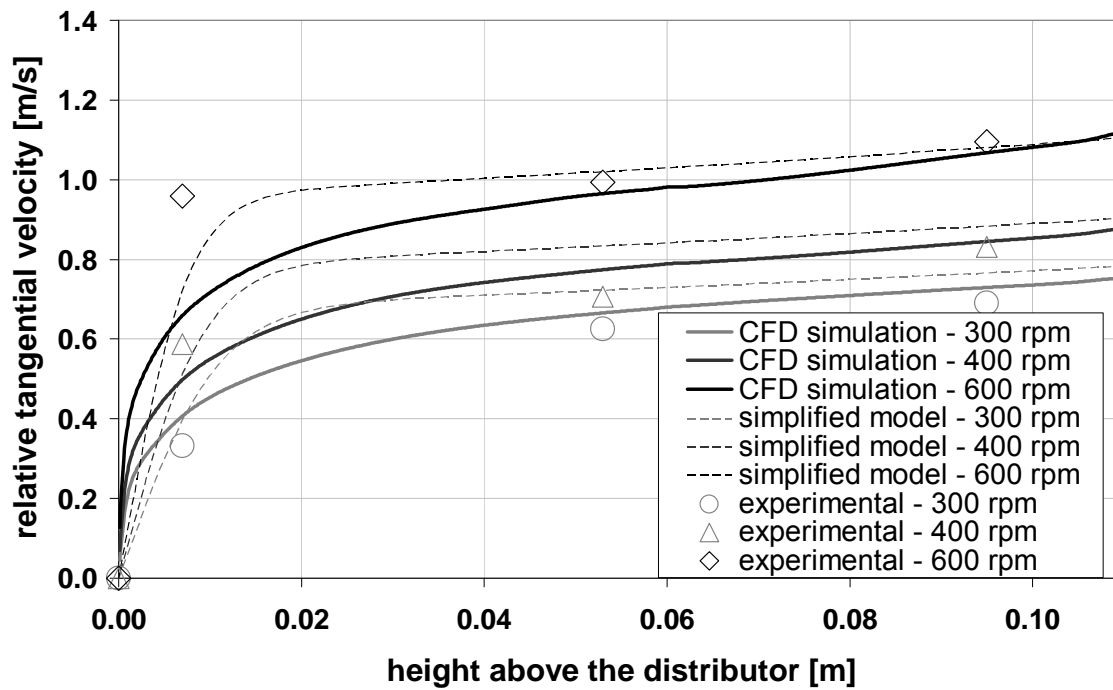


**Figure 6.6:** Comparison of the calculated tangential velocities (radial distributor velocity of 5.0 mm/s) with experiments

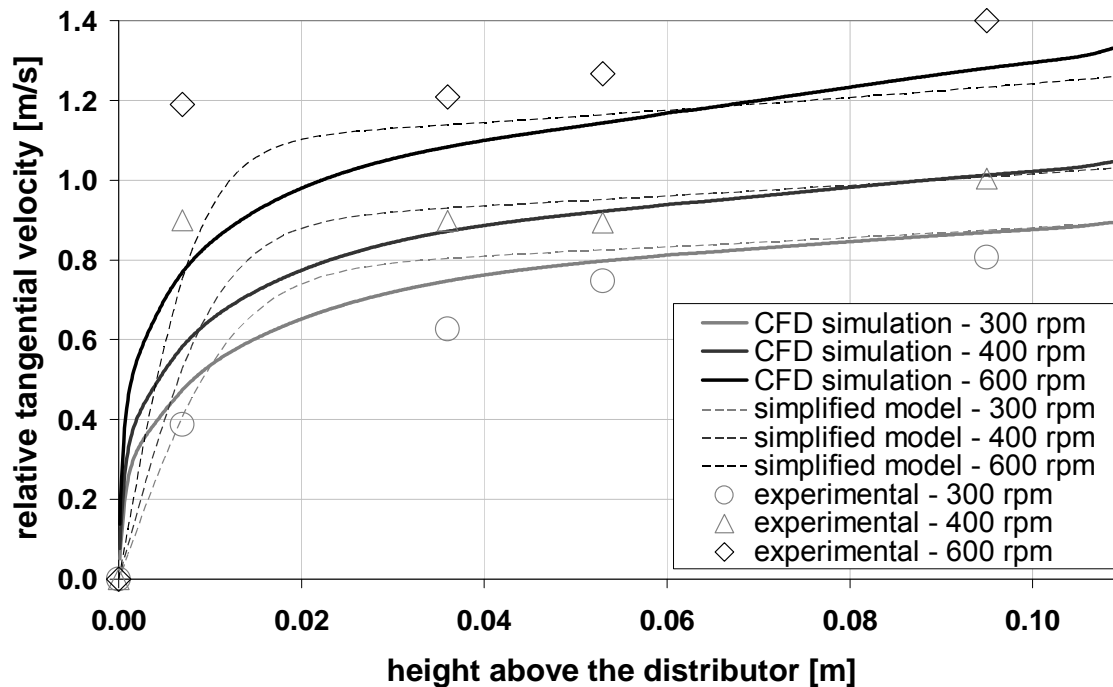


**Figure 6.7:** Comparison of the calculated tangential velocities (radial distributor velocity of 6.5 mm/s) with experiments

#### 6.1.4 The tangential velocity in the freeboard above the fluidized bed

The calculation of the tangential velocity in the freeboard above the fluidized bed was carried out in the same way as in the case of pure liquid flow. The fluid above the fluidized bed is assumed to be free of particles, i.e. the properties of the pure liquid has been used for the calculation. For these investigations quartz was used.

The fluidized bed was always built up in such a way that the water filled classifier was rotated at 300 rpm with 1 m<sup>3</sup>/h classification water. After the rotor had reached the desired speed the suspension feed valve was opened and 0.2 m<sup>3</sup>/h suspension flow (solids volume content 2%) was introduced. The accumulation of solids in the fluidized bed was visually observed and the suspension feed was closed when the desired bed height was reached. During the bed build up the fines were elutriated from the bed, so that the particle size distribution differs from the raw material. This procedure ensures that for all materials always a similar particle size distribution of the bed was achieved. The median particle size was  $d_{p,50} = 30 \mu\text{m}$ . For this test series only quartz was used as bed material.

To measure the influence of a fluidized bed on the tangential velocity profile of the freeboard the deflection of the tracer sphere was measured at a fixed radial position 37.5 mm above the distributor at a rotational speed of 300 rpm and at a water flow of 1 m<sup>3</sup>/h. Figure 6.8 shows as an example one picture of the sphere above the fluidized bed. In this series of experiments the bed height was stepwise increased from 0 m to 0.031 m, i.e. the minimal distance of the bed surface to the bottom line of the sphere was 1.5 mm. From the results (figure 6.9) it can be seen, that the tangential velocity is approximately constant between 0.8 and 0.9 m/s with increasing bed height.

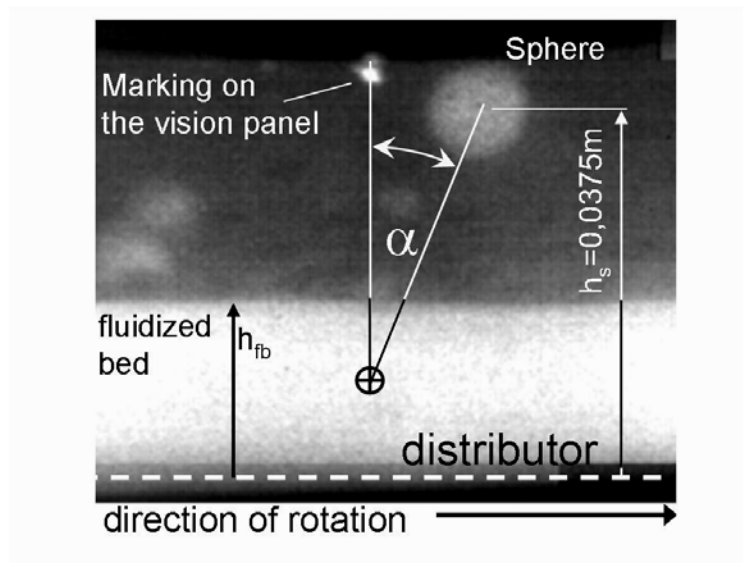


**Figure 6.8:** Photograph of the tracer sphere above the fluidized bed for the determination of the tangential velocity in the freeboard (rotational speed: 300 rpm; radial velocity at the distributor level: 5.0 mm/s)



**Figure 6.9:** The tangential velocity in the freeboard measured with the tracer sphere depending on the bed height (rotational speed: 300 rpm; radial velocity at the distributor level: 5.0 mm/s)

Only when the surface of the bed is approaching the bottom line of the sphere a slight drop of the tangential velocity can be seen which is caused by the much slower moving fluidized bed. At distances from the bed surface exceeding 5 mm the bed has no influence on the tangential velocity, so that the values from the simulation of the pure liquid flow are applicable to the freeboard.

### 6.1.5 Motion of the fluidized bed in the centrifugal field

To measure the influence of the Coriolis force on the fluidized bed itself, experiments were carried out with the freely floating tracer sphere as described in section 5.2.2. The measurements were done with radial velocities between 3 and 5 mm/s at 300 rpm and 400 rpm. A picture of the almost completely submerged floating sphere in the bed and its indicator is given in figure 6.10.

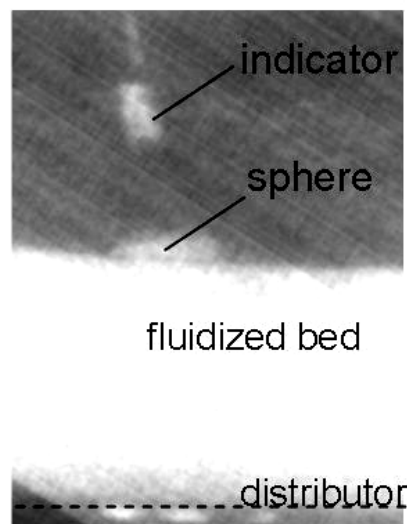


**Figure 6.10:** The freely floating sphere with the indicator in the fluidized bed

The figures 6.11 and 6.12 show the bed heights, the positions of the sphere in the bed and the tangential velocities of the sphere plotted vs. the water flow for rotational speeds of 300 and 400 rpm, respectively. For the lower rotational speed the sphere's position was always closely below the bed surface in the fluidized bed. It is assumed

that the sphere's tangential velocity equals the one of the bed at this position. The bed expands as the flow is increased. At the same time the sphere dips deeper into the fluidized bed, which is due to the decreasing bed density with increasing expansion. Furthermore an increase of the tangential velocity with increasing radial flow can be observed, as it has been found also for the pure liquid. For the higher rotational speed (400 rpm) the sphere again dips deeper into the bed at the beginning, but then it is fully submerged and starts to change its position. The higher the radial velocity the closer is the position of the sphere to the distributor. The fact, that the sphere does not completely sink to the bottom as soon as it is fully submerged, indicates that there is a vertical gradient of the porosity inside the bed with a higher porosity at the upper end and an increased density at the bottom.

The change of the sphere's position for water flows greater than 800 l/h is the reason for the decrease of the tangential velocity with further increasing water flows. Since the sphere has the tangential velocity of the bed at its current position, the decreasing tangential velocity indicates, that there is a gradient of the tangential velocity with lower velocities near the bottom. This is similar to the behavior of the pure flow, which also showed lower tangential velocities closer to the distributor. Furthermore, also the velocity increases with increasing water flow. Tangential velocities of the bed between 0.10 m/s and 0.25 m/s were measured.

Although the tangential velocity of the fluidized bed is much smaller than the tangential velocity of the water in the freeboard, the influence of the Coriolis force can be assessed to be significant on the fluidized bed. Thus the bed can be described as a fluidized bed moving in the direction of rotation. The optimization of the coarse discharge presented in chapter 5 is based on this finding.



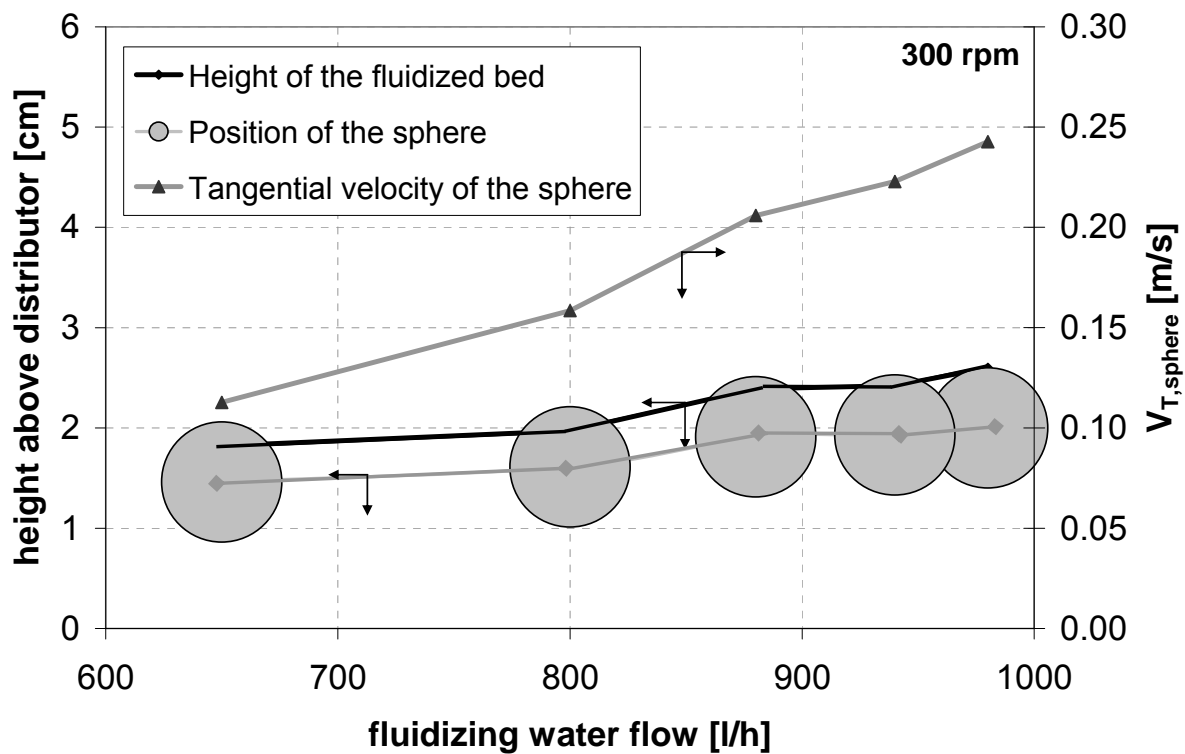


**Figure 6.11:** The position of the swimming sphere in the bed and its tangential velocity depending on the throughput at 300 rpm

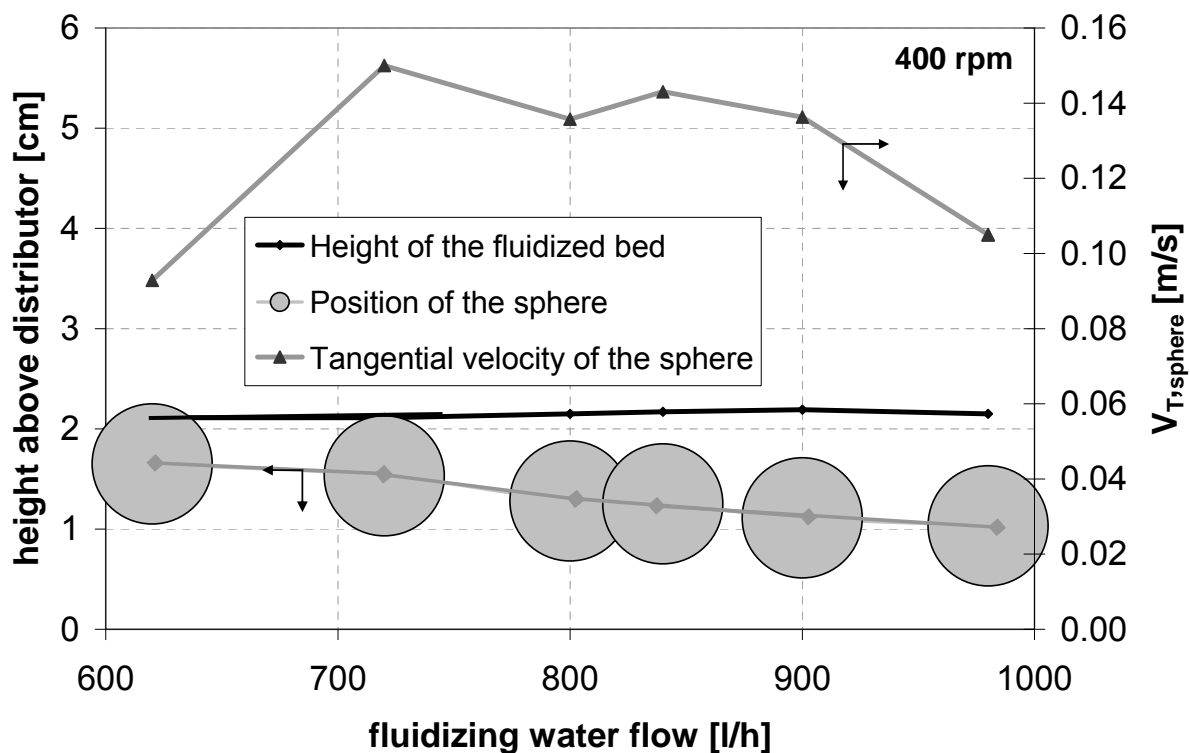


**Figure 6.12:** The position of the swimming sphere in the bed and its tangential velocity depending on the throughput at 400 rpm

## 6.2 Pressure drop

### 6.2.1 Pressure drop of the distributor

The pressure drop characteristics were measured as described in chapter 5 with a liquid column in a transparent tube installed below the distributor. In this way the distributor and the bed pressure drop are measured simultaneously. For the determination of the bed pressure drop it is important to analyze the distributor pressure drop characteristics first. A linear pressure drop profile with the slope  $K_D$  (cf. equation 5.21) is obtained and  $K_D$  was measured before each experiment at different angular velocities. Figure 6.13 shows the pressure drop profile of the distributor after the installation of new distributor material at different angular speed rates. The profile is linear and independent of the angular velocities. Porous distributor plates are known to be sensitive to clogging (D. Kunii, O. Levenspiel, 1991). Figure 6.14 illustrates the change of the pressure drop coefficient  $K_D$  of the porous distributor plate after several hours of operation.

The pressure drop coefficient increases significantly during long term operation. In general high distributor pressure drops are known to increase the fluidization stability and therefore high bed pressure drop ratios are favored in fluidized bed applications (D. Kunii, O. Levenspiel, 1991). Figure 6.15 illustrates the fluidization performance for a new distributor and after 80 hours of operation at the same operating conditions. The fluidized bed surface on the new distributor is very smooth, where on the right side void eruptions and an uneven bed surface can be observed, i.e. the fluidization performance is becoming worse. An explanation is that clogging occurs unevenly distributed over the distributor. That results in a reduced fluidization down to a collapse of the bed in some regions and to higher fluidizing velocities in other regions. The classification performance is influenced by the fluidizing behavior and therefore the distributor was exchanged after 80 hours of operation.

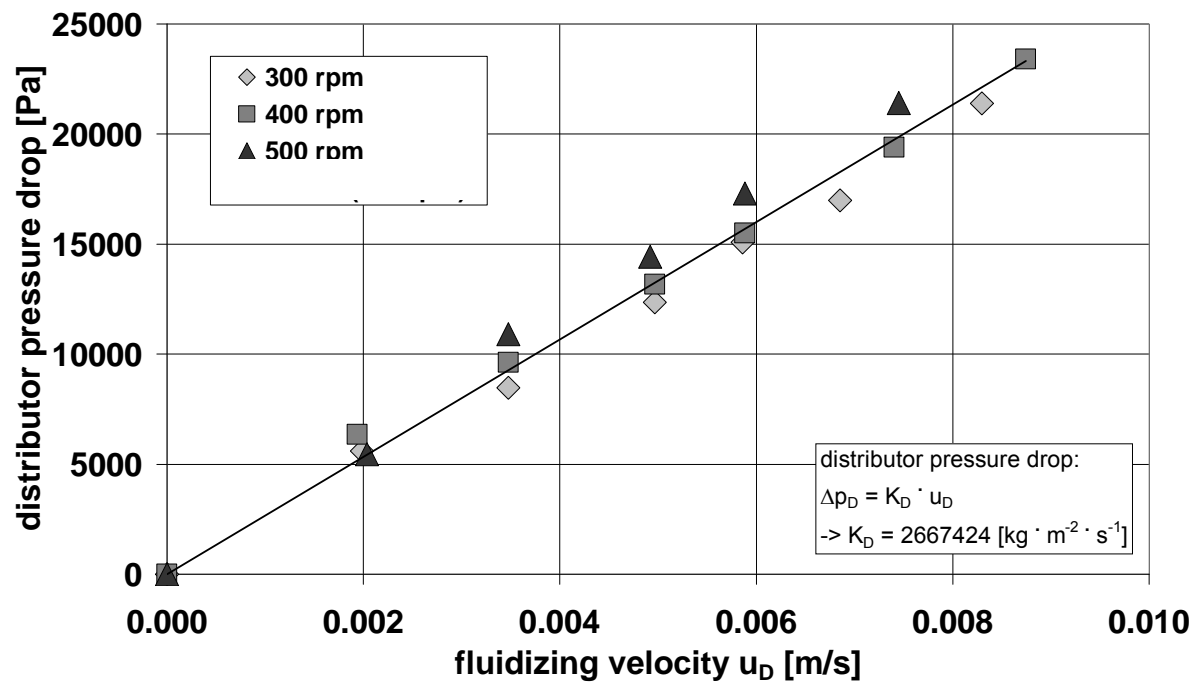


Figure 6.13: Pressure drop profile of a new porous distributor plate

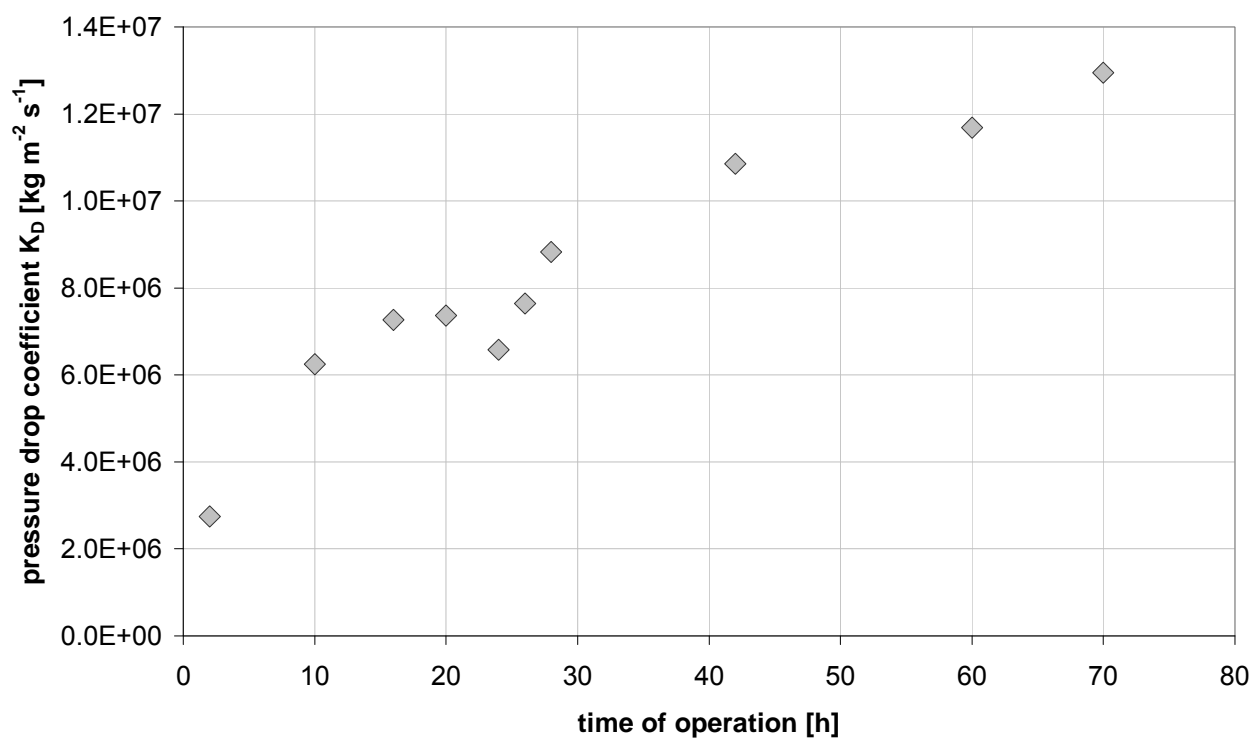
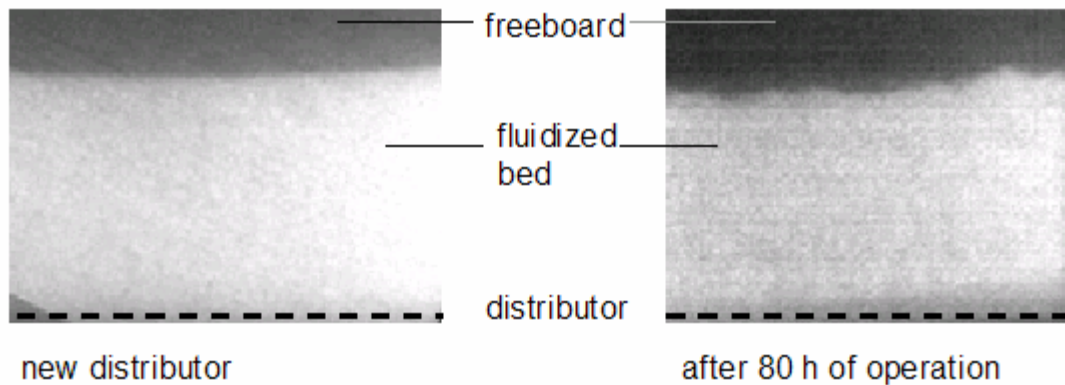


Figure 6.14: Time dependency of the distributor pressure drop



**Figure 6.15:** Fluidized beds at 400 rpm and  $u_D = 0.0025$  m/s (corresponding to  $1.7 u_{mf}$ ) fluidizing velocity (left: new distributor; right: after 80 hours of operation)

### 6.2.2 The fluidized bed pressure drop

Knowing the distributor pressure drop characteristic the bed pressure drop profile can be determined from the height of the liquid column using equation 5.24. The pressure drop characteristics of glass beads, limestone and quartz were investigated. The fluidized bed was build up with a sealed coarse discharge under a constant solids feed rate of 200 l/h at 300 rpm. During the bed build up classification took place, i.e. a fines fraction was elutriated from fluidized bed. Using always the same build-up procedure assured that different raw materials with densities in the range between  $2500 \text{ kg/m}^3$  and  $2650 \text{ kg/m}^3$  have comparable particle size distributions in the fluidized bed. By measuring the incoming and outgoing solids mass flows the solids mass of the bed was calculated. The suspension feed and the fluidizing water were shut down when the desired bed mass was reached. The sudden shutdown of the fluidizing water is causing the bed to collapse immediately. Figure 6.16 shows the particle size distribution of the bed materials glass beads, limestone and quartz. The median diameters were  $d_{p,50,\text{quartz}} = 31 \text{ }\mu\text{m}$ ,  $d_{p,50,\text{limestone}} = 30 \text{ }\mu\text{m}$  and  $d_{p,50,\text{glass}} = 30 \text{ }\mu\text{m}$ . From the fixed bed state the fluidizing water is stepwise increased until a fluidizing velocity of 0.005 m/s is reached and then decreased back to the fixed bed state. This procedure was chosen to find out, if differences between the profiles of increasing and decreasing fluidizing velocities occur.

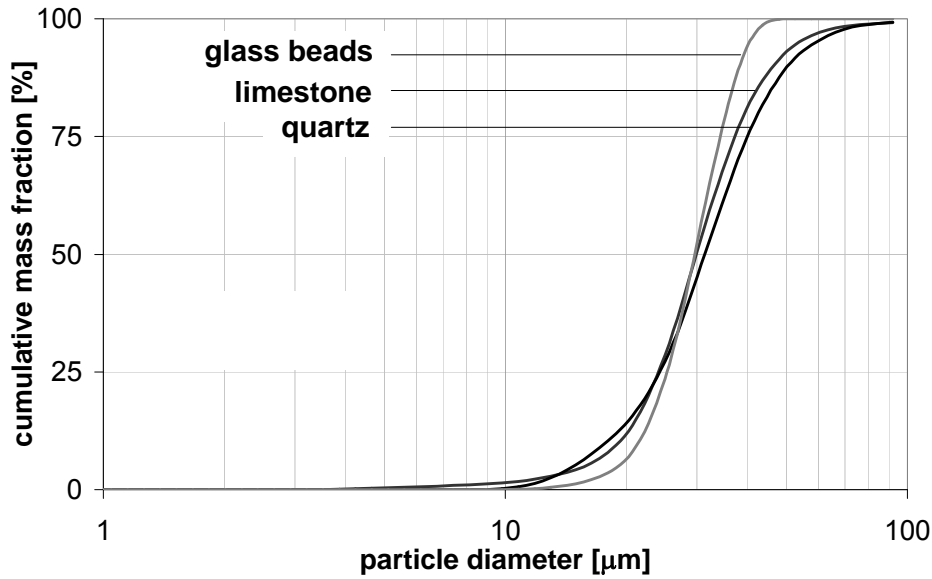


**Figure 6.16:** Particle size distribution of the bed materials

The pressure drop profile of glass beads fluidized at 400 rpm is pictured in figure 6.17. With increasing fluidizing velocity an increase of the bed pressure drop can be observed until a peak at approximately  $u_D = 0.0016$  m/s of  $\Delta p_B = 15000$  Pa is reached. Beyond  $u_D = 0.0016$  m/s the pressure drop is decreased back to the static pressure drop and stays constant between 12000 and 14000 Pa. A behavior like this has often been described in the literature (e.g. Kunii & Levenspiel, 1991). Just right before the onset of fluidization, the pressure drop reaches a maximum slightly higher than the static bed pressure drop with a fixed bed porosity  $\varepsilon_m$  slightly below the minimum fluidizing porosity  $\varepsilon_{mf}$ . A further increase of the distributor velocity causes the fixed bed to unlock, i.e. particles are getting fluidized and the bed porosity is increased from  $\varepsilon_m$  to  $\varepsilon_{mf}$ . As the porosity measurement in the rotating system is not precise enough to distinguish between fixed bed porosity  $\varepsilon_m$  and minimum fluidizing porosity  $\varepsilon_{mf}$ , they are treated as being the same.

With decreasing fluidizing velocity the bed volume is reduced until the particles form a fixed bed with the porosity near  $\varepsilon_{mf}$ . From the measurements a minimum fluidizing velocity at the distributor level of 0.0016 m/s is obtained. The scatter of the measured

points indicates the limits of accuracy of the pressure drop measurement in the rotating system.

The calculated fluidized bed pressure drop characteristic is indicating that the bed pressure drop is slightly decreasing with increasing fluidizing velocity. This is contrary to the situation in the gravitational field where the bed pressure drop is independent of the fluidizing velocity. The explanation is, that in the rotating system with increasing fluidizing water flow the bed is expanding. During expansion the center of gravity of the bed will be displaced towards the axis of rotation where the centrifugal acceleration is lower and therefore the “weight” of the bed is apparently reduced. However, this effect is very small and hardly to be seen in figure 6.17.

The results for quartz with a solids mass in the fluidized bed of  $m_s = 1.6$  kg are pictured in figure 6.18. A linear pressure drop characteristic can be observed in the fixed bed state with distinct differences between increasing and decreasing water flow. At approximately 0.0013 m/s the transition from the fixed to the fluidized bed takes place. The transition from fixed to fluidized bed is much clearer in the case of quartz compared to glass beads. The corresponding pressure drop is  $\Delta p = 12500$  Pa at the state of incipient fluidization. The fluidized bed pressure drop is quite in a good agreement with the calculated pressure drop of approximately 13000 Pa.

To confirm the model for quartz, the theoretical profile was compared with experimental data at a higher rotational speed of 500 rpm and a lower solids mass of  $m_s = 1$  kg (figure 6.19). Using a minimal fluidizing porosity of  $\varepsilon_{mf, quartz} = 0.50$  and a minimal fluidizing velocity of  $u_{mf} = 0.0023$  m/s, the pressure drop for incipient fluidization was calculated from the intersection of the fixed and fluidized bed pressure

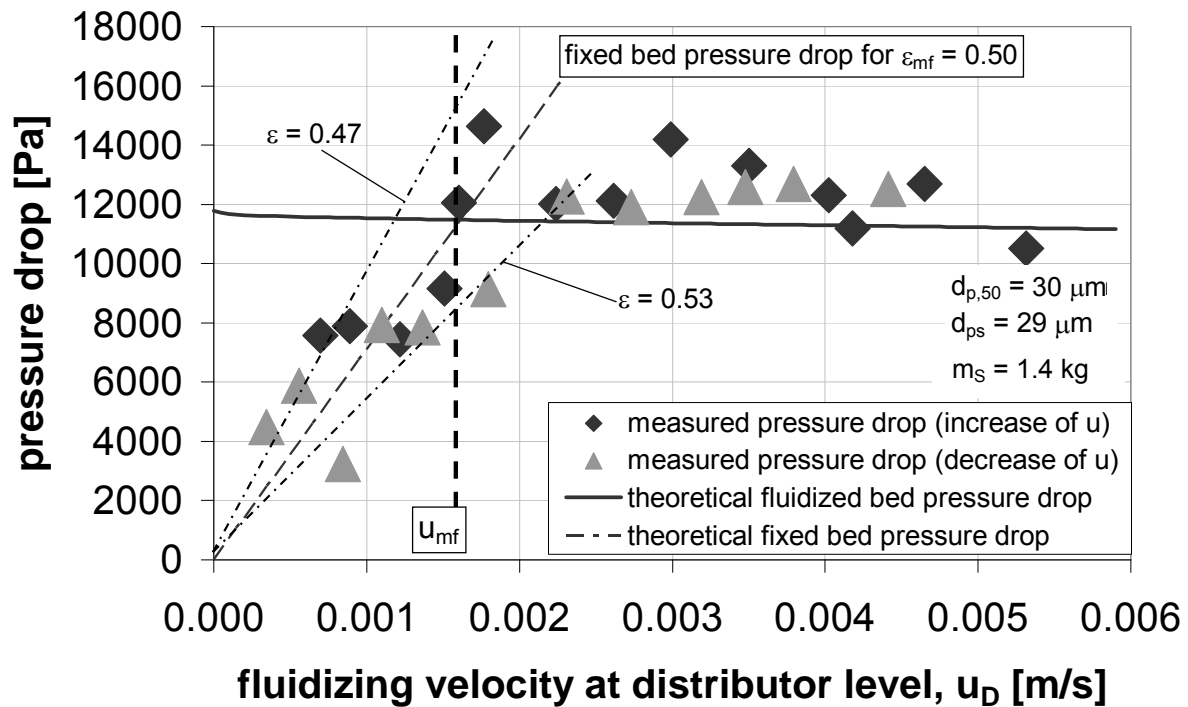


Figure 6.17: Measurement of the minimum fluidizing velocity for glass beads at 400 rpm

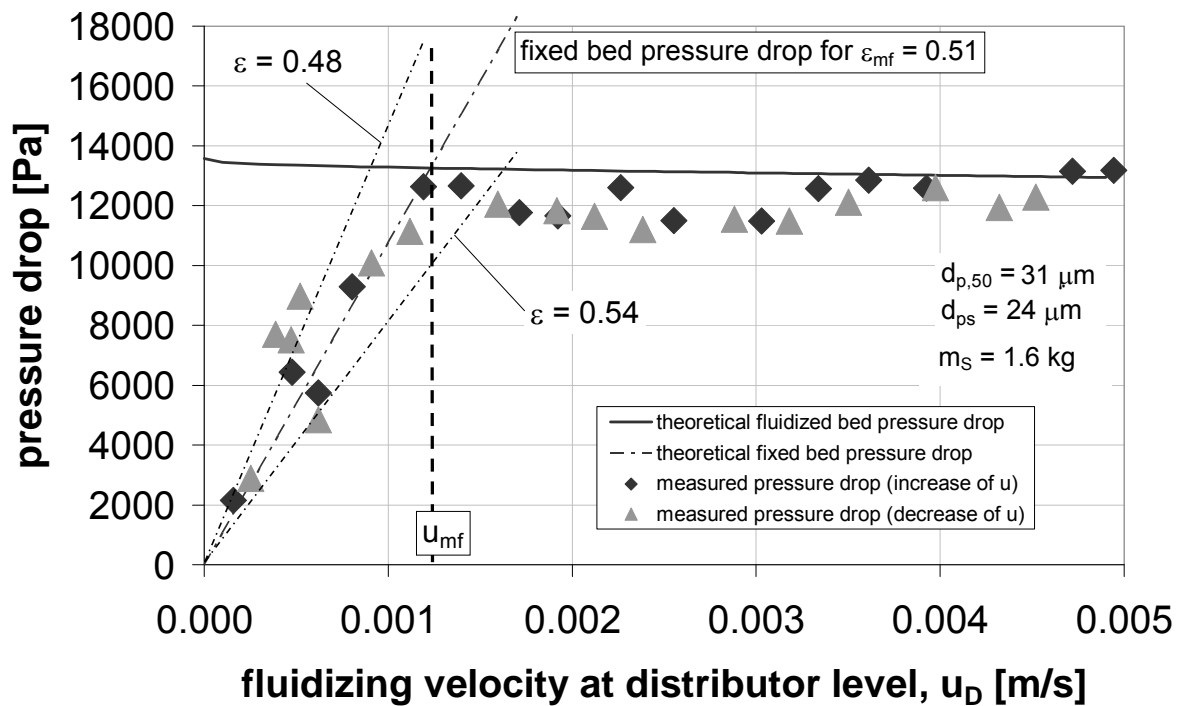
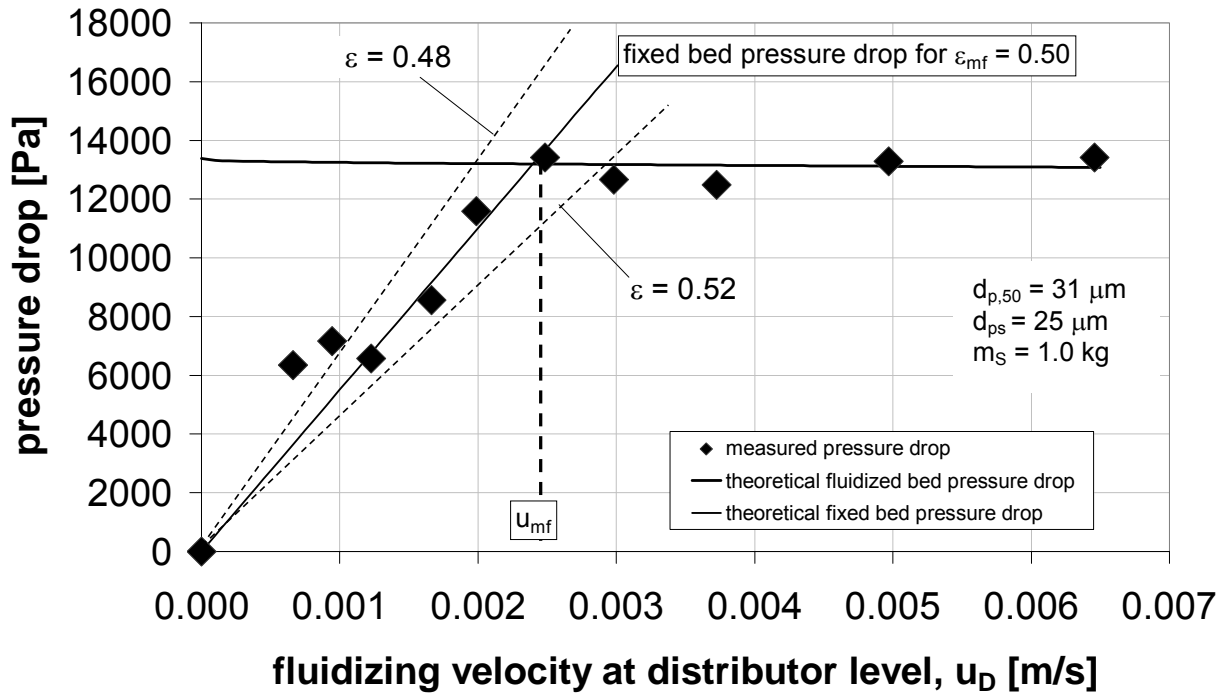


Figure 6.18: Measurement of the minimum fluidizing velocity for quartz at 400 rpm

drop curves. A fluidized bed pressure drop  $\Delta p_{\text{bed}} = 13000$  Pa was calculated, which is in good agreement with the measured results.



**Figure 6.19:** Measurement of the minimum fluidizing velocity for quartz at 500 rpm

The investigation of limestone is pictured in figure 6.20. With increasing fluidizing water flow a maximum in the bed pressure drop is located at approximately 0.0016 m/s with  $\Delta p = 15600$  Pa. With further increase of the fluidizing velocity the pressure drop is then reduced to a range between 12000 and 14000 Pa.

The measurement of the pressure drop profiles allows a determination of the minimum fluidizing velocity at the intersection of fixed and the fluidized bed pressure drop lines. At fluidizing velocities of above  $1.5 \times u_{mf}$ , no difference between increase and decrease was observed, i.e. the bed is completely fluidized. It can therefore be concluded that, in order to ensure homogeneous fluidization for classification, a fluidizing velocity of  $u_D$  exceeding  $1.5 \times u_{mf}$  is necessary. Increasing the fluidizing velocity further results in an increase of the tangential velocity, which enhances unfavourable turbulence.



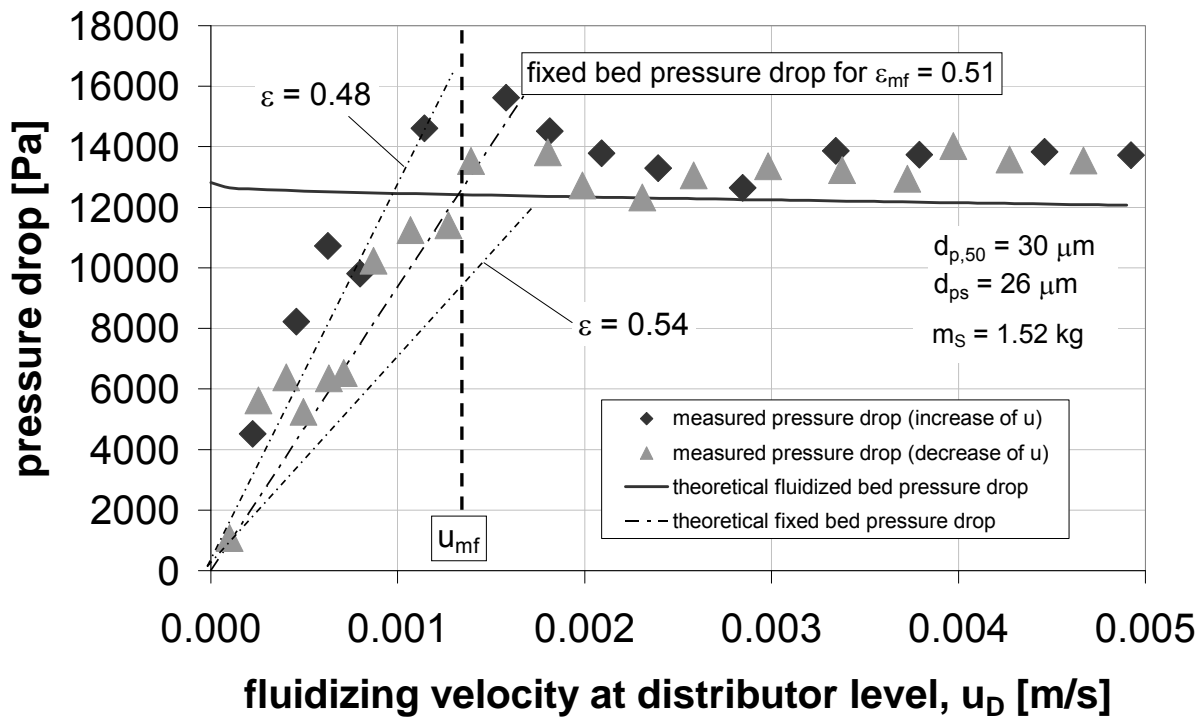


**Figure 6.20:** Measurement of the minimum fluidizing velocity for limestone at 400 rpm

### 6.3 The expansion behavior of the fluidized bed

The expansion behavior of fluidized beds of quartz, glass beads and limestone was investigated. The build up of the bed was conducted in the same way as for the pressure drop characterization, so that particle size distributions as shown in figure 6.16 were achieved. Experiments on the bed expansion behavior were carried out by varying the angular speed and fluidization velocity. A Richardson Zaki type power law is used for the description of the expansion behavior. For the determination of the exponent  $n$  the porosity  $\epsilon$  on the abscissa is plotted versus the ratio of fluidizing and terminal velocity  $u/u_t$  on the ordinate on a logarithmic grid. As the Richardson Zaki exponent  $n$  varies outside the Stokes range, i.e.  $Re_p > 0.2$ , which is the case for the

investigated fluidized beds, the plots with the Richardson Zaki exponents from literature are depending on the angular velocities. In figures 6.21 – 6.23 the plots of the Richardson Zaki correlation for the materials glass beads, limestone and quartz are shown for rotational speeds of 300 and 600 rpm. The deviation of both plots are hardly detectable, so that the description of the expansion behavior was conducted with only one exponent for the range between 300 and 600 rpm. From the literature exponents between 4.36 and 4.42 were calculated under gravitational acceleration for the same range of Reynolds numbers (Richardson, Zaki, 1954).

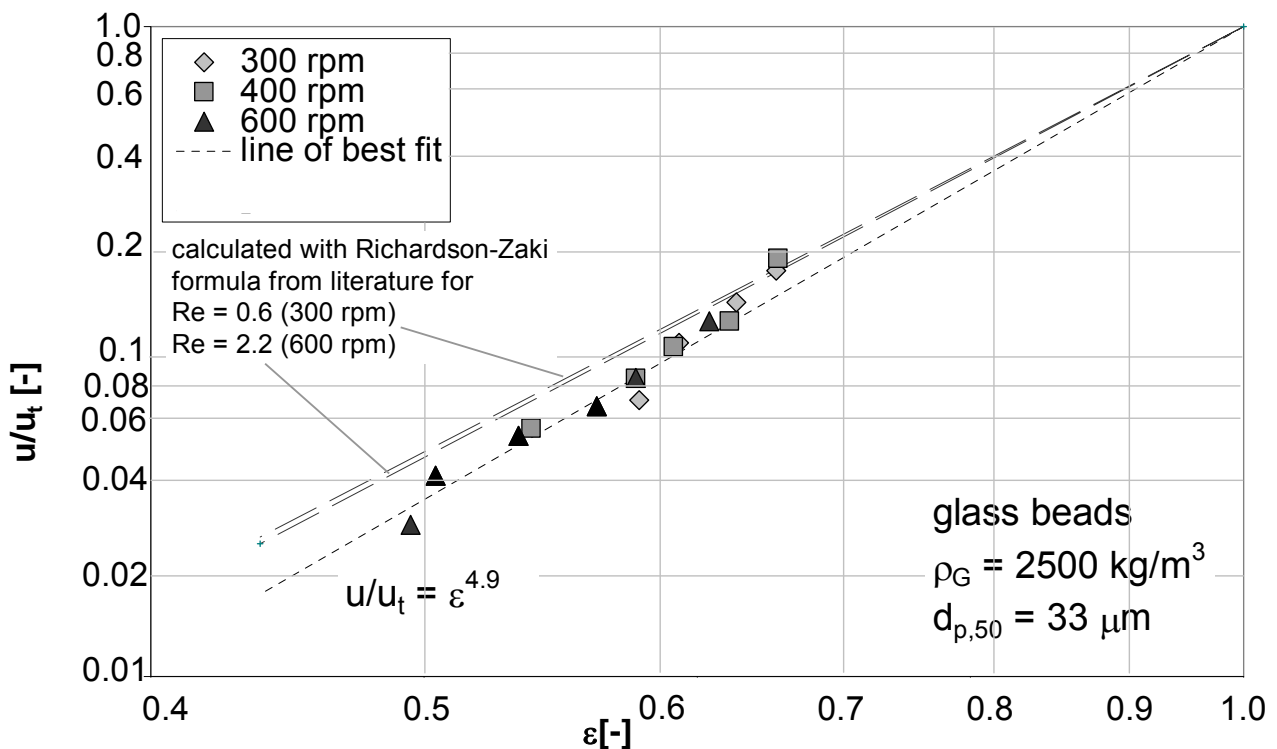


**Figure 6.21:** Bed expansion behavior of fluidized glass beads

In figure 6.21 the expansion behavior of glass beads is presented. The expansion behavior was investigated for the rotational speed rates of 300, 400 and 600 rpm. The data points can easily be represented by a straight line with the slope  $n$  of 4.9. The exponent is slightly higher than  $n$  obtained from literature, which is between 4.36 and 4.42.

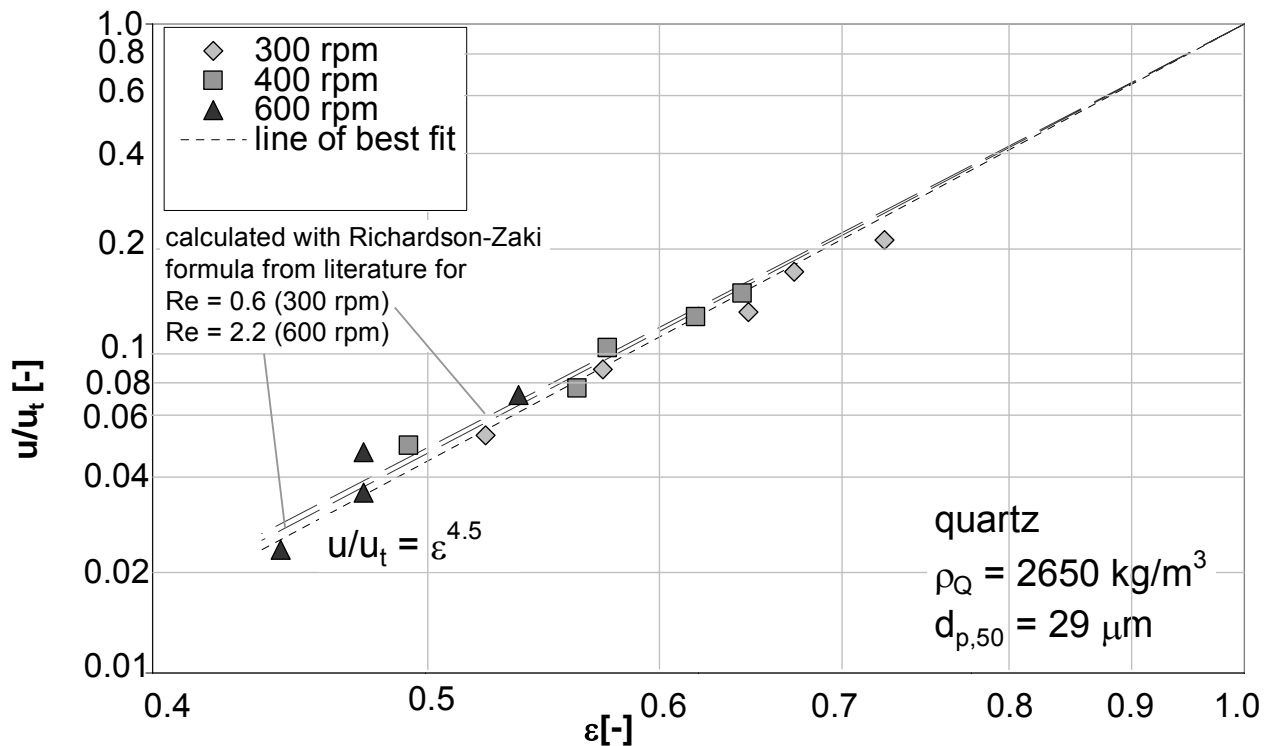


**Figure 6.22:** Bed expansion behavior of fluidized quartz powder

Figure 6.22 shows the expansion behavior of quartz. Here also all data points can be represented by a single straight line, indicating, that the usage of a common exponent for the range between 300 and 600 rpm is valid. The exponent for quartz has a value of  $n = 4.5$ . The expansion behavior of limestone is shown in figure 6.23. The exponent for the rates between 300 and 600 rpm is 5.9 in this case.

The spherical glass beads which are expected to be closest to the literature values have a slightly higher  $n$  value than in the literature, which means that for given  $u/u_t$   $\epsilon$  and therefore the bed expansion is higher in the centrifugal field than in the gravitational one. This can be explained by the superimposed tangential movement of the bed in the centrifugal field.

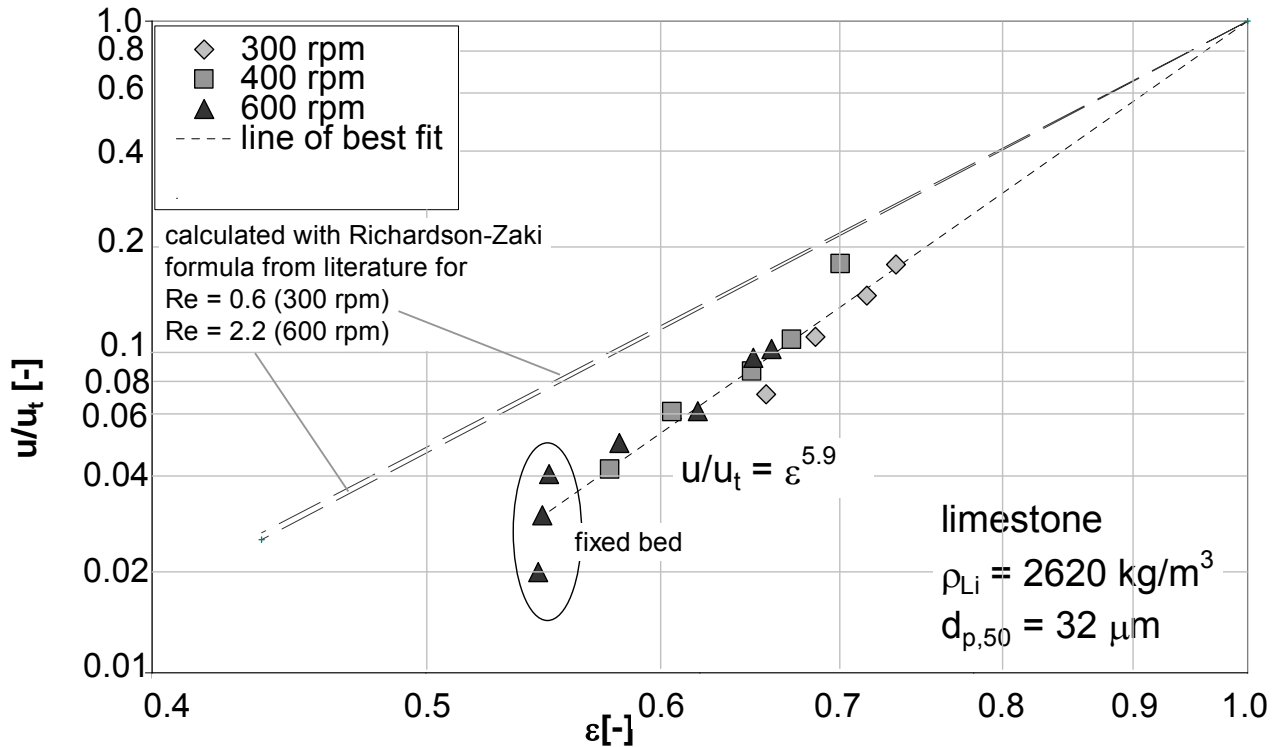


**Figure 6.23:** Bed expansion behavior of fluidized limestone

#### 6.4 Analysis of the particle size distributions

For the characterization of the classification performance a proper analysis of the particle size distributions is essential. For this purpose many sophisticated methods are available in industry. The most easiest and cheapest method is screening, but screens are only available for particle sizes down to  $25 \text{ }\mu\text{m}$ . Another method is the sedimentation technique, which can be performed either in the normal gravity or in a centrifugal environment. While gravity sedimentation is not suitable for particle sizes below  $10 \text{ }\mu\text{m}$  due to too low settling velocity, the centrifugal sedimentation analysis was tested for the experimental materials in the disc centrifuge of the CPS company (CPS Instruments Europe, Oosterhout, The Netherlands). The analysis of the used materials revealed that this method is only precise between  $0.01$  and  $10 \text{ }\mu\text{m}$ . Large

particles are not detected, because of too high settling velocities in the centrifugal field, whereby the sedimentation has to be assessed as a not suitable analysis method for the purpose of this work.

The determination was therefore conducted by laser diffraction analysis. Light from a laser is sent into a cloud of particles, which are suspended in a transparent liquid e.g. distilled water. The particles scatter the light, smaller particles scattering the light at larger angles than bigger ones. The scattered light can be measured by a series of photodetectors placed at different angles. This is known as the diffraction pattern for the sample. The diffraction pattern can be used to measure the size of the particles using light scattering theory that was developed in the early 20th century by Mie. As the instrument measures clouds of particles rather than individual ones, it is known as an "ensemble" technique, with the advantage that at smaller sizes e.g. 10 microns, the system is measuring millions of particles which gives some statistical significance to the measured results.

As the Mie theory is very complex a large amount of computing power and the knowledge of the refraction index are required to evaluate the particle size distribution. Therefore a simplified model, also known as Fraunhofer approximation, is widely used for the evaluation. As the Mie theory is valid for the whole spectrum of particle sizes, the Fraunhofer approximation is found to be unreliable in the lower micron range (Malvern, 2000), i.e. for particles  $< 10 \mu\text{m}$ . Therefore the two laser diffraction analyzer of the Institute of Solids Process Engineering and Particle Technology at Hamburg University of Technology, namely the Beckman Coulter (LS13320c – Beckman Coulter GmbH, Krefeld, Germany) and HELOS (Sympatec GmbH, Clausthal – Zellerfeld, Germany) were tested concerning their accuracy in the particle size measurement. The HELOS provides the Fraunhofer approximation only, while the Beckman Coulter provides both.

To find the most accurate evaluation method, it is necessary to compare the particle size distributions of the same sample with a method, where accuracy can be assured. This method can be an optical evaluation of >1000 particles taken by SEM pictures of the sample. For the evaluation the software SCANDIUM (Olympus Soft Imaging Solutions GmbH, Münster, Germany) was applied. SCANDIUM detects each particle on SEM pictures and calculates each diameter from the cut surface. The detection enables the calculation of a number density distribution, which can be converted in a mass density distribution. Picture 6.24 shows the detection of limestone particles with SCANDIUM. Detecting some thousand of particles this way (approx. 10 pictures) gives an adequate number of particles for a particle size distribution determination.

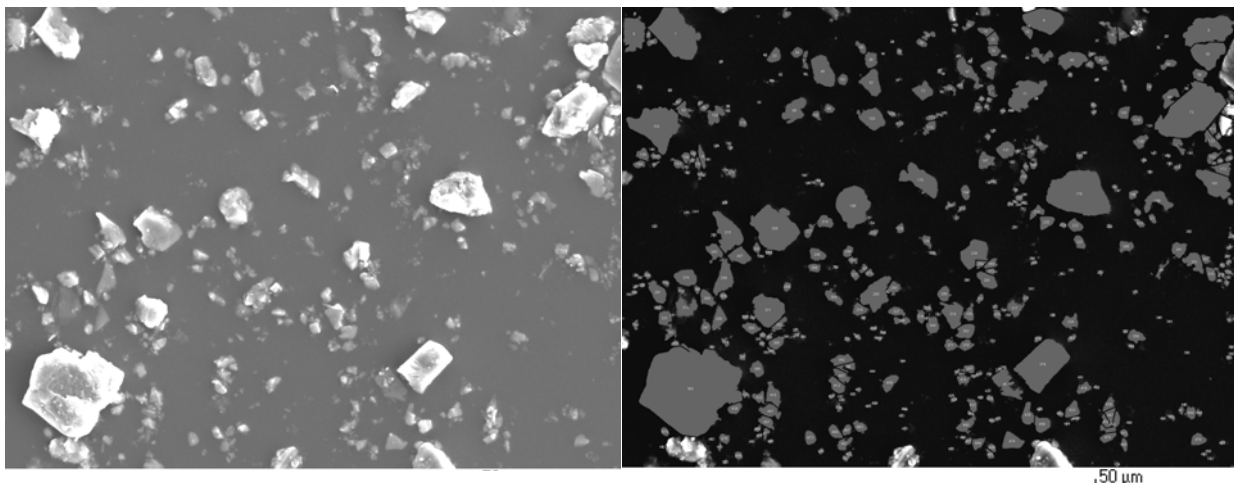


**Figure 6.24:** Limestone particles on a SEM picture (left) detected with the evaluation software SCANDIUM (right)

The comparison of the methods for a limestone sample in figure 6.25 revealed that the Mie evaluation and the SCANDIUM detection are in a quite good agreement in the range below 10  $\mu\text{m}$ . The deviation in the range above 25  $\mu\text{m}$  can be explained by the fact that not enough particles can be taken into account in the coarse region. As the Fraunhofer approximation is known to be inaccurate in the fines region it can be concluded that the fines content indicated in figure 6.25 is overrated, i.e. the detected

particles do not exist. Previous measurements (Schmidt, 2004) were conducted with HELOS and evaluated with the Fraunhofer approximation. A strong fishhook effect, wherein the recovery of fine particles in the coarse fraction increases with decreasing particle size, was observed by Schmidt. This effect can now be explained by overrating the fines due to an evaluation error of the Fraunhofer approximation. On the contrary the evaluation with the Mie theory turns out to be accurate as is demonstrated by the optical evaluation.

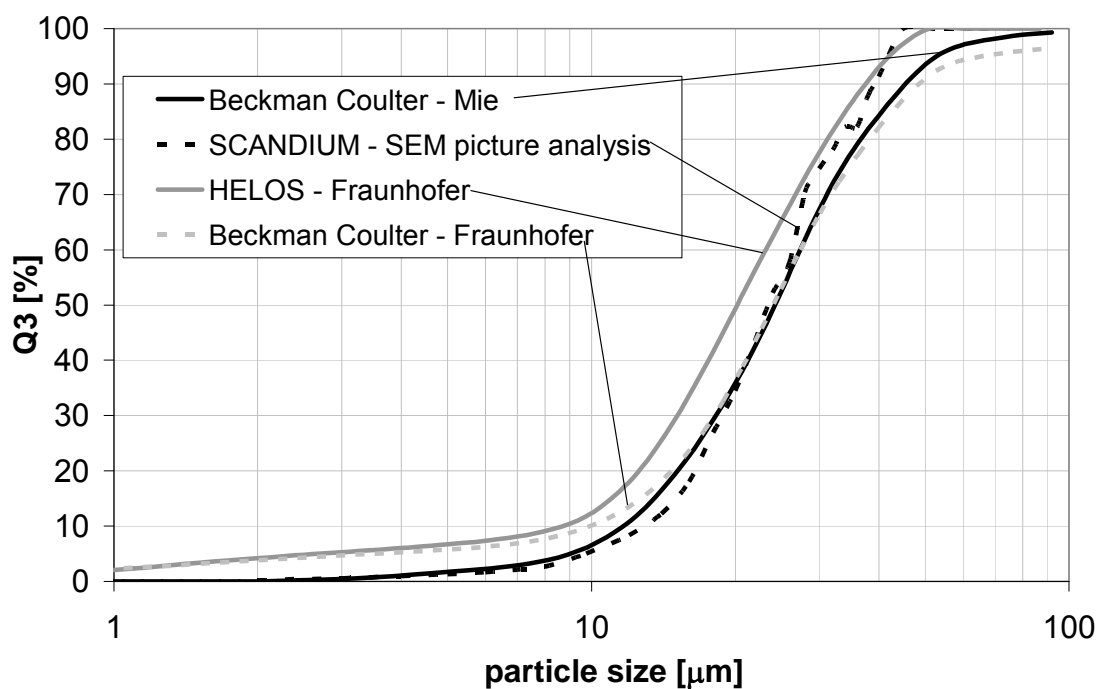


**Figure 6.25:** Limestone sample analyzed with different methods

To illustrate the effect of the evaluation error, the density distributions and the separation efficiency curves of the classification experiment from the 23.th May 2008 evaluated with Mie theory and Fraunhofer approximation are presented in figure 6.26. The top left diagram shows the density distributions of the suspension feed, the coarse and the fines fractions. Submicron particles are really rare and are hardly to detect in the fines fraction and the suspension feed. These findings were confirmed by the SEM-analysis as described above. What happens when the Fraunhofer approximation

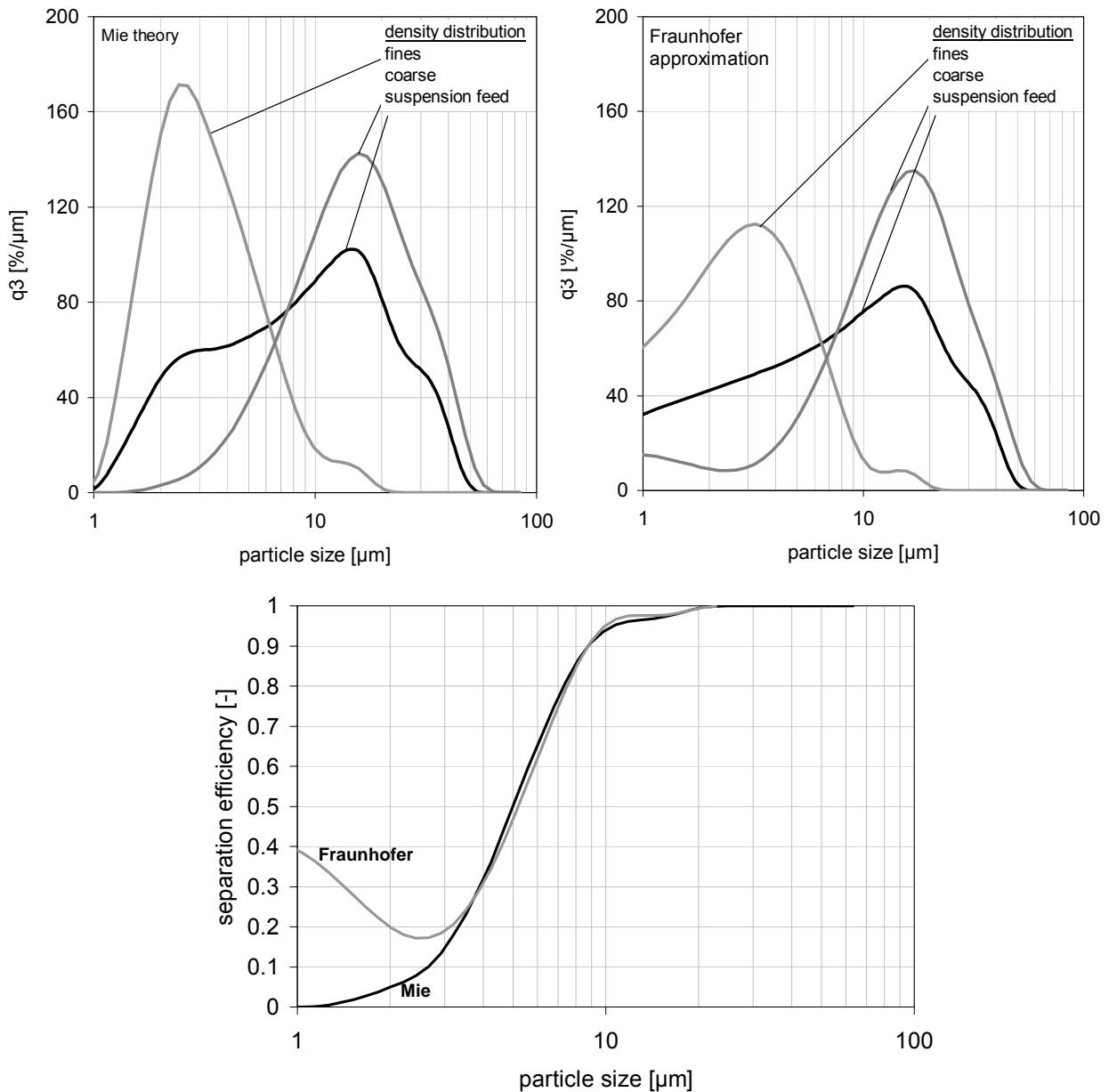


**Figure 6.26:** Mass density distributions before and after quartz classification and separation efficiency curve evaluated with Mie theory and Fraunhofer approximation (experiment 23th May 2008: 700 rpm; fluidizing velocity: 0.0031 m/s)

is applied is shown on the picture at the top right. In the range below  $1\ \mu\text{m}$  up to  $10\ \mu\text{m}$  the particle classes are increased by not existing particles, what has an significant effect on the separation efficiency curve, especially in the regions at the upper or lower end, where the total mass in the particle classes are small. A ‘detection’ of not existing particles in the coarse fraction combined with a large coarse fraction  $c$  results in a



fishhook effect as shown at the bottom of figure 6.26. This fishhook effect is only based on evaluation errors of the Fraunhofer approximation in the range below 10  $\mu\text{m}$ . Thus the particle analysis in this work has been conducted with the Beckman Coulter using the Mie theory only.

### **6.5 Classification experiments with the original configuration of solids discharge**

Previous classification experiments were carried out with the elbow lever mechanism for coarse withdrawal. As described above the elbow lever mechanism is not capable to control the bed height accurately, which, however, is necessary for a sharp classification. Another problem is the occurrence of a flushing out of the bed material, what leads to misclassification due to bypass of fines to the outlet.

In the previous work (Schmidt, 2004) inaccurate separation efficiency curves were found with a huge amount of fines being misclassified into the coarse fraction. Figure 6.27 is picturing separation efficiency curves of classification experiments at 400 rpm by Schmidt, where the suspension feed to fluidizing water ratio was investigated. Schmidt found that the lower the ratio the more efficient is the classification performance. The water injected through the feed ports is only affecting particles above the ports and is less homogeneous distributed compared to an injection through the distributor, so that the better classification performance for a lower ratio can be explained.

But even the separation efficiency curve with the lowest suspension feed-to-fluidizing water ratio shows a very strong fishhook effect. On one hand the fishhook can be explained by errors in the evaluation of the laser diffraction patterns with the Fraunhofer model, resulting into an overrating of fines. On the other hand a reason might be the use of the elbow lever mechanism for coarse discharge. For clarification

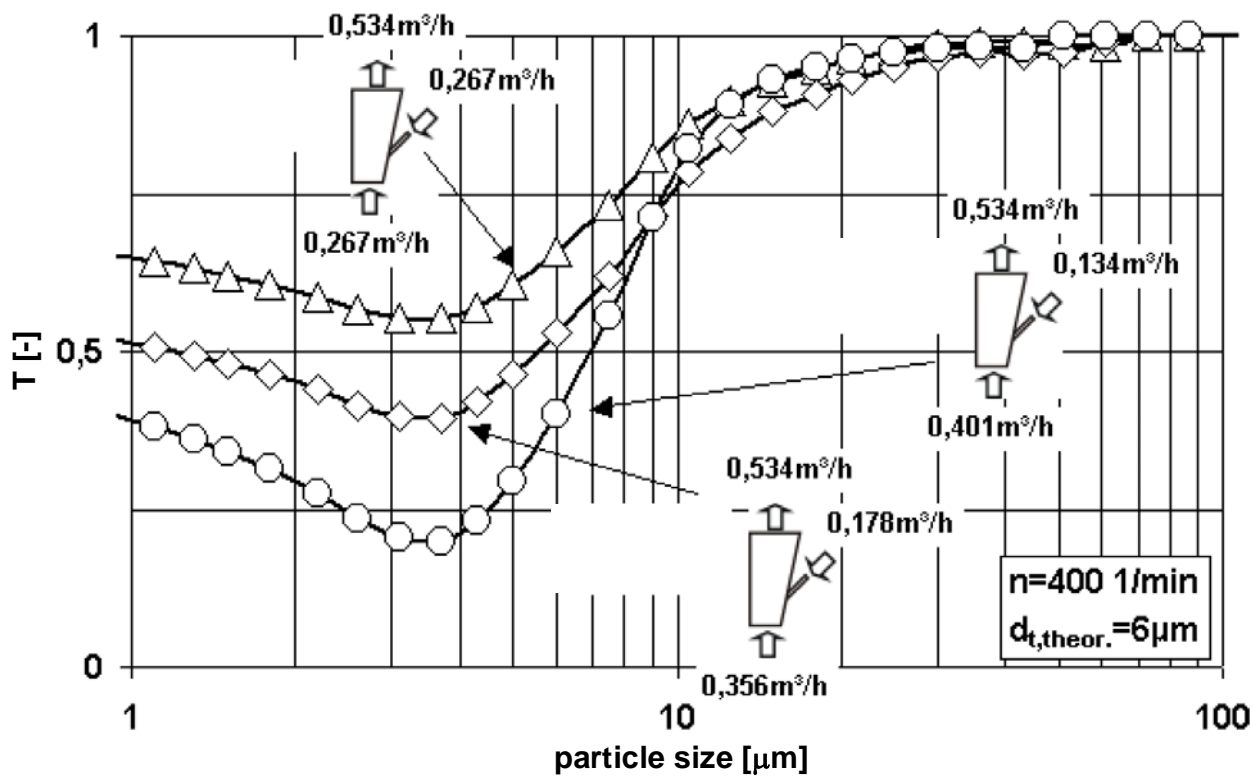


**Figure 6.27:** Classification experiment at 400 rpm rotational speed at different suspension feed to fluidizing water ratios (Schmidt, 2004)

new experiments with the elbow lever mechanism were conducted at 400 rpm and the particle size distributions were evaluated by the Mie theory. Figure 6.28 shows separation efficiency curves of quartz classified at 400 rpm rotational speed and at a fluidizing velocity of  $u_D = 0.004$  m/s. As proposed by Schmidt a low ratio of suspension feed to fluidizing water was chosen, namely less than 1:4. In these separation efficiency curves a high amount of fines being misclassified to the coarse fraction were found. The only explanation is a bypass flow of fines to the coarse outlet, when the fluidized bed is flushed out. The misclassification is visible for all of the taken samples. Another classification experiment was carried out with limestone at the same rotational speed (figure 6.29). In this case the misclassification of fines is much higher and the split much lower compared to the previous experiment with quartz. The difference to quartz can not only be explained by the material properties, which are similar. The reason might be rather that the coarse discharge was wider opened and at different time intervals. As mentioned before the controlling of the coarse discharge operated

with the elbow lever, is very inaccurate. To adjust the needle valves in exactly the same positions as in previous experiments is nearly impossible. A precise reproduction of the experimental conditions can not be achieved. The needle valves operated with an elbow lever mechanism have turned out to be unsuitable for classification purposes in the centrifugal field.

Therefore the needle valves were replaced by the coarse discharge nozzles (II-IV), which were used in the following only.

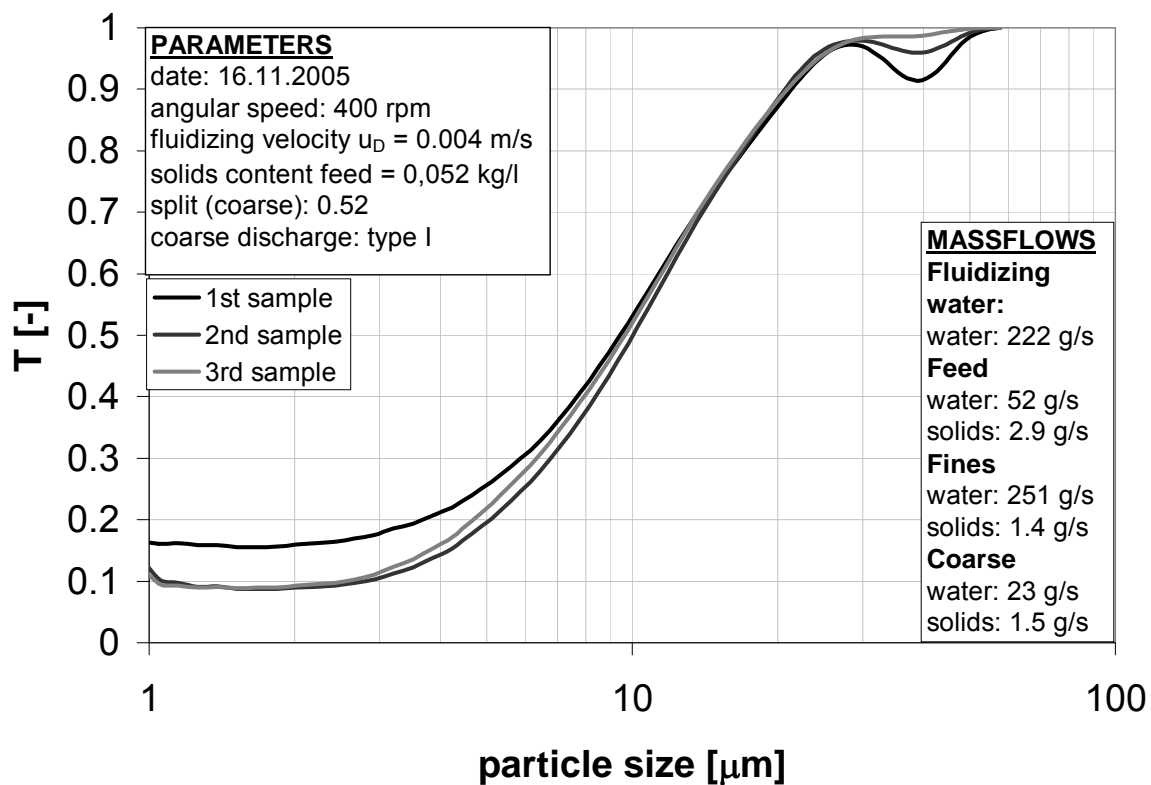


**Figure 6.28:** Separation efficiency curved of quartz classification operated with needle valves (coarse discharge type I)

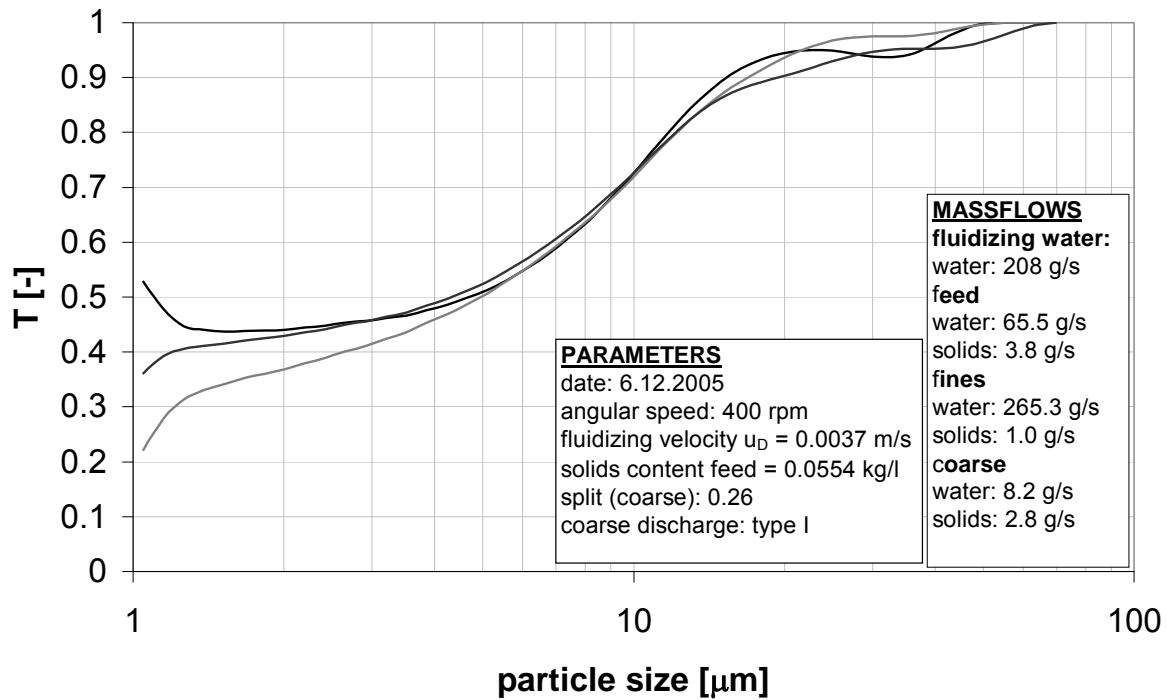


**Figure 6.29:** Separation efficiency curve of limestone classification operated with needle valves (coarse discharge type I)

## 6.6 Estimation of the outgoing mass flows for classification with the optimized coarse discharge nozzles

In chapter 5 a correlation was developed to estimate the outgoing solid mass flows of the discharge nozzles (type II-IV). The prediction of solid mass flows is of major interest, when the operating conditions for a classification task have to be chosen. Therefore the predicted mass flows for a constant outlet friction coefficients  $\xi$  for quartz and limestone were compared with the experimental determined mass flows. Additionally bed porosities were compared with the solid mass content in the outlet of the coarse discharge. Figure 6.30 shows for nozzle IV the difference between the bed porosities and the porosities of the coarse suspension for some selected classification experiments with the coarse discharge type IV. The bed porosity lies in all experiments below the one of the coarse suspension. The difference can be explained by a water slip in the outlet, i.e. the water flows with a higher velocity than the solid particles.

Figure 6.30 shows for higher angular velocities a higher difference between bed and coarse suspension porosity or in other words a higher fluid slip. With decreasing bed porosity and decreasing angular velocity the water slip decreases also. The slip in the coarse discharge is difficult to predict and a detailed study is needed to model it, what is not part of this work. The slip is influencing the apparent viscosity in the nozzle and the viscosity is influencing the outgoing currents. Therefore the laminar content is not considered in the modeling of the solid mass flow out of the bed, instead the general formula proposed in chapter 5.6.4 is used.

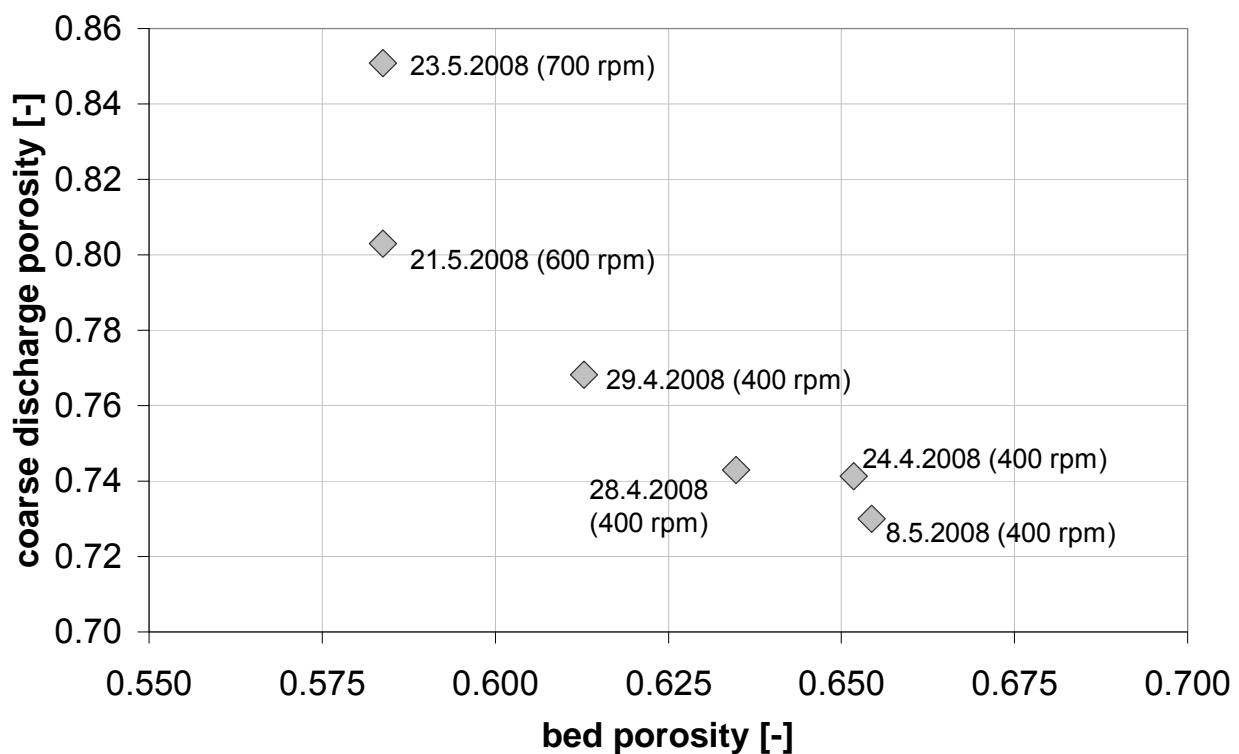


**Figure 6.30:** Comparison of the porosities in the fluidized bed and in the coarse outlet suspension with the discharge nozzle type 4.

Table 6.1 gives the experimental data of different classification experiments conducted with the discharge nozzle type IV. The pure water mass flows of the suspension S, the fines F and the coarse suspension C are given as well as the solid mass flows

(coarse:  $\dot{M}_C$ ; fines:  $F \cdot x_F$ ; feed:  $S \cdot x_S$ ). Nozzle friction coefficients for quartz  $\xi = 2.7$  and for limestone  $\xi = 5$  were determined by adaptation to the experimental data for the model proposed in chapter 5, which is also valid for the nozzles II and III. Comparing the columns of the experimentally determined solids mass flows out of the coarse discharge nozzle with the calculated data, it can be seen that the values are quite in a good agreement, so that the model can be assessed as precise enough for a first estimation of the outgoing mass flows for the nozzles used in this work.

The cut size can be calculated from the force balance on a single particle and is illustrated in figure 6.31, where cut sizes are plotted versus classifying water throughput depending on rotational velocity and density difference. The presented findings enable the selection of appropriate operating conditions as described in chapter 5.6.

Classification of Quartz											
date	rot. speed [rpm]	S [g/s]	F [g/s]	C [g/s]	$S \cdot x_S$ [g/s]	$F \cdot x_F$ [g/s]	$\dot{M}_C$ [g/s]	$u_d$ [m/s]	$u_t$ [m/s]	bed height [cm]	$\dot{M}_C$ calculated with $\xi = 2.7$
24.04.2008	399	46	286	4	10.2	6.5	3.7	0.004	0.030	1.4	4.3
28.04.2008	402	46	213	6	10.7	5.2	5.5	0.003	0.024	3.4	4.7
29.04.2008	401	46	150	7	9.8	4.2	5.6	0.002	0.018	3.6	5.0
08.05.2008	400	46	214	5	9.8	4.9	4.9	0.003	0.021	2.8	4.5
21.05.2008	600	46	210	10	10.0	3.4	6.5	0.003	0.035	2.2	7.6
23.05.2008	700	46	203	17	10.9	3.0	7.9	0.003	0.035	1.8	8.8
Classification of Limestone											
date	rot. speed [rpm]	S [g/s]	F [g/s]	C [g/s]	$S \cdot x_S$ [g/s]	$F \cdot x_F$ [g/s]	$\dot{M}_C$ [g/s]	$u_d$ [m/s]	$u_t$ [m/s]	bed height [cm]	$\dot{M}_C$ calculated with $\xi = 5$
15.04.2008	405	48	289	3	6.2	3.7	2.5	0.004	0.030	2	2.7
08.10.2008	675	47	201	12	7.4	2	5.2	0.003	0.032	3	5.2

**Table 6.1:** Comparison between calculated and experimentally determined mass flow through the coarse discharge nozzle type IV

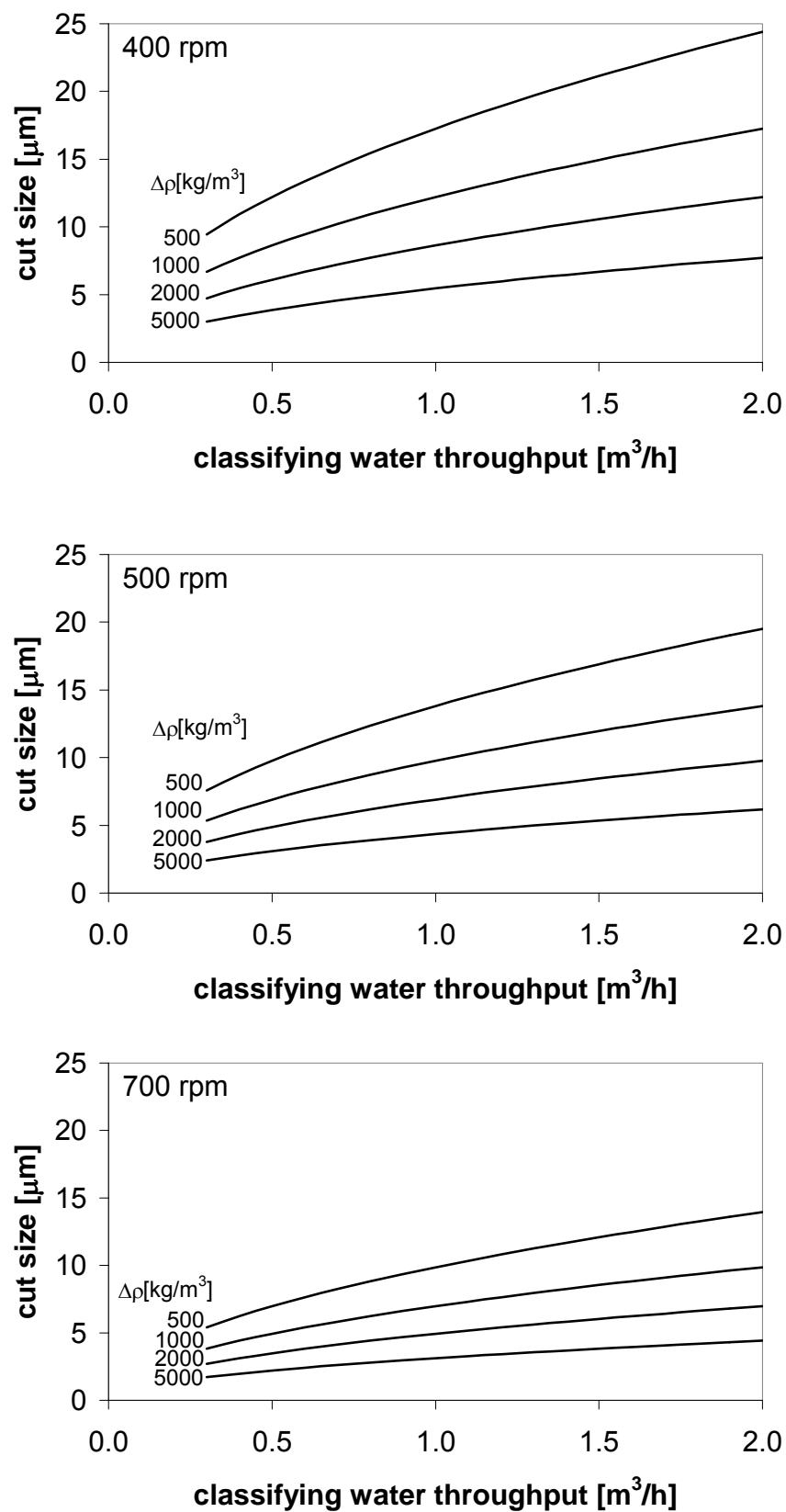


**Figure 6.31:** Cut sizes calculated from a force balance on the single sphere depending on the operating conditions

### 6.7 Classification experiments with the optimized coarse discharge

Because of poor separation performance the coarse discharge type 1 was replaced by the coarse discharge nozzle, in the first case (type II) an outlet pipe with a diameter of 1 mm located 1.3 cm above the distributor (cf. figure 5.7). The experiment (13.10.2006) with the new coarse discharge was operated at similar conditions (400 rpm, 3 g/s solid feed rate) as with type I. The classification experiment (figure 6.32) revealed a strong fishhook and a misclassification of coarse particles. For clarification a closer look into bed build up was taken. Figure 6.33 shows the development of the bed height during the experiment. In the first minutes the bed height was increasing until it was approaching the coarse discharge. Reaching the height of the coarse discharge the bed height remains constant. This indicates that the coarse discharge nozzle was not completely submerged in the fluidized bed. To further support this conclusion the coarse discharge flow was estimated with the help of equation (5.55) with a bed height of 1.5 cm and a pressure drop coefficient  $\xi = 2.7$ . With a calculated solid mass flow of  $\dot{M}_C = 3.1$  g/s through the discharge nozzle, the calculated value exceeds the measured one significantly. The calculated one is based on the assumption of a completely submerged discharge, which is obviously not fulfilled in this case. In other words, a mass flow of  $\dot{M}_C = 3.1$  g/s into the fluidized bed would be necessary for the given conditions to keep the bed height at a minimal level above the coarse discharge. If the real flow is lower, the coarse discharge penetrates into the freeboard and a bypass of fines and vortices in the freeboard occur as with the coarse discharge type 1 (chapter 6.5) resulting in an insufficient classification efficiency. A cut size of  $d_C = 9 \mu\text{m}$  and a coarse fraction  $c = 0.52$  was measured for this configuration.

With an increase of the mass flow into the bed by an increase of the solids concentration in the suspension feed a submerged coarse discharge can be assured. In the classification experiment (21.9.2006) shown in figure 6.34, conducted at 400 rpm and 0.0033 m/s fluidizing velocity, a mass flow of 4.3 g/s into



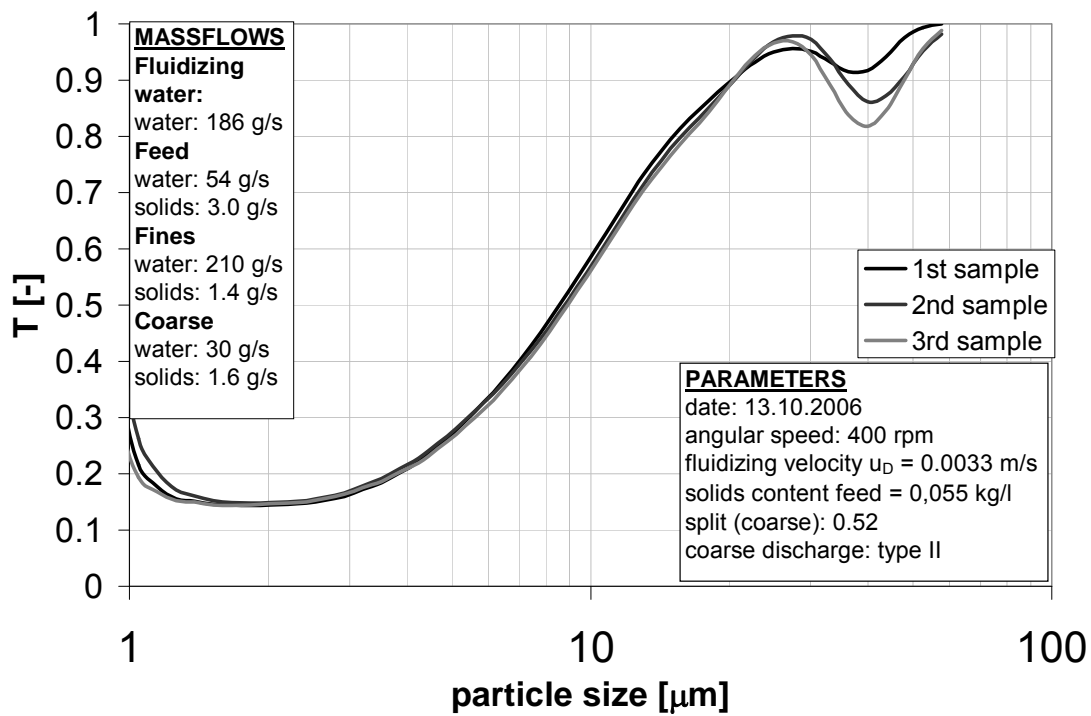


**Figure 6.32:** Separation efficiency curve of quartz classification operated with coarse discharge nozzle (type II)

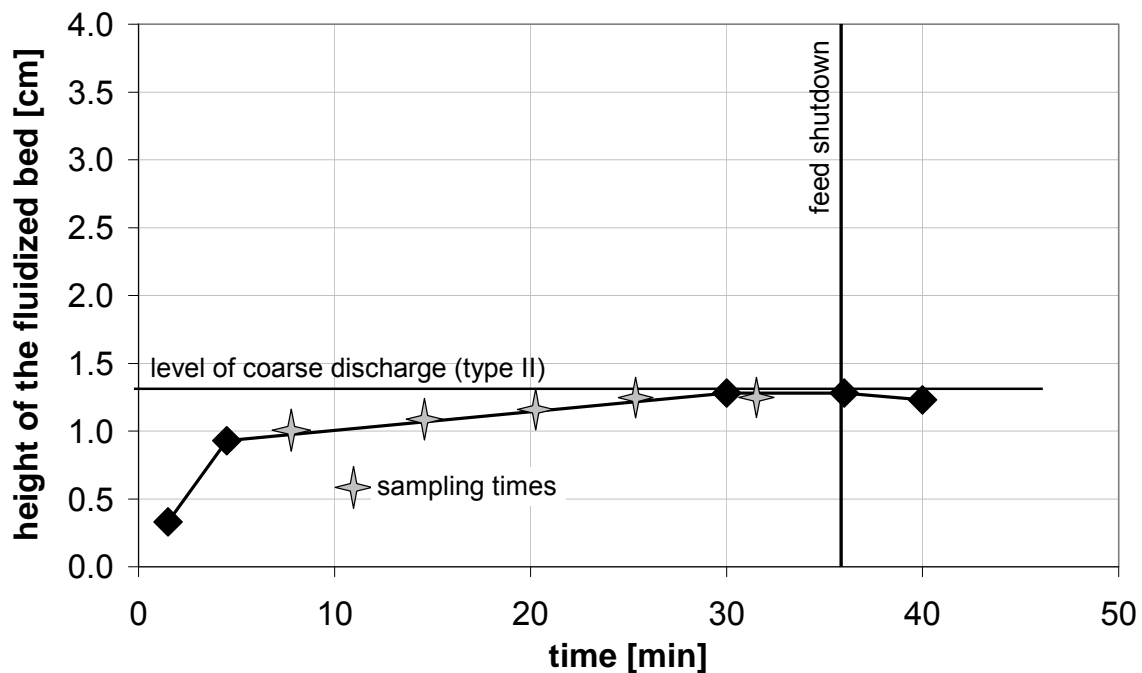


**Figure 6.33:** Bed height diagram of quartz classification (13.10.2006)

the fluidized bed was reached. The submersion of the coarse discharge increases the separation performance significantly. The misclassification of the coarse particles indicated by a local minimum at  $40\text{ }\mu\text{m}$  in figure 6.32 was vanished and the fishhook effect eliminated. The slope of the separation efficiency curve was strongly increased, which indicates a sharp separation. After the definition of Eder a sharpness  $\kappa = 0.63$  is reached, what lies in the range of industrial sharp separations. In the fines region just a small amount particles have been misclassified, what is in the range of acceptance for industrial application. In this case the coarse fraction  $c = 0.45$  is reduced compared to the previous experiment as less fines are been misclassified. The reduction of the coarse fraction increases the cut size to  $12\text{ }\mu\text{m}$ .

It has to be noted that the separation efficiency curves of the 4 samples taken at different times are almost identical, so that stationary conditions were prevailing. The times of sampling can be taken out of the bed height diagram (figure 6.35).

In this experiment a constant bed height of approximately  $1.2\text{ cm}$  above the coarse discharge is achieved after 18 minutes, i.e. an equilibrium between the solid mass flows into the bed and out of the coarse discharge is reached. After shutdown of the suspension feed after 42 minutes of classification the bed height is quickly reduced to the level of the coarse discharge. The calculation of the coarse discharge flow leads to a solids mass flow of  $\dot{M}_c = 4.5\text{ g/s}$ , what is in a good agreement with the experimental value of  $4.3\text{ g/s}$ .

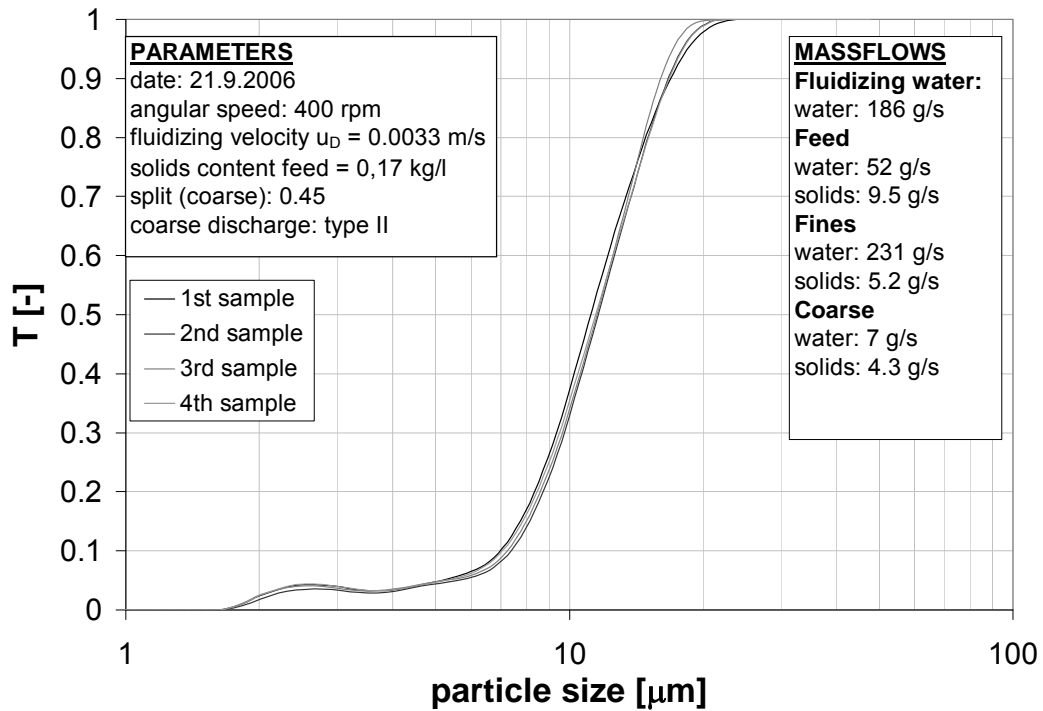


**Figure 6.34:** Separation efficiency curve of quartz classification operated with coarse discharge nozzle type II (21.9.2006)

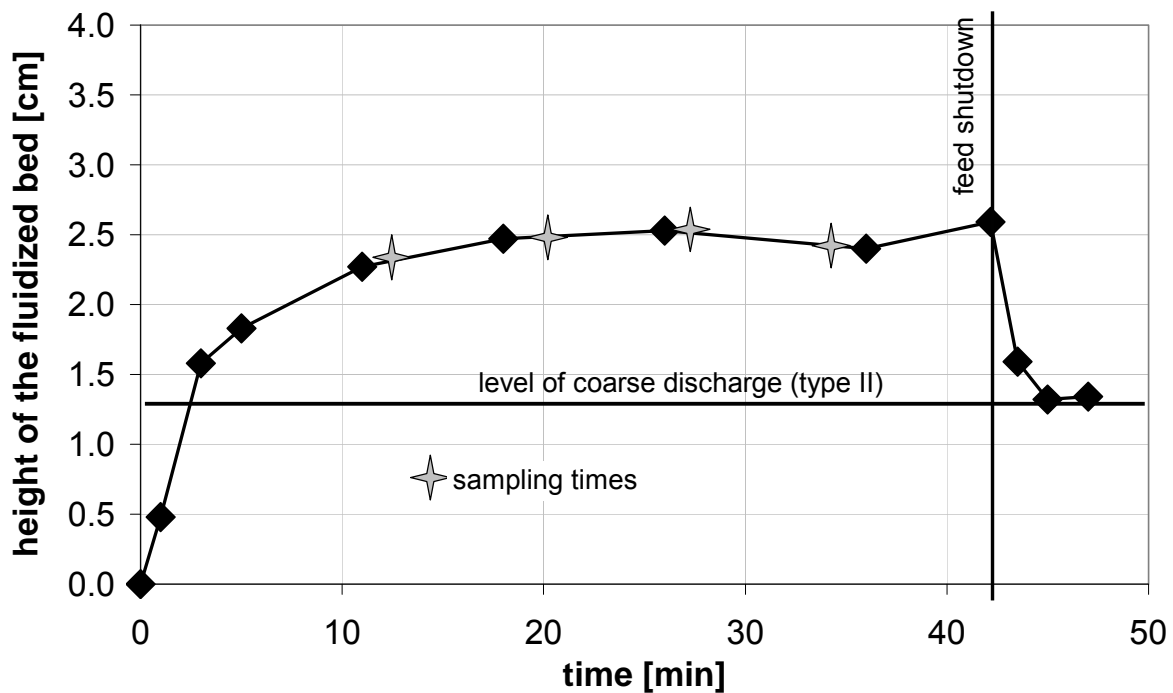


**Figure 6.35:** Bed height diagram of quartz classification (21.9.2006)

### 6.8 Classification experiments with the coarse discharge nozzle type III

The replacement of the coarse discharge mechanism (type I) by the discharge nozzle type II brought an improvement of the control of the outgoing currents, a realization of a constant bed height and of course an increase of the separation performance. The discharge nozzle type II was not penetrating into the bed, but was arranged in the side wall of the classification chamber. To analyze the influence of the location of the discharge nozzle, it was brought into the center of the classification chamber (nozzle type III) and classification experiments were performed. Figure 6.36 shows the results of the classification experiment (19.3.2008) under comparable conditions as the experiment with the discharge nozzle II (21.9.2006). The bed height diagram is pictured in figure 6.37. The 4 samples taken at different times, when a constant bed height was reached, show a small deviation, what lies in the range of experimental precision. The average cut size  $d_c = 11 \mu\text{m}$  is comparable with the classification with nozzle II. The sharpness  $\kappa = 0.58$  as well as the bed height is below the ones of the experiment from the 21.9.2006. It is not clear if the lower sharpness is due to the arrangement of the discharge nozzle, which might disturb the flow or has it to be contributed to the influence of the bed height, what will be discussed later.

The constancy of the bed height at a lower level for the coarse discharge nozzle III can be explained by a difference of the fluidization in the center compared to the wall. In the center a well fluidized bed can be assumed, while at the wall the flow is reduced by wall friction, resulting in a lower porosity at the wall compared to the center. Thus the apparent viscosity in the center is lower than at the wall, what eases the outflow in the center. Therefore a lower bed height is adjusted. However, an increase of the separation efficiency is not achieved by this configuration compared to nozzle II, so that nozzle III was not investigated further.

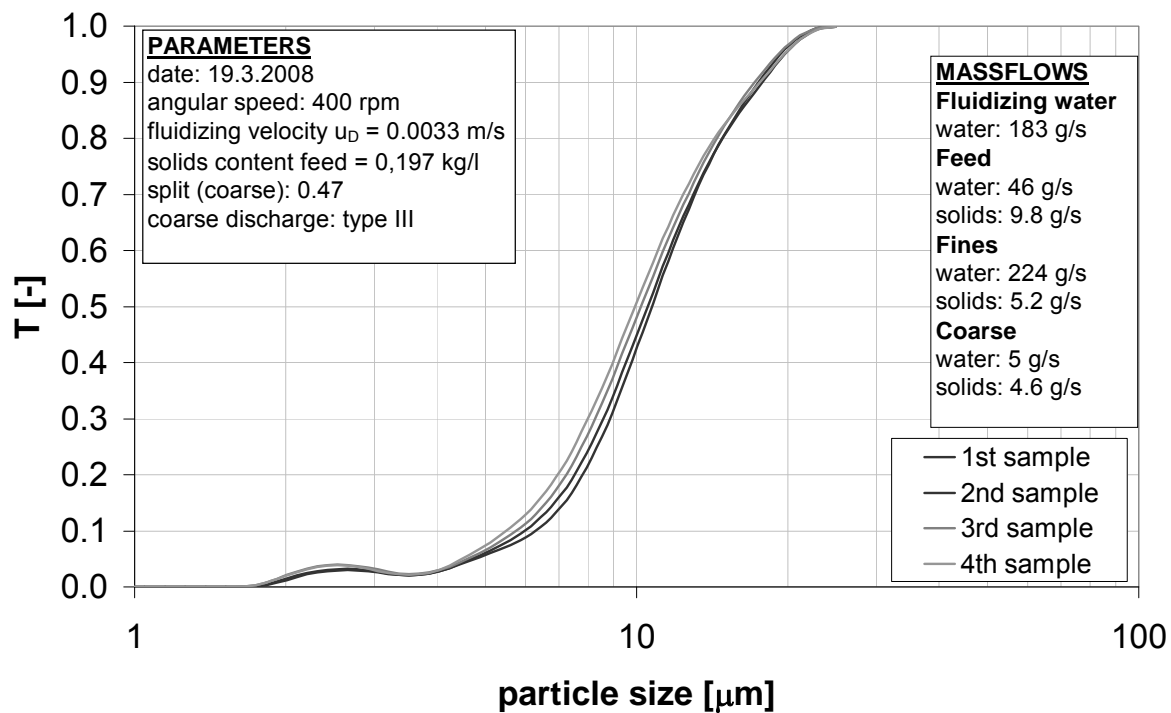


**Figure 6.36:** Separation efficiency curve of quartz classification operated with coarse discharge nozzle type III (19.3.2008)

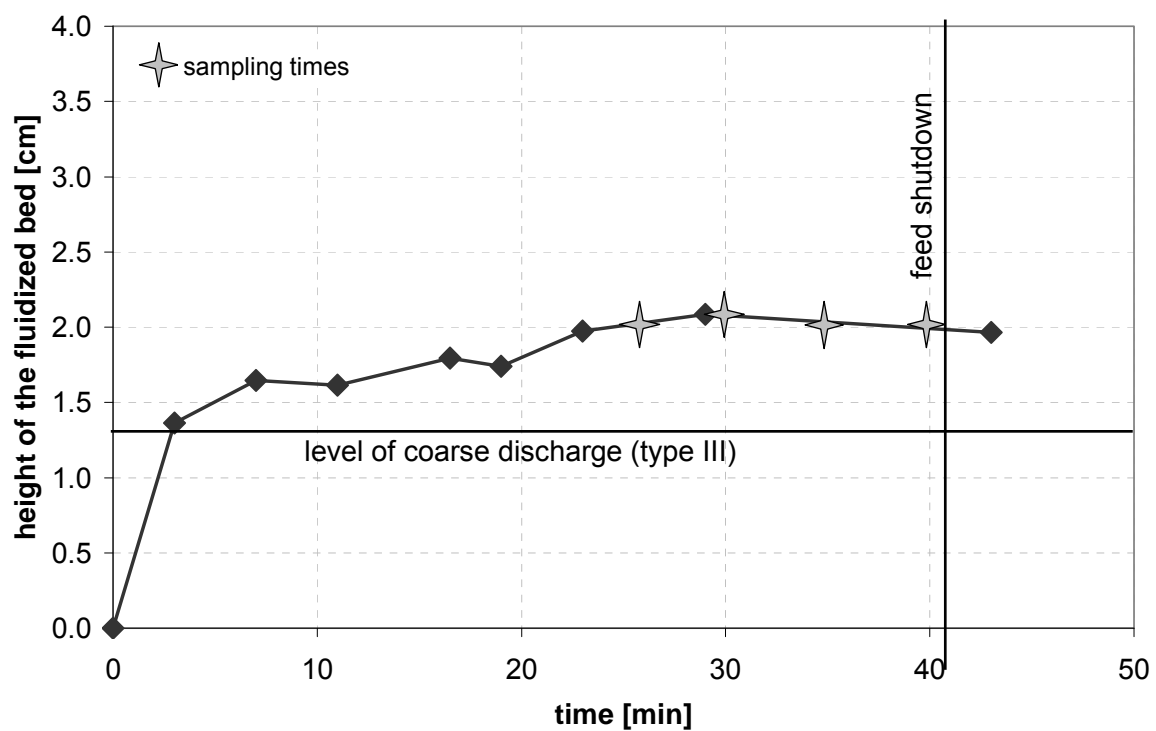


**Figure 6.37:** Bed height diagram of quartz classification (19.3.2008)

### 6.9 Classification with the coarse discharge nozzle type IV

To study the influence of the position of the outlet orifice, coarse discharge IV was developed. The nozzle is arranged such that the orifice is facing the distributor at a distance of 5 mm. The orifice nozzle is connected to the outlet transport pipe at a 90° angle (cf. figure 5.7). The design of coarse discharge IV enhances the distance from the bed surface to the outlet, what should make it more difficult for the fines to be misclassified. With the discharge nozzle IV the influence of the bed height, the suspension feed concentration and the cut size on the separation efficiency were investigated. As mentioned above classification is only recommended above  $1.5 \times u_{mf}$  and therefore the presented results were conducted in the range  $1.5 \times u_{mf} < u < 4 \times u_{mf}$ . When performing classifications with coarse discharge nozzle IV it was always assured that the nozzle was completely covered by the bed to avoid bypass of fines.

Figure 6.38 shows the classification with the nozzle IV (24.4.2008) for a cut size of  $d_c = 13 \mu\text{m}$  at 400 rpm and with a fluidizing velocity of  $u_D = 2.1 \times u_{mf}$ . A high separation sharpness of  $d_{p,25}/d_{p,75} = 0.62$  was achieved. The amount of fines below  $8 \mu\text{m}$  been misclassified is smaller compared to the experiments with other coarse discharges, i.e. the coarse fraction contains only a very tiny amount of fines, while the fines fraction is completely devoid of particles larger than  $23 \mu\text{m}$ . However the sharpness is comparable with the result obtained with nozzle II (21.9.2006). The separation efficiency curves of 5 taken samples are presented in figure 6.38 and all of them show a very small deviation from the others, so that stationary conditions can be assumed. Also the bed height as shown in figure 6.39 stays almost constant after 25 minutes, so that an equilibrium between particles entering the bed from the coarse fraction of the suspension feed and leaving the bed through the nozzle was reached. The bed height was adjusted between 1.3 to 1.4 cm above the distributor or 0.8 to 0.9 cm above the nozzle orifice.

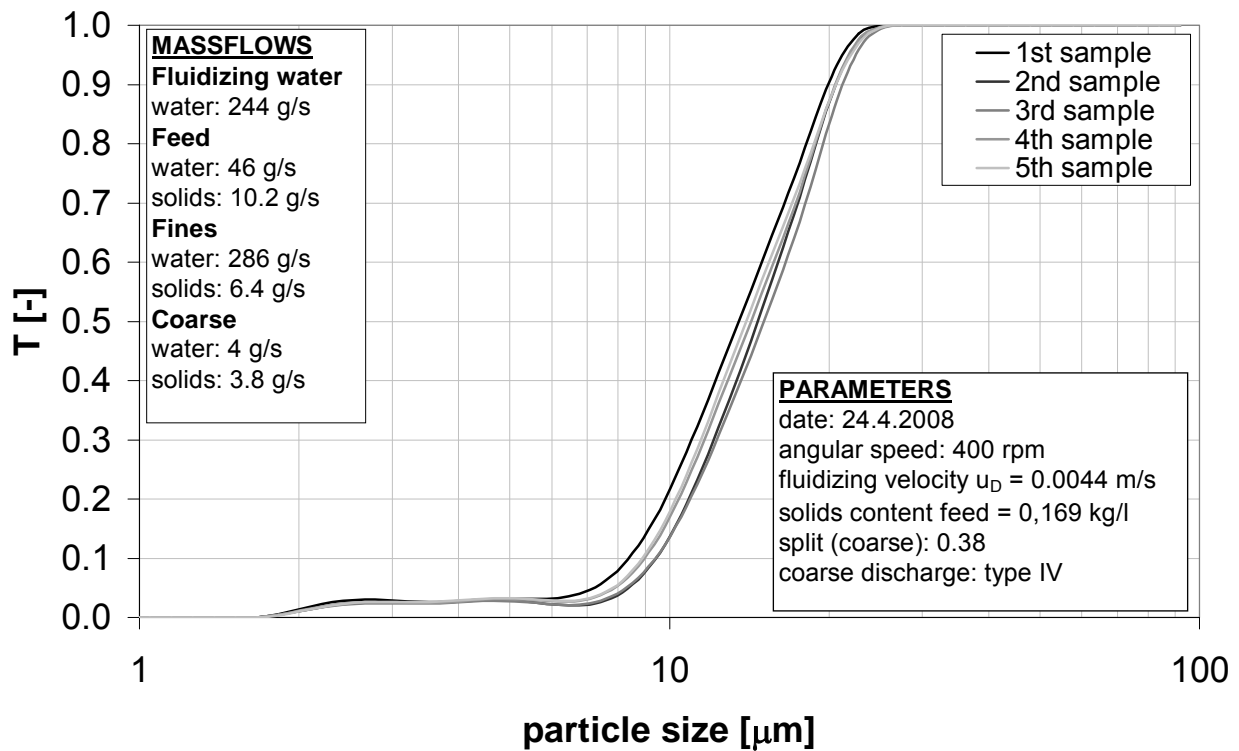


**Figure 6.38:** Separation efficiency curve of quartz classification operated with coarse discharge nozzle type IV (24.4.2008)

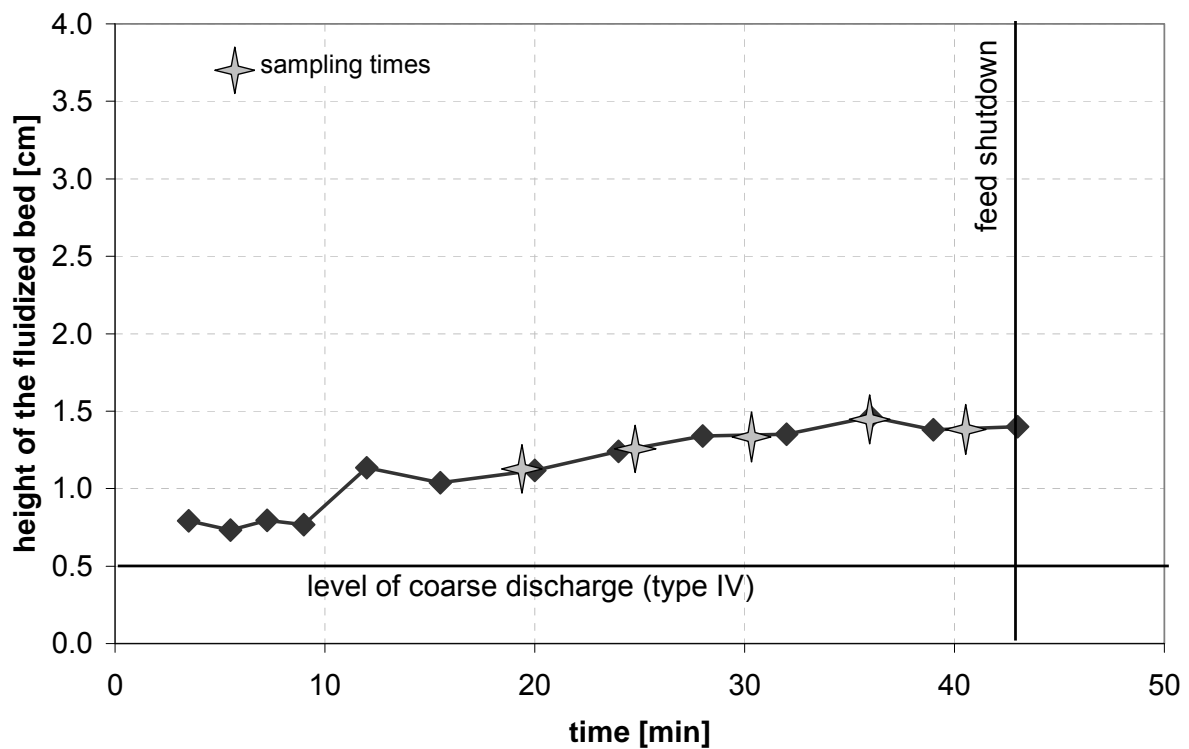


**Figure 6.39:** Bed height diagram of quartz classification (24.4.2008)

### 6.9.1 Influence of the bed height

As coverage of the discharge nozzle by the fluidized bed is essential for the classification, the question arises how the bed height influences the classification performance even when the nozzle is covered. For that reason a classification was carried out with increasing bed height (28.4.2008), the results are depicted in figure 6.40. With increasing bed height the experiment becomes instationary, i.e. particles were accumulated in the bed. For the calculation of the mass flows for the determination of the separation efficiency curve the equations (5.64 – 5.65) were employed, taking the accumulation of the particles in the bed into account. The accumulation was determined by the change of the bed height. The build up of the bed was conducted with comparable conditions as in the experiment of the 24.4.2008, but with a fluidizing velocity of 0.0031 m/s. Due to this more particles are classified to the coarse fraction. The consequence is that more particles report to the fluidized bed than the outlet nozzle can handle for bed heights below 4 cm above the distributor. Thus the bed height increases due to accumulation of particles. The separation efficiency and the corresponding development of the bed height of the described experiment are presented in the figures 6.40 and 6.41. The bed height increases as expected to a level above the suspension feed port and samples were taken when an approximately constant increase of the solids mass of 0.9 g/s took place. The bed heights of samples 1 and 2 were below the 4 feed ports, which have diameters of 0.5 cm and the centers are located 3.25 cm above the distributor. For the samples 3 and 4 the bed heights reached the positions of the feed ports, so that it can be assumed that the complete suspension feed was injected to the fluidized bed. For the understanding of the classification it is interesting to know how this influences the classification. From figure 6.40 it can be seen that with increasing bed height the separation efficiency curves are shifted to coarser diameters. The sharpness of the classification increases significantly from  $\kappa = 0.57$  at a bed height of  $H_B = 2.4$  cm to  $\kappa = 0.67$  at  $H_B = 3.2$  cm.



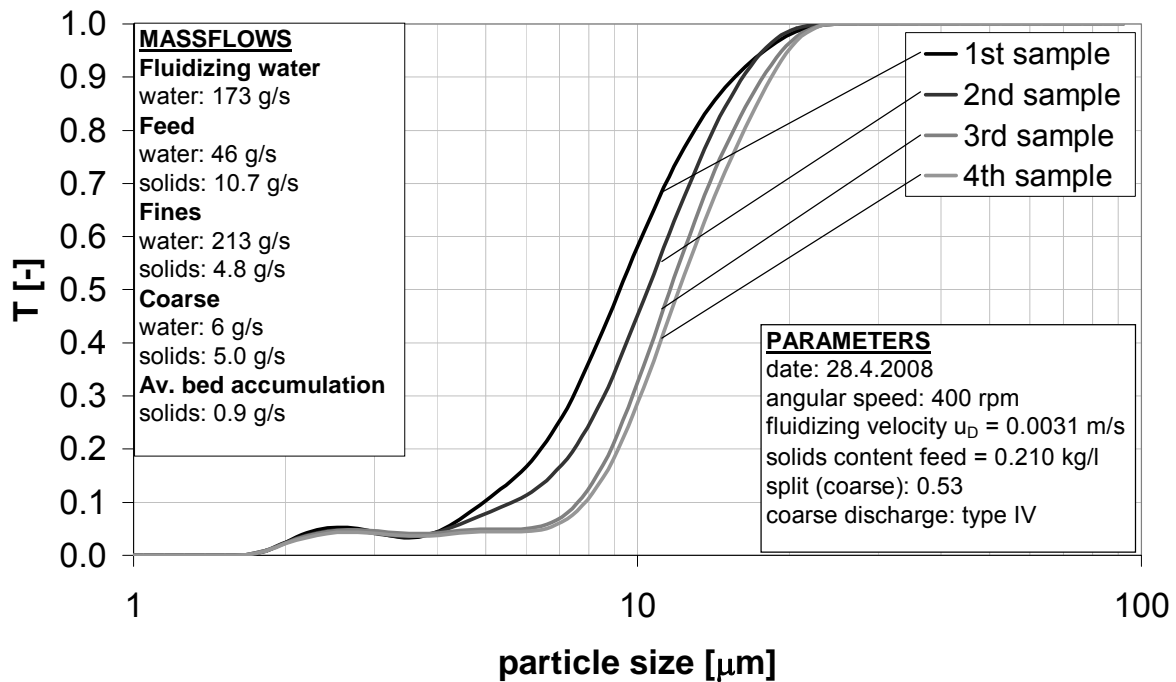


**Figure 6.40:** Separation efficiency curve of quartz classification depending on the bed height (28.4.2008)

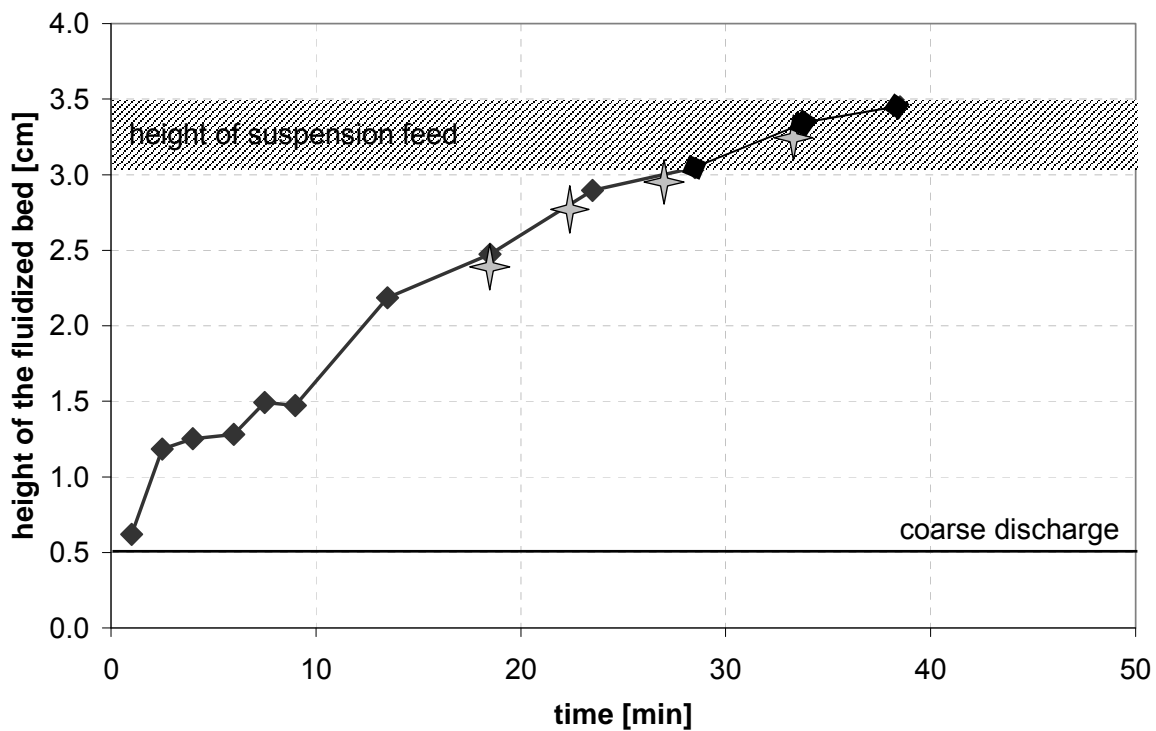


**Figure 6.41:** Bed height diagram of quartz classification (28.4.2008)

The cut size was shifted from  $d_c = 9 \mu\text{m}$  to  $11 \mu\text{m}$ , for the samples 3 and 4 both the cut sizes and the sharpness stay almost the same. It can therefore be concluded that increasing the bed height increases the slope of the separation efficiency curve, while shifting the cut size to higher particle diameters.

This experiment provides also a deeper insight into the classification process. As the bed height reaches the position of the feed ports, the whole suspension containing fines and coarse particles is introduced into the fluidized bed, i.e. the fines cannot be separated in the freeboard. In a gas fluidized bed an almost complete mixing of particles inside the bed would be observed, which, however, cannot be the case for wet centrifugal classification, because a sharp classification was achieved even when the whole suspension flow is introduced into the bed. On the contrary the amount of fines reported to the nozzle was reduced with increasing bed height, which can only be explained by a strong segregation above the height of the fluidized bed. In case of the bed height reaching to the feed ports (sample 4) a particle size distribution of the raw material can be assumed at the bed surface, which changes along the bed height down to the nozzle to final coarse particle size distribution.

The influence of the bed height was also studied for the classification of cut sizes below  $10 \mu\text{m}$ . Figure 6.42 pictures the classification experiment (29.4.2008), where the bed height was increased from 1 to 4 cm above the distributor. With a fluidizing velocity of  $u_D = 0.002 \text{ m/s}$  the coarse discharge was not capable to completely discharge the coarse fraction, so that the fluidized bed was built up. The fluidizing velocity, which equals approximately 1.5 times the minimum fluidizing velocity ( $u_D = 1.5 \times u_{mf}$ ) is in the range of recommendation. The separation performance is technically sharp for all samples taken and ranges between  $\kappa = 0.52$  at the low bed height of  $H_B = 1 \text{ cm}$  to  $\kappa = 0.67$  at a bed height of  $H_B = 4 \text{ cm}$ . Cut sizes between 6 and  $10 \mu\text{m}$  were achieved. At the highest bed height the suspension is injected directly into

the fluidized bed and the cut size as well as the sharpness is the highest, what confirms the findings presented above.

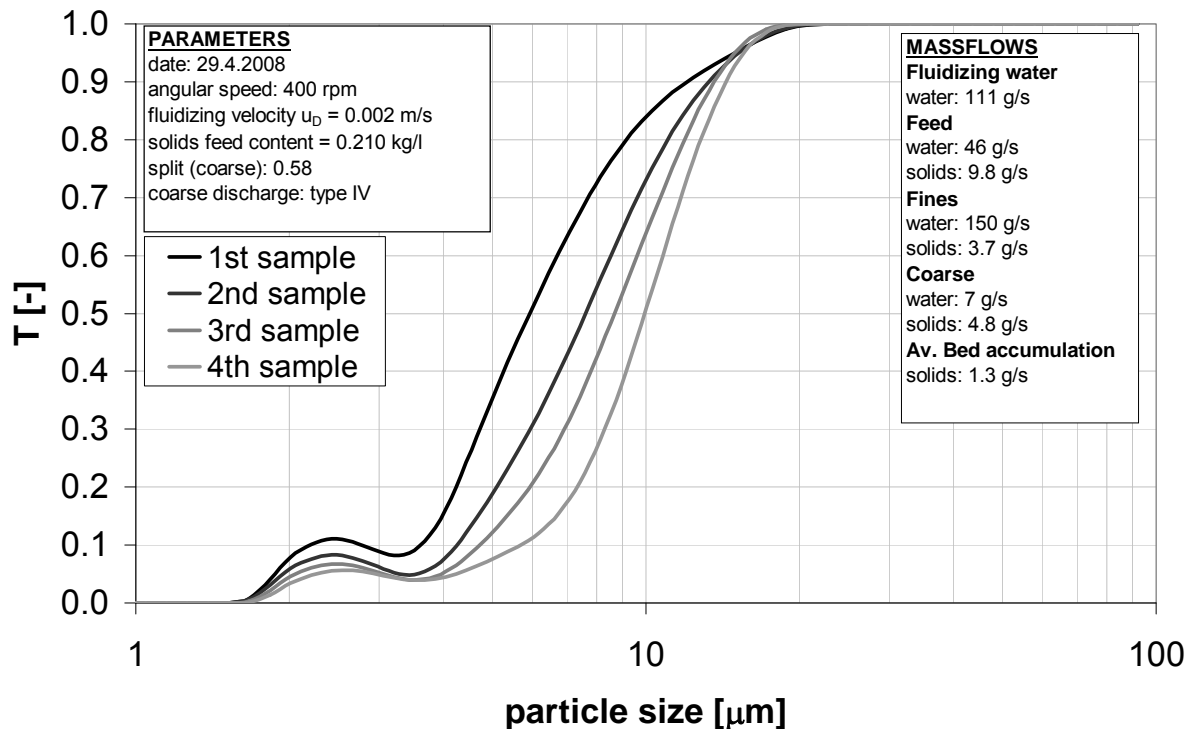


**Figure 6.42:** Separation efficiency curve of quartz classification depending on the bed height with cut sizes below 10  $\mu\text{m}$  (29.4.2008)

### 6.9.2 Effect of the number of feed ports on the classification with nozzle IV

Due to a strong tangential flow in the freeboard induced by the Coriolis force, the injected suspension feed is immediately distributed circumferentially in classification chamber. It can be expected that this will also happen when the four feed ports are replaced by only one. In this case the injected flow through the single port is four times higher than in the four feed ports. Considering only a single feed port is a simplification for the design, which is advantageous for industrial usage. For that reason an experiment was conducted with only one active feed port (8.5.2006). Figure 6.43 shows the setup. On top the configuration with the four open ports and the single coarse discharge as used before is presented. At the bottom only one feed and one

coarse discharge nozzle is visible. As the bed and the freeboard moves tangentially in the direction of rotation the injected particles are expected to follow the flow inside the classifier. For that reason the open feed port is located shortly behind the coarse discharge nozzle to enhance the minimum traveling distance of a single particle, i.e. a particle has at least to perform an almost complete rotation before it can report to coarse discharge nozzle. The intention is the reduction of misclassification of fines by enhancing the minimum tracking distance.

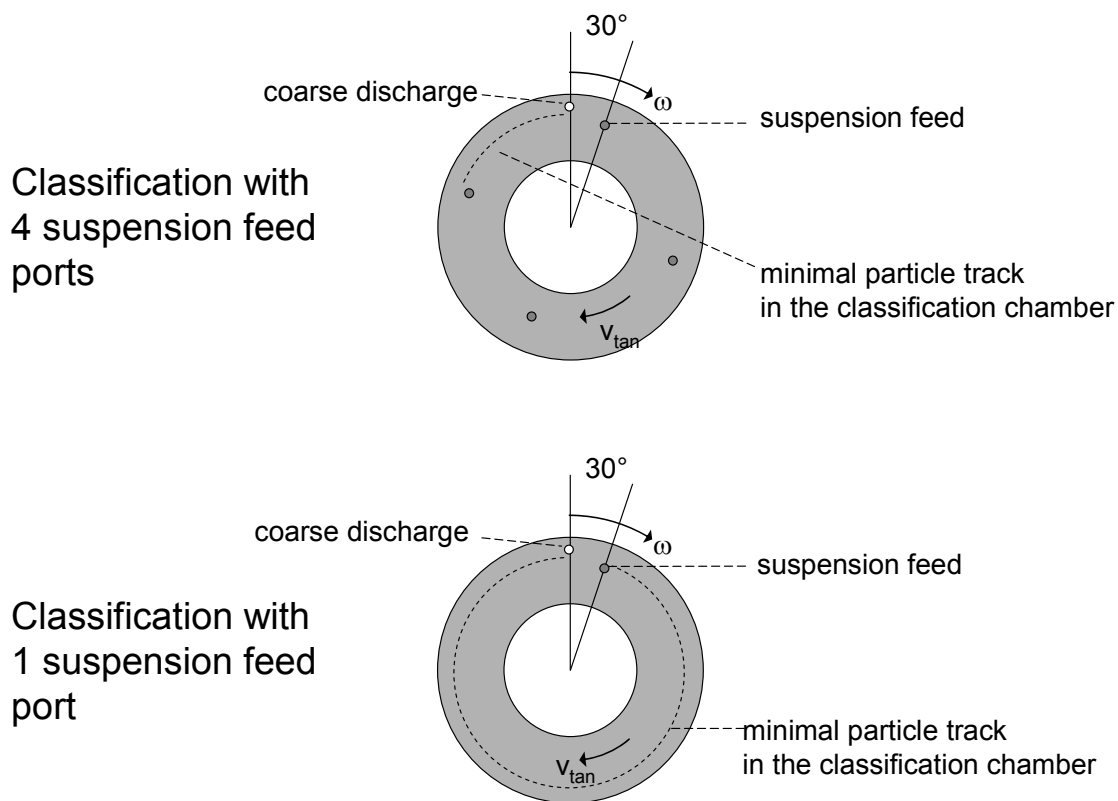


**Figure 6.43:** Classification with only one suspension feed port

To study the influence of the bed height in this configuration, similar conditions were chosen as in the experiment at the 28.4.2008. Quartz particles were injected to the single feed port at 400 rpm and fluidized at 3.1 mm/s. 47 % of the solids feed were classified to the fines and 45 % to the coarse fraction. An average of 8 % of the solids

feed was accumulated in the fluidized bed, where at the beginning the accumulation was stronger than at the end of the experiment. The build up of the fluidized bed is shown in figure 6.44. The samples were taken at different bed heights for further clarification of the influence of the bed height on the separation efficiency.

The separation efficiency curves are shown in figure 6.45. Different cut sizes were achieved, ranging from 9 to 12  $\mu\text{m}$  depending on the bed height, which was increased from 1.5 cm to 3 cm above the distributor. With increasing bed height, the separation efficiency curve was shifted to the coarse region with achieving higher separation sharpness  $\kappa$ . The range of the separation sharpness is between  $0.55 < \kappa < 0.68$ , which can be classified as technically sharp separation. The amount of fines is for all cases very small, however a minimum of misclassified particles can be found in the sample of the largest bed height.

These findings are confirming the results of the previous experiment conducted at the 28.4.2009. Also the separation sharpness and the cut size for this case are comparable, what indicates that the injection of the suspension by one single feed port is sufficient and a higher number of feed ports is overrated. However, the following classification experiments were conducted with four active feed ports.

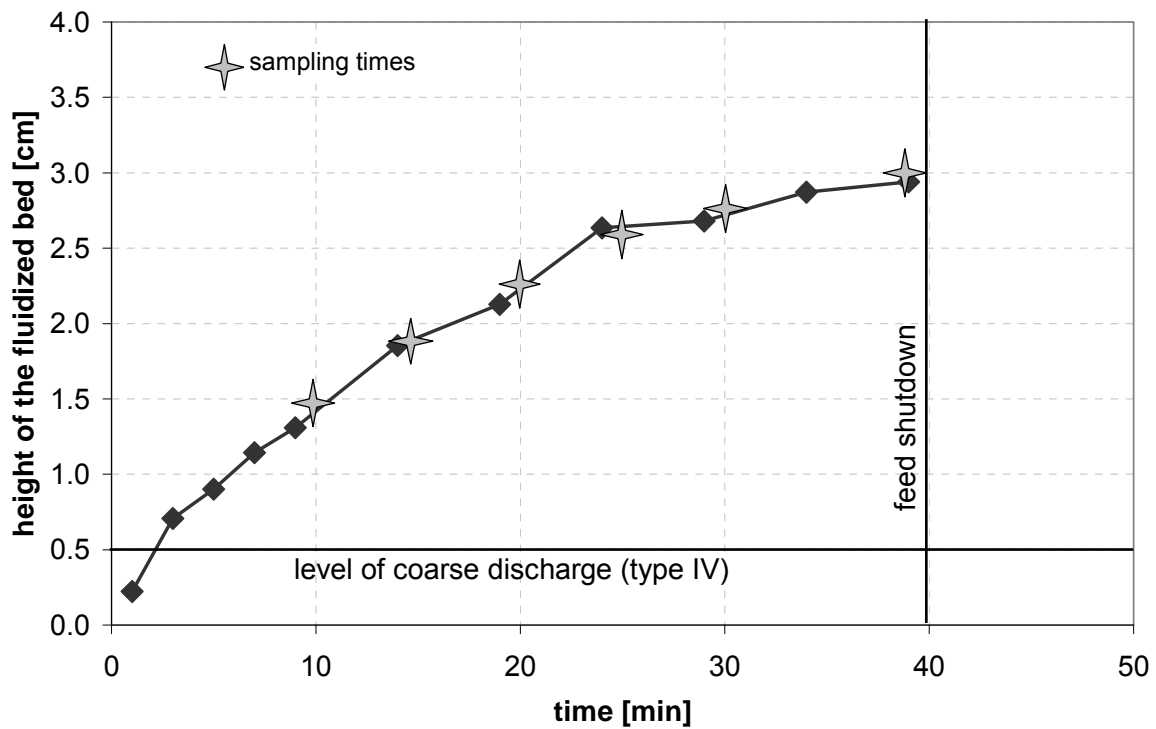


**Figure 6.44:** Bed height diagram of quartz classification (8.5.2008)

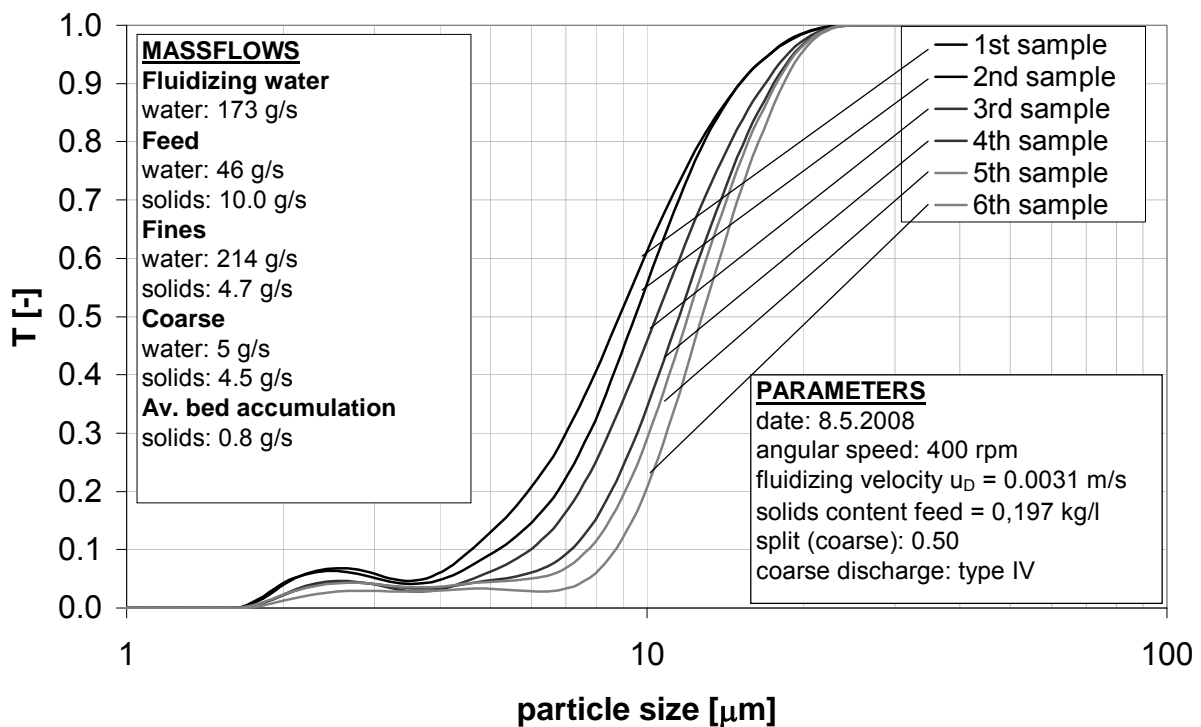


**Figure 6.45:** Separation efficiency curve of quartz classification depending on the bed height with only one suspension feed open (8.5.2008)

### 6.9.3 Classification of limestone

Limestone is like quartz a natural product, which is therefore irregular shaped. Although the density ( $\rho_{Li} = 2620 \text{ kg/m}^3$ ) and the particle size distribution of the used limestone is similar to quartz, the fluidized bed expansion behavior differs significantly from quartz (Margraf and Werther, 2008). The investigation of the feasibility of the classification of limestone with the optimized coarse discharge is therefore of big interest. In figure 6.46 the result of limestone classification of 10<sup>th</sup> April is presented. A high fluidized bed was achieved, whose height reached constancy at 3.9 cm above the distributor at the end of the sampling period. The coarse discharge as well as the suspension feed ports were submerged by the fluidized bed. This applies to all taken samples during the sampling period, in which the bed height was increased from 3.2 cm to its final and stationary height of 3.9 cm. For all samples a very sharp separation performance with  $\kappa = 0.77$  was achieved, which confirms the finding that a high fluidized bed is favorable for the classification. Also for limestone a strong segregation in the bed from the submerged coarse discharge to the submerged feed ports can be assumed. At 400 rpm with a fluidizing velocity of 4.4 mm/s cut sizes between 16 and 18  $\mu\text{m}$  depending on the bed height were achieved. With limestone a slight increase of the cut size can be observed with increasing bed height. This behavior is similar to the one observed with quartz. The bed height reached higher values at similar conditions compared to quartz due to a higher bed voidage, which was investigated by Margraf and Werther (2008).

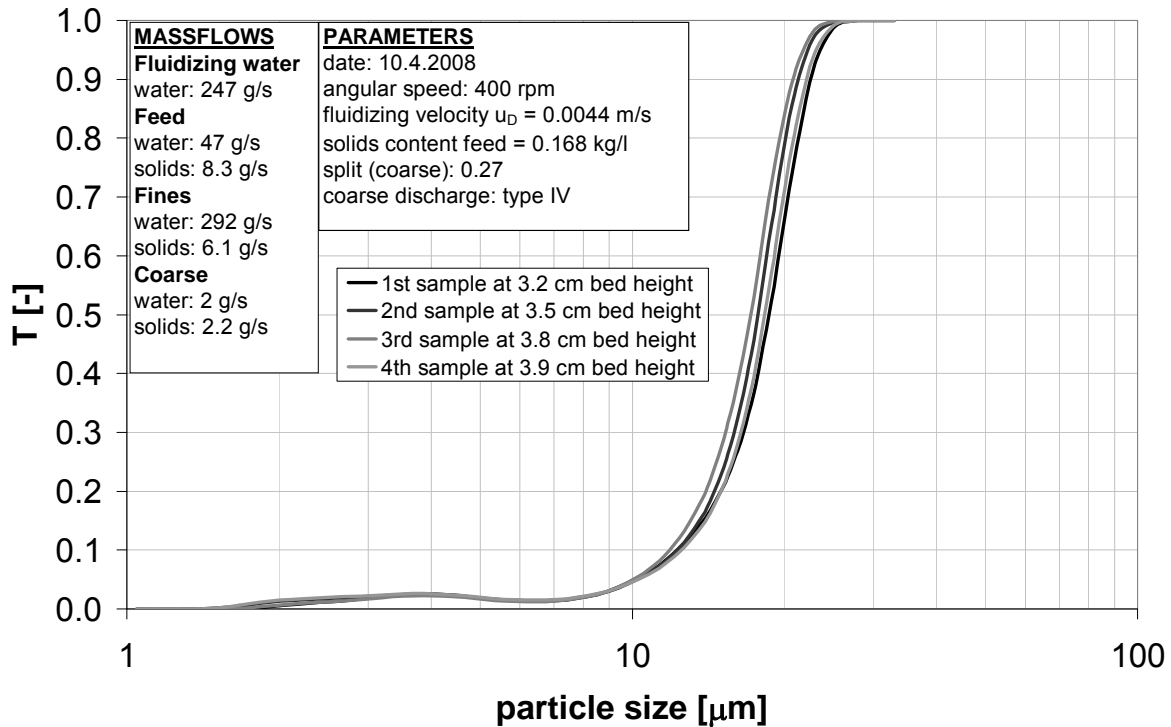


**Figure 6.46:** Separation efficiency curve of limestone classification with a cut size of about 20  $\mu\text{m}$  (10.4.2008)

#### 6.9.4 Classification of quartz for cut sizes between 1 and 10 $\mu\text{m}$

With increasing angular velocities above 600 rpm cut sizes far below 10  $\mu\text{m}$  can be achieved. As quartz powder ranges from 1 to 60  $\mu\text{m}$  with only mass-20 % below 4  $\mu\text{m}$ , classifications below 4  $\mu\text{m}$  are not recommendable for this material. Furthermore at lower cut sizes the stable fluidization of the larger particles cannot be assured. Therefore classification experiments with cut sizes of approximately 6 and 4.7  $\mu\text{m}$  were carried out. It should be mentioned that particle collectives containing submicron particles can be classified at cut sizes down to 1  $\mu\text{m}$  and below, when the classification is not disturbed by defluidized zones due to the presence of too large particles.



The separation efficiency curves of figure 6.47 are showing the classification results at 600 rpm for a cut sizes at approximately 6  $\mu\text{m}$ . The curves are corresponding to samples, taken in a time range of 30 minutes at a constant bed height of 2.2 cm. The deviations of the cut sizes and the shapes of the curves are very small, so that stationary conditions can be assumed. With  $\kappa = 0.5$  a technically sharp classification was achieved. A similar result gives the classification experiment conducted at 700 rpm and at a cut size of 4.7  $\mu\text{m}$  (figure 6.48). Stationary conditions were achieved when the bed height reaches 1.8 cm and samples were taken over 20 minutes of operation. A sharpness of  $\kappa = 0.51$  was reached which is comparable to the one presented above. The performance of the classification in the range of cut sizes below 10  $\mu\text{m}$  is still technically sharp and no fishhook effect can be observed.

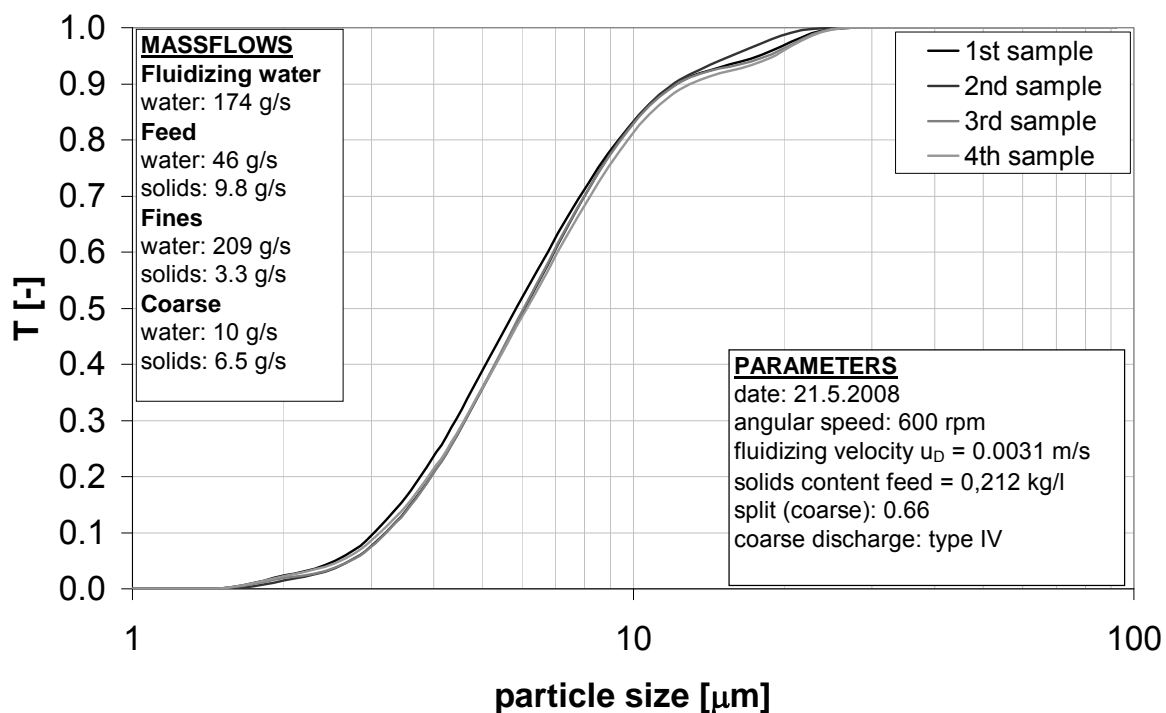


**Figure 6.47:** Separation efficiency curve of fine quartz classification at a constant bed height of 2.2 cm (21.5.2008)

However, the sharpness of the classification is smaller compared to cut sizes above 10  $\mu\text{m}$ . An explanation is that with decreasing cut sizes the range of particle diameters

in the fluidized bed is increased, which may lead to an onset of defluidized zones in the bed. These instabilities may contribute to a decrease in the classification performance.

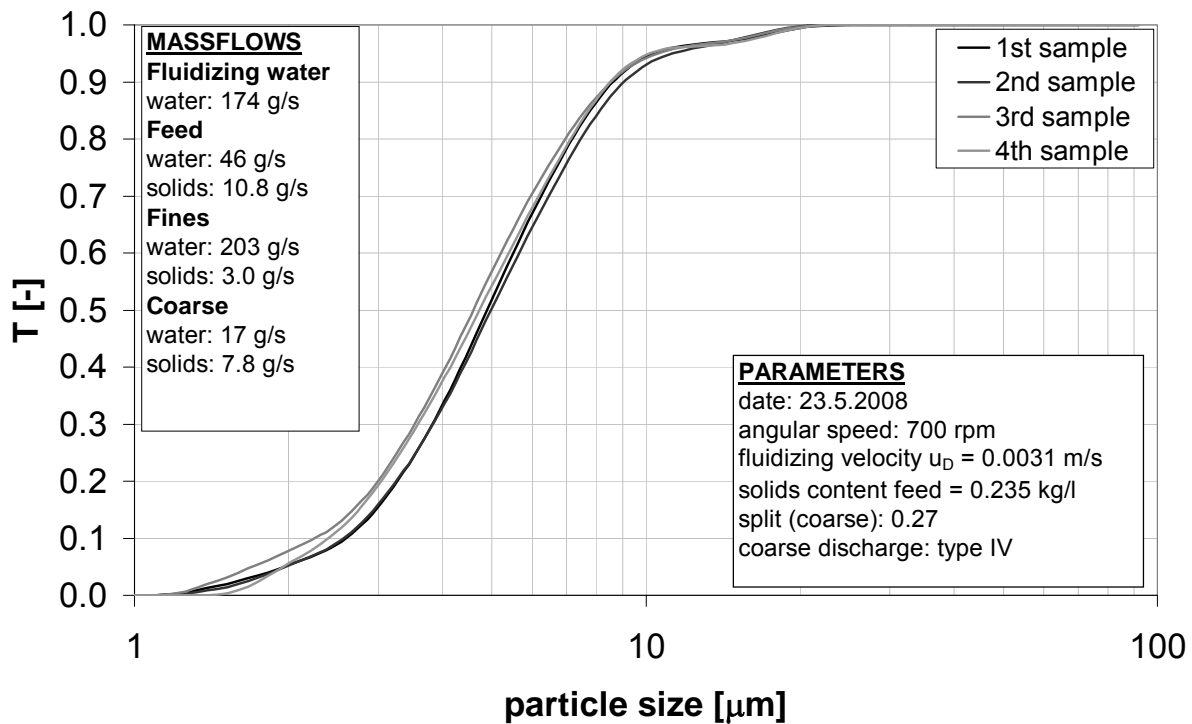


**Figure 6.48:** Separation efficiency curve of fine quartz classification at a constant bed height of 1.8 cm (23.5.2008)

### 6.9.5 Classification of glass beads

Finally the influence of the particle shape was investigated. Therefore the separation efficiency of a classification of spherical shaped particles (glass beads, cf. figure 5.1 and 5.2) was determined.

As only 10-mass% of the glass beads are below 20  $\mu\text{m}$ , cut sizes above 20  $\mu\text{m}$  are necessary to obtain reasonable results. The classification experiment presented in figure 6.49 shows a cut size of 21  $\mu\text{m}$ . With a coarse fraction of  $c = 0.85$  only 15% of

the raw material was elutriated to the overflow. For the classification a rotational speed of 185 rpm was adjusted with a fluidizing velocity of 2.8 mm/s at the distributor. The bed reached after 10 minutes a stationary height of 1.9 cm and samples were taken. It can be seen that a high slope of the separation efficiency curve was achieved. A sharpness of  $\kappa = 0.91$  was achieved and no fishhook effect can be observed. This high separation efficiency can be explained by a very smooth fluidization of a bed with a very narrow particle size distribution. Furthermore the spherical shape of the glass particle gives ideal conditions for fluidization and for the transport to the coarse and fines discharge. Thus an almost ideal classification was achieved.

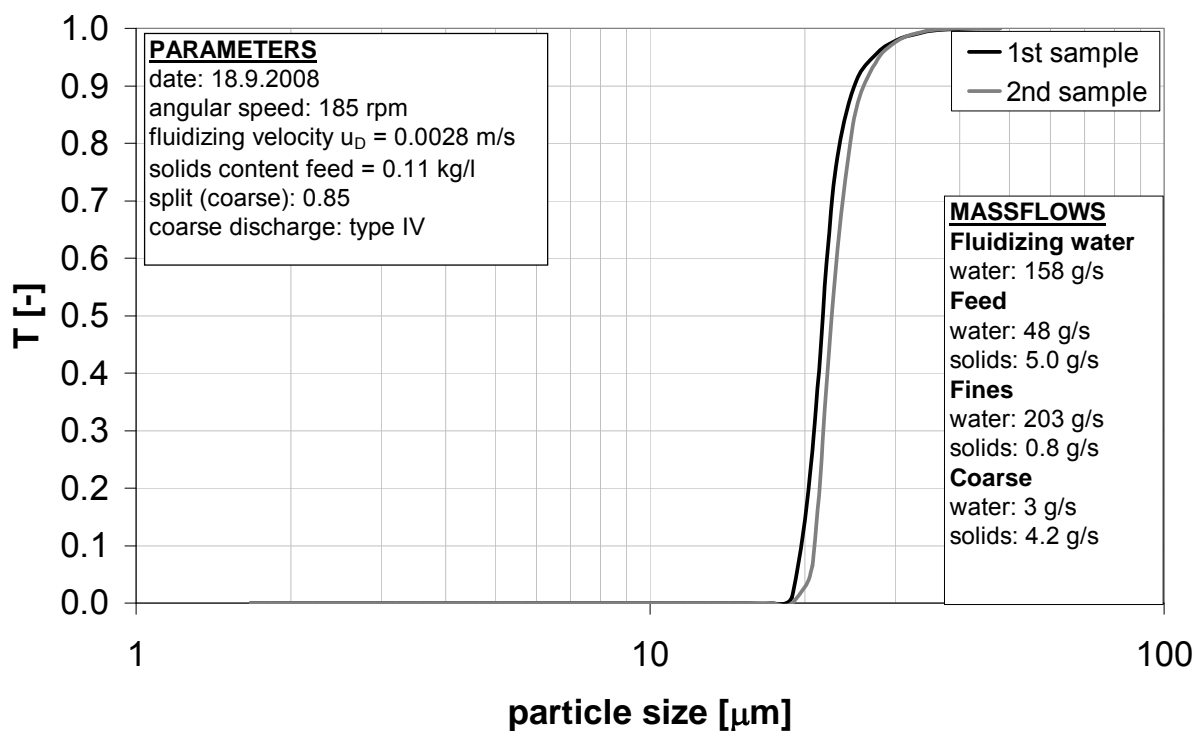


**Figure 6.49:** Separation efficiency curve of glass beads classification at a constant bed height of 1.90 cm (18.9.2008)

### 6.10 Practical example of the control strategies for quartz powder classification

In the previous chapters the classification process of the present classifier was discussed in detail and the results of the investigations were presented. Finally the findings will now be used to design a classification process with the classifier of the present work.

For the given material, which is to be classified with the certain cut size  $d_C$ , a rotational speed and the bed height in the classifier are chosen. The necessary fluidizing velocity and the permissible feed mass flow are calculated. An estimation of the minimum fluidizing velocity  $u_{mf}$  will prove the feasibility of the given classification task, i.e. when  $u > 1.5 \times u_{mf}$ .

As an example the quartz powder with the properties presented in chapter 5.1 was selected as the material to be classified. A cut size with a diameter of  $d_C = 7 \mu\text{m}$  was chosen. Under the assumption of an ideal classification, the fines fraction  $f$ , the coarse fraction  $c$  and their cumulative mass distributions  $Q_{3,F}(d_p)$ ,  $Q_{3,C}(d_p)$  are given due to the cut size  $d_C$  and the feed mass distribution  $Q_{3,S}(d_p)$  by:

$$f = Q_{3,S}(d_C) \quad (6.5)$$

$$c = 1 - f \quad (6.6)$$

$$Q_{3,F}(d_p) = Q_{3,S}(d_p)/f; \quad \text{for } d_p < d_C \quad (6.7)$$

$$Q_{3,C}(d_p) = [Q_{3,S}(d_p) - Q_{3,S}(d_C)]/c; \quad \text{for } d_p > d_C \quad (6.8)$$

For the present case  $f = 0.4$  and  $c = 0.6$  are obtained, the cumulative mass distributions of the feed, fines and coarse fraction are shown in figure 6.50. Under the assumption that the coarse mass distribution equals the one of the fluidized bed, a median diameter of  $d_{p,50} = 16 \mu\text{m}$  and a Sauter diameter of  $d_{32} = 15 \mu\text{m}$  for the fluidized bed are obtained.

For classifications with cut sizes below 10  $\mu\text{m}$  rotational velocities larger than 400 rpm are recommendable. For the present case 500 rpm were chosen to be suitable. A higher rotational speed would result in an unnecessarily high throughput of fluidizing water. For bed heights of 3.0 cm and above, sharp classifications were obtained (cf. experiments 28.4.2008 and 8.5.2008, figures 6.40 and 6.45), so that a target bed height of 3.5 cm was selected, i.e. the surface of the fluidized bed is  $R_B = 0.41$  m. From figure 5.8 the terminal velocity of the fluidized bed can now be taken with  $u_t = 0.020$  m/s.

Applying equations (5.58), (5.57) and (5.39) gives the fluidizing velocity  $u$ , the bed porosity  $\varepsilon$  and the mass of solids  $m_S$  in the fluidized bed:

fluidizing velocity:  $u = 0.0042$  m/s

bed porosity:  $\varepsilon = 0.71$

solids mass in the bed:  $m_S = 1.58$  kg

For the given solids mass  $m_S$ , the theoretical fixed bed height  $H_{FB} = 2.1$  cm or the radius of the fixed bed surface  $R_{FB} = 0.424$  m are calculated by equation (5.36) under the assumption of a fixed bed porosity of 0.5 (cf. figure 6.19).

The equations (5.37) and (5.45) allow the estimation of the pressure drop profile, which is pictured in figure 6.51. A minimum fluidizing velocity of  $u_{mf} = 0.0007$  m/s is obtained. The ratio  $u/u_{mf}$  is then

$$\frac{u}{u_{mf}} = \frac{0.0042 \text{ m/s}}{0.0007 \text{ m/s}} = 6 \quad \rightarrow \quad u_{mf} > 1.5$$

This means that the feasibility of the classification process is proven.

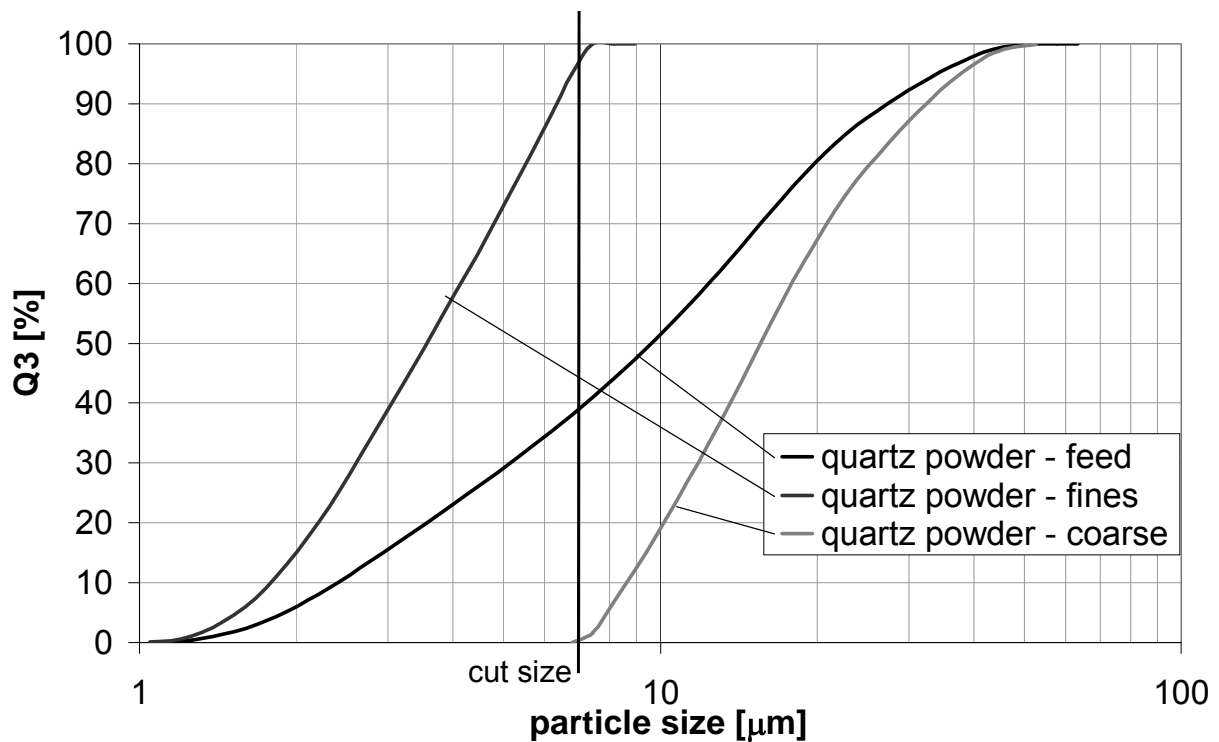


**Figure 6.50:** Cumulative mass distributions of the feed, the coarse and the fines fraction for an ideal quartz powder classification with the cut size  $d_C = 7 \mu\text{m}$

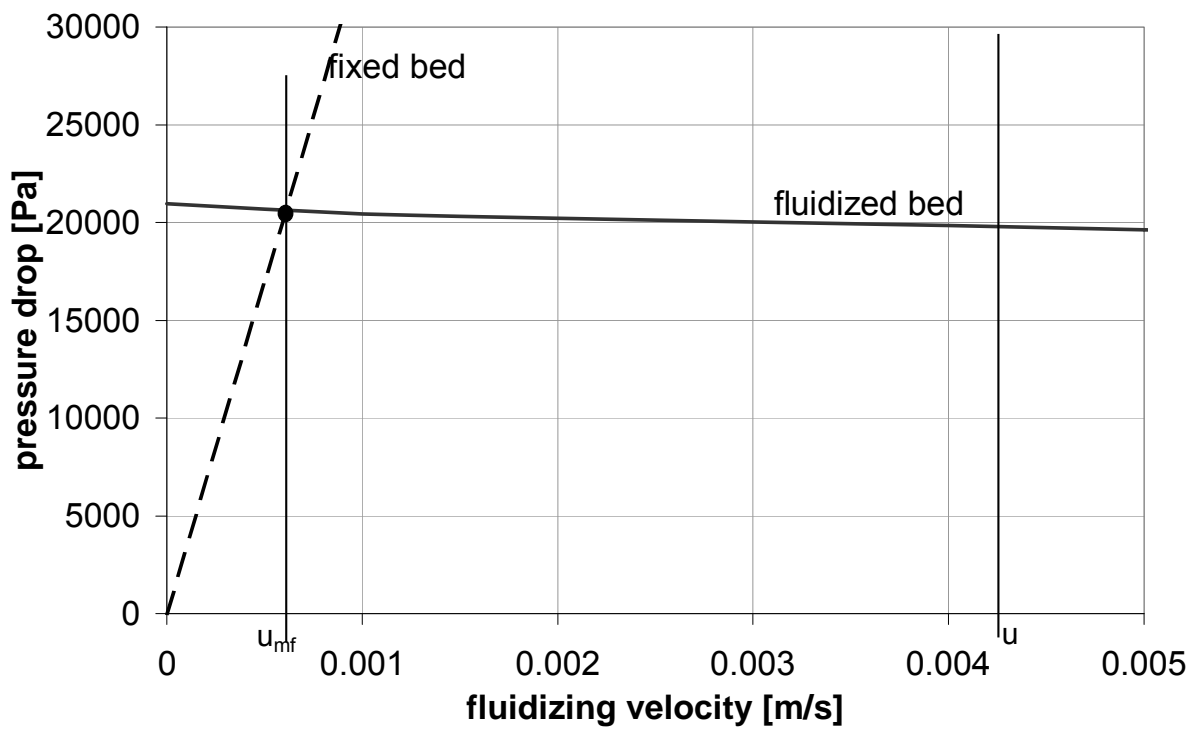


**Figure 6.51:** Calculated pressure drop profile for the example of quartz classification at 500 rpm with a cut size  $d_C = 7 \mu\text{m}$  and a fluidizing velocity  $u_D = 0.0042 \text{ m/s}$

With the discharge nozzle (IV) with an orifice diameter of  $d_N = 1$  mm, equations (5.55) and (5.56) give the coarse discharge suspension and solids mass flow:

$$\dot{M}_{\text{sus,c}} = 9.1 \text{ g/s}$$

$$\dot{M}_c = 4.5 \text{ g/s}$$

The required solids feed mass flow is then given by

$$\dot{M}_s = \frac{\dot{M}_c}{c} = 7.5 \text{ g/s} \quad (6.9)$$

It should be noted that the target bed height is in fact controlled via the feed mass flow. For the given case a tolerance interval of  $\pm 0.5$  cm from the target bed height is acceptable. The radius of the fluidized bed surface is correlated via equation (5.38) with the bed pressure drop, whereby the radius  $R_B$  of the bed can be calculated even when the bed height cannot be determined optically due to turbidity. In figure 6.52 the bed pressure drop is plotted versus the bed height for the present case. The ideal operation point and the acceptable tolerance interval are provided to ensure a high sharpness and a constant cut size. Via figure 6.52 the operator is provided with the valuable information about the operating status of his classification process. The easiest way to keep the pressure drop and thus the bed height at the desired level is to adjust the feed mass flow accordingly.

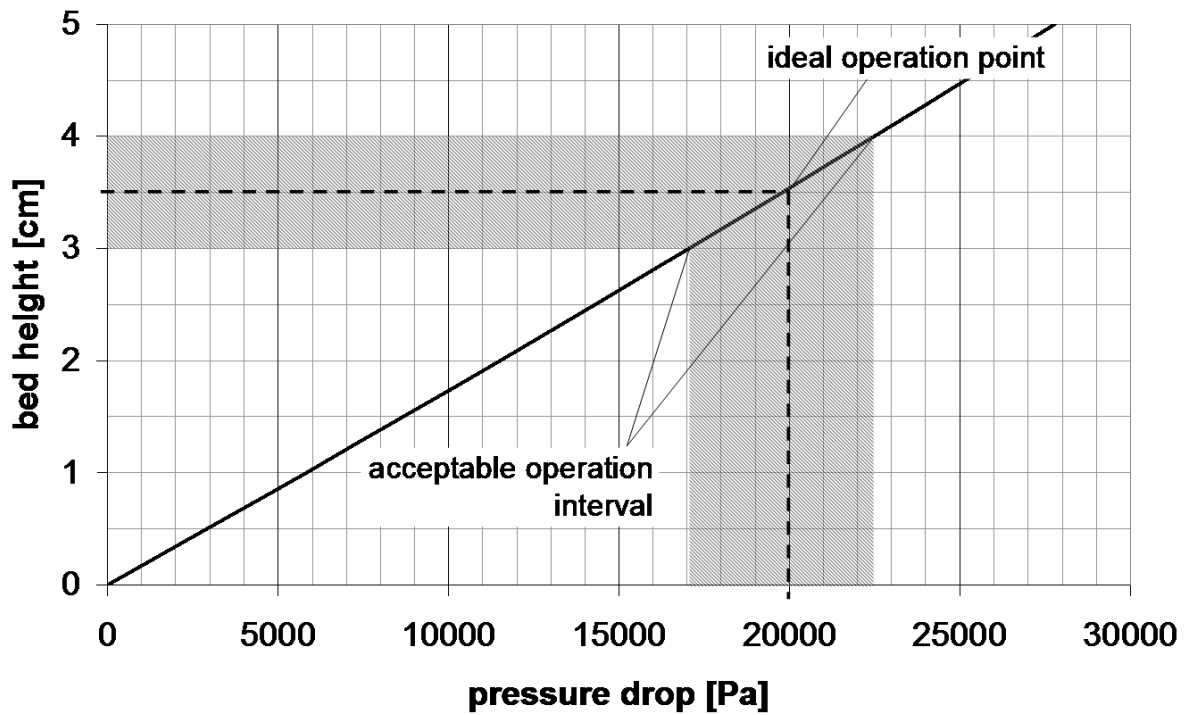


**Figure 6.52:** Bed height versus pressure drop diagram for the example of quartz classification at 500 rpm with a cut size  $d_p = 7 \mu\text{m}$  and a fluidizing velocity  $u_D = 0.0042 \text{ m/s}$



## 7 Summary and Conclusions

A centrifugal counter current classifier was investigated and optimized. The classifier can be operated continuously and is designed for wet classification in the micron range. The principle of the classifier is based on gravity elutriation but is transferred to the centrifugal field. The fluid mechanics were analyzed experimentally and with CFD simulations.

First tests in the solids-free chamber revealed an intense tangential flow in the direction of rotation, which is caused by the Coriolis force, resulting from the radial flow of the liquid. Also air shows a high tangential velocity under similar conditions but with lower tangential velocities due to a higher effect of the wall friction.

Numerical simulations of the liquid flow field are confirmed by measurements in a pilot-scale apparatus. The tangential velocity is significantly higher than the radial fluid velocity. When the chamber is filled with particles a liquid fluidized bed is set up. In its freeboard the intense tangential flow is detected again. The fluidized bed itself is also moving in the tangential direction, however, with a much lower velocity than the freeboard. But even in the fluidized bed, the tangential velocities relative to the rotating apparatus are significantly higher than the radial ones. The bed expansion of the fluidized bed can be described by a Richardson-Zaki type power law. The Richardson-Zaki exponents have values  $n$  of 4.9 (glass beads), 4.5 (quartz) and 5.9 (limestone) for the presently investigated particles with mean particle sizes around 30  $\mu\text{m}$ . The findings are useful for designing a new coarse discharge mechanism.

As the tangential bed movement is still significant it can be concluded that a single coarse discharge is sufficient. Thus the previously installed four needle valves were replaced by a single coarse discharge nozzle. A constant bed height could now be

achieved with an equilibrium of bed height and coarse outlet flow. For reaching this equilibrium the orifice diameter of the discharge nozzle has to be adapted to the desired coarse discharge flow or vice versa.

Pressure drop measurements were carried out to determine the onset of fluidization and the minimum fluidizing velocity. A stable fluidization, which is achieved at fluidizing velocities above  $1.5 \times u_{mf}$ , and a fully submerged coarse discharge were found to be essential for a sharp classification. Classification experiments were performed with glass beads, quartz and limestone and very sharp separations were achieved with cut sizes down to 5 microns.

The investigation of the influence of the bed height revealed that with increasing bed height an enhancement of the sharpness with a slight increase of the cut size occurs. Increasing the bed height to the radius of the feed port the solid particles are directly injected to the bed. As the classification is still sharp it can be concluded that the bed has to be strongly segregated.

The results showed that this classifier is very capable for separation tasks in the micron range. The fishhook effect can be almost completely eliminated, when the classifier is operated correctly.

Comparing the rotating fluidized bed classifier with other devices it can be concluded that the sharp separation efficiency of gravity elutriators is achieved at cut sizes in the micron range. The fishhook effect, which is a problem with hydrocyclones, was eliminated and misclassifications were strongly reduced compared to the previous configuration.

## Nomenclature

$\bar{a}_c$	Coriolis acceleration
$A_C, A_D$	cross sectional area, cross sectional area of the distributor [ $m^2$ ]
$B$	width of the chamber [m]
$c_D$	drag coefficient [-]
$c$	coarse fraction [-]
$C$	water mass flow of the coarse suspension [kg/s]
$C_K$	Kozeny constant [ $C_K = 4$ ]
$d_C$	cut size [m]
$d_h$	hydraulic diameter [m]
$d_N$	inner diameter of coarse discharge nozzle [m]
$d_p$	particle diameter [m]
$d_{ps}$	Sauter diameter [m]
$d_{ts1}, d_{ts2}, d_{ts3}$	diameters of the tracer spheres [m]
$E(d_p)$	error function [mg/s]
$f$	finer fraction [-]
$F$	water mass flow of the fines suspension [kg/s]
$F_B, F_C, F_D, F_W$	buoyancy, centrifugal, drag and wall friction force [N]
$F_{DR}, F_{DT}, F_S$	drag forces in radial and tangential direction, force on chord [N]
$g$	gravity acceleration [ $g = 9.81 \text{ m/s}^2$ ]
$K$	chamber profile constant [ $K = 0.00396 \text{ m}^3$ ]
$K_D$	distributor pressure drop coefficient [ $\text{Pa}\cdot\text{s/m}$ ]
$H_B$	fluidized bed height [m]
$H_{FB}$	height of the fixed bed [m]
$L$	circumference [m]
$L_C$	length of the thread (tracer sphere) [m]
$\dot{m}$	mass flow [kg/s]
$m_S$	mass of the solids in the fluidized bed [kg]

$m_L$	mass of water in the classification chamber
$m_{ts}$	mass of the tracer sphere [kg]
$n$	Richardson - Zaki exponent [-]
$M_F, M_O, M_W$	angular momentums (incoming flow, outgoing flow, torque) [N·m]
$\dot{M}_F, \dot{M}_S, \dot{M}_C$	solids mass flows of fines, feed and coarse discharge [g/s]
$\dot{M}_{SUS,S}, \dot{M}_{SUS,C}$	mass flows of the feed and coarse suspension [g/s]
$p$	pressure [Pa]
$Q_{3,S}(d_p), Q_{3,C}(d_p),$ $Q_{3,F}(d_p)$	cumulative mass distributions of the feed, coarse and fines particles [%]
$q_{3,S}(d_p), q_{3,C}(d_p),$ $q_{3,F}(d_p)$	mass density distributions of the feed, coarse and fines particles [%/m]
$r$	radius [m]
$r_{ts}, r_F$	radial position of the tracer sphere and the chord fixing [m]
$R_D, R_W, R_B, R_N$	radii of the distributor, the overflow weir, the bed surface and the coarse discharge nozzle [m]
$Re_{ts}, Re_p$	Reynolds numbers (tracer sphere, particles)
$S$	water mass flow of the suspension [kg/s]
$S_V$	specific surface of a particle collective [1/m]
$T(d_p)$	separation efficiency curve [-]
$u, u_t$	fluidizing velocity, terminal velocity [m/s]
$u_d$	fluidizing velocity at the distributor [m/s]
$\dot{V}$	water volume flow [m <sup>3</sup> /s]
$V_B$	bed volume [m <sup>3</sup> ]
$W$	fluidizing water mass flow [kg/s]
$v_N$	fluid velocity through the discharge nozzle [m/s]
$v_R$	radial fluid velocity [m/s]
$v_T$	tangential velocity (relative to the rotor) [m/s]
$V_{ts1}, V_{ts2}$	Volumes of the tracer spheres [m <sup>3</sup> ]
$w$	absolute tangential velocity (observer located outside) [m/s]

---

$x_S, x_F, x_C$	solids loadings of the feed, the fines and the coarse suspension
$\alpha, \delta, \gamma$	angles for evaluation of the force balances on the tracer spheres
$\varepsilon$	porosity of the fluidized bed [-]
$\varepsilon_{FB}$	fixed bed porosity [-]
$\kappa$	classification sharpness
$\eta$	fluid viscosity [Pa·s]
$\lambda$	wall friction coefficient [-]
$\rho_S, \rho_L$	densities of solids and liquid [kg/m <sup>3</sup> ]
$\rho_m$	mean fluidized bed density [kg/m <sup>3</sup> ]
$\xi$	nozzle pressure drop coefficient
$\omega$	angular velocity [1/s]

## References

- Bickert, G., "Sedimentation feinsten suspendierter Partikel im Zentrifugalfeld", Dissertation, Universität Karlsruhe (1997).
- Bohl, W., „Technische Strömungslehre“, Vogel Buchverlag (1991)
- CFX, „CFX Version 5.7, Reference Manual“, ANSYS Germany GmbH, Otterfing, Germany (2004).
- Colon, F., van Heuven, J., van der Laan, H., „Centrifugal Elutriation of Particles in Liquid Suspension.“, Groves and Wyatt-Sargent(Editors): Particle Size Analysis, pp.42-52, Bradford 9.-11.9.1970, The Society of analytical chemistry.
- De Wilde, J., de Broqueville, A., "Rotating fluidized beds in a static geometry: experimental proof of concept", AIChE Journal, Vol.53, No.4, pp.793-810 (2007)
- Dixon, "Fluid Mechanics, Thermodynamics of Turbomachinery," 5<sup>th</sup> edition, Elsevier Butterworth-Heinemann, Oxford, UK (1998)
- Gerhart,C., "Untersuchungen zum Trennverhalten von Hydrozyklonen niedriger Trennkorngrößen, Dissertation, Universität Erlangen (2001)
- Heiskanen, K., „Particle Classification“, Chapman & Hall, London (1993)
- Hidaka, N., „Correlation of solid holdup in liquid-solid fluidized bed“, Journal of Chemical Engineering of Japan“, Vol. 27, No.5, pp. 563-570, (1994)

Kalck, U., Werther, J. „Zum Einsatz von Aufstromklassierern für die Aufbereitung kontaminierter Baggerschlämme“, Aufbereitungstechnik, 31(11), pp. 593-601, (1990)

Kellerwessel, H., Zahr, P., “Nassklassierung von Erz- und Mineralsuspensionen unterhalb 10 mm mittels Vollmantel-Zentrifugen“, Erzmetall, 32(5), pp. 227-231, (1979)

Kerkhoff, T. „Feinkornklassierung in einem luftkernlosen Hydrozyklon“, Dissertation, Universität Erlangen (1996)

Kunii, D., Levenspiel, O., „Fluidization Engineering“, Butterworth-Heinemann (1991)

Mahabadi, H., Stocum, A., "Xerox's Emulsion Aggregation Toner – An Environmentally Friendly Technology", Xerox Corporation, (2006)

Majumder A.K., “The fish-hook phenomenon in the centrifugal separation of fine particles”, Minerals Engineering 16 (2003); pp. 1005–1007

Malvern Instruments Ltd., “Laser diffraction for particle analysis – why use Mie theory?”, LabPlus international, p.28, (November 2000)

Margraf, J., Werther, J., “Fluid mechanics of liquid-solid fluidization in the centrifugal field“, The Canadian Journal of Chemical Engineering, Vol. 86, pp. 276-287, (2008)

Nakamura, H., Iwasaki, T., Watano, S., “Modeling and measurement of bubble size in a rotating fluidized bed”, AIChE Journal, Vol. 53, No. 11, pp. 2795-2802, (2007)

Nakamura, Y., Kutsuwada, N., „Direct measurement of toner particle size“, Applications Society Annual Meeting, Conference Record of the 1989 IEEE, Volume, Issue, 1-5, pp:2239 – 2242, (1989)

Priesemann C., "Naßklassierung in einer Aufstromzentrifuge", Dissertation, University of Clausthal, (1994)

Qian, G-H., Burdick, I.W., Pfeffer, R., Shaw, H., Stevens, J.G., "Soot removal from diesel engine exhaust using a rotating fluidized bed filter", *Advances in Environmental Research*, Vol. 8, Iss. 3-4, pp. 387-395 (2004)

Richardson J.F. and Zaki W.N., "Sedimentation and Fluidization I", *Trans. Inst. Chem. Eng.*, pp.35-52, (1954)

Schmidt, J., "Wirbelschichtklassierung von Feinstkornsuspensionen im Zentrifugalfeld", Dissertation, Technische Universität Hamburg-Harburg (2004)

Schmidt J. and Werther J., "Separation Efficiency of a Centrifugal Fluidized Bed Classifier in the Micron Range", *J. Chinese Inst. of Chem. Eng.*, 36, pp. 49-60 (2005)

Schröder R., "Technische Hydraulik – Kompendium für den Wasserbau", Springer Verlag, (2004)

Stieß M., "Mechanische Verfahrenstechnik 1", Springer Verlag, (1993)

Timmermann D., "Kontinuierliche Naßklassierung in einer Aufstromzentrifuge im Feinstkornbereich", Dissertation, University of Clausthal, (1998)

Tsuchiya K., Furumoto A., Fan L.S, Zhang, J., "Suspension viscosity and bubble rise velocity in liquid-solid fluidized beds", *Chem. Eng. Sci.* 52, 18, pp. 3053-3066, (1997)

Wang, Y., Forssberg, E., Axelsson, H., Hoel, F., Brehmer, P., „Wet classification of industrial mineral fines using a disc-stack nozzle centrifuge“, *Proceedings of the XX IMPC-Aachen*, pp. 475-487, 21-26 September 1997



Watano S., Imada Y., "Microgranulation of fine powders by a novel rotating fluidized bed granulator", Powder Technology 131, pp. 250-255 (2003);

Watano S., Nakamura H., "Fine particle coating by a novel rotating fluidized bed coater", Powder Technology 141, pp. 172-176, (2004)

Webster, J. G., "The measurement, instrumentation and sensors handbook", (1999)

## Curriculum vitae

### Jan Margraf

---

22/04/1976                      born in Hamburg, Germany

### Education

---

08/1982 – 07/1986              Elementary School in Stade, Germany

08/1986 – 07/1988              Orientierungsstufe in Stade, Germany

08/1988 – 06/1996              Gymnasium Stade

06/1996                          Abitur

### Military Service

---

07/1996 – 08/1996              Basic Training in Goslar, Germany

09/1996 – 04/1997              Service in a supply unit in Visselhövede, Germany

### Internships

---

05/1997 – 08/1997              Technical internship with Synthopol Chemie in Buxtehude, Germany

10/2003 – 01/2004              Internship in the R&D department of Robert Bosch GmbH, Gerlingen, Germany

### Academic History

---

11/1997 – 09/2004              Studies in Process Engineering at Hamburg University of Technology

09/2004                          Graduation: Diplom Ingenieur

11/2004 – 11/2008              Doctoral candidate in the Institute of Solids Process Engineering and Particle Technology of the Hamburg University of Technology

### Experience

---

Since 01/2009                      Development Engineer at HJS GmbH in Menden, Germany